# Impulsive signals search with the gravitational wave detector Virgo

André-Claude Clapson

▶ **To cite this version:**

André-Claude Clapson. Impulsive signals search with the gravitational wave detector Virgo. Cosmology and Extra-Galactic Astrophysics [astro-ph.CO]. Université Paris Sud - Paris XI, 2006. English. NNT : . tel-00085885

**HAL Id: tel-00085885**
**https://theses.hal.science/tel-00085885**

Submitted on 17 Jul 2006

**HAL** is a multi-disciplinary open access archive for the deposit and dissemination of scientific research documents, whether they are published or not. The documents may come from teaching and research institutions in France or abroad, or from public or private research centers.

L'archive ouverte pluridisciplinaire **HAL**, est destinée au dépôt et à la diffusion de documents scientifiques de niveau recherche, publiés ou non, émanant des établissements d'enseignement et de recherche français ou étrangers, des laboratoires publics ou privés.

ORSAY
n° d'ordre :

**LAL 06-45**
Avril 2006

UNIVERSITÉ DE PARIS SUD
CENTRE D'ORSAY

THÈSE *présentée*

*pour obtenir*

Le GRADE de DOCTEUR EN SCIENCES
DE L'UNIVERSITÉ PARIS XI ORSAY

Spécialitée : Astrophysique

*par*

**André-Claude CLAPSON**

# *Recherche de signaux impulsionnels sur le détecteur d'ondes gravitationnelles Virgo*

~

## *Analyse temps-fréquence*

## *Suppression de lignes spectrales*

Commission d'examen

| | | | |
|---|---|---|---|
| MM. | Eric | AUBOURG | Examinateur |
| | Eric | GOURGOULHON | Examinateur |
| | Patrice | HELLO | Directeur de Thèse |
| | Erik | KATSAVOUNIDIS | Rapporteur |
| | Fulvio | RICCI | Rapporteur |
| | Guy | WORMSER | Examinateur |

*Geometrica demonstramus quia facimus ;*
*si physica demonstrare possemus, faceremus.*

Les choses mathématiques nous pouvons les démontrer
parce que nous les faisons nous-mêmes ;
pour démontrer les choses physiques,
il nous faudrait les faire.

Giambattista Vico
**De Nostri Temporis Studiorum Ratione** (1708)

# Introduction

Virgo is a ground observatory, built in Italy near Pisa. It is dedicated to the detection of gravitational waves. The instrument is a Michelson interferometer modified by the addition of Fabry-Perot cavities in the (3 km long) arms and recycling of light power. All the mirrors are suspended, to approach free fall conditions and suppress seismic noise. Several instruments of similar principle are in activity in the collaborations GEO, LIGO and TAMA.
The expected sources are relativistic astrophysical systems, compact and massive objects in excited states. The most studied, though not observed yet, are neutron stars and black holes, notably at the formation stage. Such would be a type II supernova or the inspiral of a binary system of compact objects. Even at the target sensitivity, the estimates in observation occurrence rates and amplitudes remain low : a few events per century for supernovae and a signal to noise ratio below 10. These circumstances justify the importance of the reduction of instrumental noise and the development of efficient methods for the recovery of low energy signals in noisy data.
An introduction on the theoretical framework of General Relativity, instrument principles and a short review of expected astrophysical sources are provided in Chapter 1.

This work took place within the Virgo group from the Laboratoire de l'Accélérateur Linéaire while the final steps toward the control of the instrument were taken. The conclusion of this phase was delayed by several months, due to hardware modifications carried out in summer 2005. Before this interruption, there were several data-taking runs, with a progressively improved sensitivity.
The activities of the LAL Virgo group cover data analysis, in particular the search for impulsive signals (typically shorter than 100 ms) and network analysis, the control of the instrument and research and development for the next generation of instruments (notably the signal recycling technique).

## Time-frequency analysis methods

The short signal detection problem, namely the low energy and variety of the waveforms, has prompted many analysis approaches. An additional difficulty comes from the power spectral density of noise in instruments like Virgo, very unevenly distributed among the frequency bands, and observed to vary with time.
To add to the range of methods already developed, notably in the LAL group, time-frequency transforms, explored as well within the LIGO collaboration, are considered in Chapter 2.
Three methods with *a priori* complementary properties were selected. Firstly an implementation of the wavelet transform, where data is reversibly decomposed on a simple waveform repeatedly dilated in time, the 'à trous' algorithm. Secondly the S Transform, a modified Gabor transform where the time resolution Gaussian kernel is adjusted in duration according to the selected frequency. Lastly a time-frequency derivation of the match filtering technique, using as templates complex exponentials with a Gaussian envelop.
These transforms produce time-frequency 'maps', from which the relevant events are to be extracted, ideally without loss of energy nor mix between signal and noise. To this end, in addition to the transforms themselves, a time-frequency analysis chain was developed. It allows the normalization of the maps, noise rejection and clusterization of selected elements into time-frequency events.
The performance characterization of these algorithms is based on the selection of the parameters (frequency band, data-segment duration, event-defining thresholds) providing in (Monte Carlo) simulation the best visibility for test waveforms.
Besides, these methods were taken in consideration by the joint working group set up in 2004 between the LIGO and Virgo collaborations to pave the way for a future network analysis. The first

goal of this joint group has been to compare the available detection methods. This opportunity permitted to establish the interest of the original and promising algorithm described here.

## Mechanical-resonances suppression in Virgo data

Suspended mirrors introduce noise, in particular through the thermally excited mechanical resonances of the suspension wires and mirrors. Thanks to the choice of materials for Virgo, those resonances have large quality factors, thus reducing the affected frequency bands. The resulting structures may affect the performances of signal detection algorithms that prefer stable and smooth Gaussian noise backgrounds. Detection methods in the time domain and some time-frequency decompositions would benefit from the removal of these structures.
Fortunately this noise is sufficiently coherent to be described with a simple model. The possibility of removing resonances in the data had been tested in the LIGO collaboration. Their preliminary results were positive, which called for an equivalent algorithm, based on Kalman filtering, to be tested for Virgo.
Chapter 3 presents the activity on this topic. Other pre-processing methods exist for the same end, but are not explored here.
The bulk of the work concerned the systematic quantification of the filter quality, then the issue of the estimation of model parameters (essentially resonance frequency, equivalent mass and quality factor), in view of its application to Virgo. Indeed, it was shown that an error of a few percents on a parameter can considerably reduce the performances of the filter, possibly affecting a broad range of frequencies.
Generic modifications of the Kalman filtering technique did not give satisfying results in this particular case. A robust approach was designed, with the goal of estimating parameters with enough accuracy for an efficient filtering, from data durations as small as possible. This constraint comes from the observed parameter variability, due for instance to temperature fluctuations, that may imply frequent parameter updates.

## Analysis of instrumental data

The actual behaviour of an instrument always differs from models, especially simple ones. Simulated data as used in the Virgo collaboration have a static Gaussian distribution, far from the available measurements. Therefore it is mandatory to characterize anew the analysis methods and possibly to modify them.
This work can also contribute to improve the understanding of the instrument. The necessary reduction of the false alarm rate relies strongly, especially for impulsive signals, on the identification of instrumental or environmental origins.
Joining this effort, the tools introduced for both noise pre-processing and time-frequency analysis were put to use. Information on instrumental noise were extracted for the latest Commissioning Run, as detailed in Chapter 4. It was possible to isolate three populations of noise events with similar characteristics. Coincidence with auxiliary data permitted to identify the origin of these events, and thus to suppress them confidently.

# Contents

# List of Figures

# List of Tables

# Chapter 1

# Gravitational waves and related astrophysics

## Contents



## 1.1 Introduction to gravitational waves

A physical description of the world relies on, at least, four extensive dimensions. Space, the three coordinates required to position an object, or estimate its volume, and time, the parameter of motion and change. Without questioning the definition of time (see [1] for such a discussion), or the possible intervention of extra physical dimensions, as proposed by string theory ([2] offers an introduction to the topic), these four dimensions have allowed the construction of classical physics including gravitation, with the major contributions of Newton and Einstein. General Relativity, presented in 1915 by the latter, is currently the leading model for gravitation-related phenomena. Among other observable effects, it predicts the existence and behaviour of gravitational waves, for which an experimental detection has yet to be made. Note that these are classical theories and

waves, independent from quantum mechanics.
Before developing instrumental and astrophysical considerations, a brief layout of the theoretical framework is in order. Though not always mentioned in the text, all the material comes from references [3] to [11].

### 1.1.1 Newtonian gravitation

Newton's theory of gravitation is a very successful description of the world around us. It took observations of celestial bodies, namely the perihelion advance of Mercury, discovered by Leverrier in 1845, to question its universality, and some more time to find a replacement with General Relativity.
The laws of Newtonian physics that concern gravitation are :

$$\vec{F} = m_i\vec{a} \quad \text{second law of dynamics} \tag{1.1}$$
$$\vec{F} = m_{pg}\vec{g} \quad \text{law of gravitation} \tag{1.2}$$

The first one relates any applied force $\vec{F}$ to the acceleration $\vec{a}$, while the second derives the gravitational pull from a universal acceleration. In this framework, forces propagate instantaneously.
The Principle of Equivalence initially concerned the relation between the different masses, 'inertial' mass $m_i$ and 'passive gravitational' mass $m_{pg}$, presented by the same object. The Principle of Equivalence states that $m_i = m_{pg}$ for any body. A more general formulation of Newtonian gravitation introduces the universal constant $G$ :

$$\Delta\phi(\mathbf{x}) = 4\pi G\rho(\mathbf{x}) \quad \text{Poisson equation for the gravitational potential } \phi \tag{1.3}$$
$$\ddot{x_i} = -\frac{\partial\phi}{\partial x_i} \quad \text{for the gravitational acceleration} \tag{1.4}$$

for $\rho$ the mass density of matter and $\Delta$ the Laplacian operator: $\Delta = \nabla^2 = \partial_i\partial^i x = \sum \frac{\partial^2}{\partial {x_i}^2}$.
Put differently, all bodies affected by the same gravitational field fall with the same acceleration, regardless of their internal properties, mass included.
Consider bodies free-falling in the same gravitational field, that is to say affected by no external force except gravity. The mechanical relation of equation 1.1 indicates that those bodies will behave with respect to each other as if there were no gravitational pull at all. In a local reference frame, accelerated with respect to an external observer non affected by gravity, the influence of gravity cannot be identified.

#### Classical definition of space-time

In an Euclidean coordinate system with its three space dimensions (x,y,z), plus time (t), an event M is defined as $M(t,x,y,z)$. Compact notation gives $M(X_\alpha)$ with $\alpha \in [0,3]$ such as $X_0 = t$ *etc.* Note that since the time coordinate plays a specific role compared to the spatial ones, two types of manipulation are to be distinguished concerning either any of four coordinates, indicated by a Greek letter, for instance the above $\alpha$, or any of the spatial coordinate, with a Latin letter, *e.g.* $i \in [1,3]$.

Given two events M and M' and Cartesian coordinates [1] the distance $L$ between them is :

$$L_{MM'} = \sqrt{\sum_i (x^i_{M'} - x^i_M)^2} \tag{1.5}$$

or for objects infinitely close, $dl^2 = dx^2 + dy^2 + dz^2$. Using a repeated summation convention, this expression becomes $dl^2 = \Sigma\delta_{ij}dx_i dx_j = \delta_{ij}dx^i dx^j$ where $\delta_{ij} = 1$ if $i = j$, 0 otherwise. The coefficients $\delta_{ij}$ can be conveniently grouped in a matrix :

$$\delta = \begin{pmatrix} 1 & 0 & 0 \\ 0 & 1 & 0 \\ 0 & 0 & 1 \end{pmatrix} \tag{1.6}$$

[1] defined with an orthogonal base of directions.

By replacing $\delta$ with a generic matrix $g$, this formula allows more general combinations of coordinates, and definitions of distances [2]. As such, $g$ is called a metric, with in the Euclidean case $g = \delta$.
Time does not appear in the Euclidean distance. In classical physics, forces apply immediately, so the propagation delay is null. For a finite velocity motion between M and M', in straight line with speed $v$, the time separation is simply $T_{MM'} = L/v$.

The same events can be described in different coordinate systems. With time considered to be universal, the spatial referential system can be changed, from $M(t, x_i)$ to $M(t, x'_i)$. Obviously, a relation exists between the two coordinates, with $x'(x)$ giving the value of $x'$ for any $x$. It can be shown that the distance formula also changes, with $dl^2 = (\delta_{ij} \frac{\partial x^i}{\partial x'^k} \frac{\partial x^j}{\partial x'^l}) dx'^k dx'^l$ and

$$g_{kl}(x') = \frac{\partial x^i}{\partial x'^k} \frac{\partial x^j}{\partial x'^l} g_{ij}(x) \tag{1.7}$$

in the generic case. This is the Galilean coordinate transform.

### Relativity Principle

From empirical observation, it seemed necessary that reference systems even in relative motion could host the same physical phenomena. Newton introduced the notion of inertial systems, favored reference systems submitted to no acceleration. All these systems would be equivalent with respect to physical laws.
A world-line describes the space-time trajectory of such a reference system. These are straight lines in Newtonian gravitation.
The Relativity Principle notably holds for the electromagnetic fields $E$ and $B$, whose laws are :

$$\Delta E(or B) - \frac{1}{c^2} \frac{\partial^2 E(or B)}{\partial t^2} = \Box E(or B) = 0 \tag{1.8}$$

$\Box$. is called the d'Alembertian operator.

### Special relativity framework

The classical space-time model does not function well once introduced electromagnetism and its fixed vacuum velocity for light ($c$). To synchronize clocks, the best allowed scheme is to consider the propagation time of a light beam between them. When the clocks belong to distinct inertial referentials in relative motion, the velocity term introduced in the synchronization equation does not satisfy anymore the absolute time rule. This is an indication of the inadequacy of the Galilean coordinate transform.

For non-gravitational physics, the resolution of the problems met by the classical model of space-time was provided by Special Relativity.

**Minkovski space-time** The synchronization conundrum could only be solved by foregoing either the fixed value of $c$ or the existence of an absolute time, that would be shared by all inertial systems.

If local times are allowed, the definition of distance and the rule for a coordinate system change can be modified to permit clock synchronization. The mathematically most simple formulation is for distance : $ds^2 = -c^2 dt^2 + dx_i dx^i$ for an inertial referential in Cartesian coordinates. Considering the four-coordinates $x^\mu = (ct, x_i)$, the metric is now :

$$g_{\mu\nu} = \begin{pmatrix} -1 & 0 & 0 & 0 \\ 0 & 1 & 0 & 0 \\ 0 & 0 & 1 & 0 \\ 0 & 0 & 0 & 1 \end{pmatrix} \tag{1.9}$$

This specific form will be noted $\eta_{\mu\nu}$ hereafter, as a reference case. As time and metric are now linked, it is possible for a clock at rest in an inertial referential to define a proper time $\tau$ such as $ds^2 = -c^2 d\tau^2$.

[2] To respect the properties of a distance, $g$ must be symmetric and define a quadratic form.

Coordinate changes are modified accordingly, from the Galilean transform to the Lorentz transform. In the 'Standard Configuration', where both start and end coordinate systems are Cartesian, with identical time origin, parallel axes and a relative velocity $v$ along $x\vec{x}'$, the formulation simplifies into the special Lorentz transform :

$$\begin{cases} ct' = \dfrac{ct - \frac{v}{c}x}{\sqrt{1-\frac{v^2}{c^2}}} \\ x' = \dfrac{x - vt}{\sqrt{1-\frac{v^2}{c^2}}} \\ y' = y \\ z' = z \end{cases} \tag{1.10}$$

This new space-time, where time and spatial dimensions are not independent anymore is called the Minkovski space-time. The limit of vanishingly small translation velocity is the classical space-time, with independent time and space, fortunately.
When velocities become commensurate with c, the properties of this space-time are not supported by intuition. Take for instance a merry-go-round that spins extremely fast. Someone standing next to it could measure its radius and circumference, and recover $\pi$ from the ratio of the two. But a person on the merry-go-round performing the same measurements would obtain, instead of $\pi$, the value $\frac{\pi}{\sqrt{1-(\frac{r\omega}{c})^2}}$. This the relativistic length contraction effect.

### 1.1.2 Gravitation and General Relativity

Among the known forces, gravitation is unique in that it accelerates everything, regardless of composition details. Attempts to directly include gravitation in Special Relativity failed, or implied modifications that led to General Relativity.
A classical justification for this incompatibility between gravitation and Special Relativity [4] comes from the gravitational redshift effect. Einstein introduced this effect as a classical energy conservation problem: a particle falling in a gravitational potential well gains some kinetic energy. If it is converted in a photon, of null mass, hence no potential energy, traveling out of the well, the energy difference could be extracted from the photon, in violation of energy conservation, unless it is also affected by gravitation and losses energy ( i.e. is red-shifted). Now, in a flat space-time, the propagation of light between observers at rest always follows similar world-lines. However, as light is also the distance or time reference, in the case of gravitational redshift a different delay elapses at the bottom and at the top of the well, which is in contradiction with the geometrical constraints of congruent world-lines propagation.
Hence gravitational redshift is required for energy conservation but it is not in agreement with flat space-time.

To guide the formulation of General Relativity, Einstein proposed an extended Equivalence Principle, that states that the classical Equivalence Principle remains valid, plus two propositions that concern any 'local non-gravitational test experiment' [3]: firstly that the outcome is independent of velocity, secondly that it would be identical everywhere in the Universe. Under these postulates, Newtonian inertial referentials are replaced by free-falling referentials.
This 'Einstein Equivalence Principle' allows the suppression of gravitation in free-falling referentials and thus the use of the Special Relativity framework and so-called 'locally inertial' coordinates :

$$ds^2 = (\frac{\partial X^\nu}{\partial x^\mu}\frac{\partial X^\beta}{\partial x^\nu}\eta_{\alpha\beta})dx^\alpha dx^\nu \tag{1.11}$$

As Einstein himself illustrated, a person locked in an elevator in free-fall would not be able to identify the effect of gravitation (in practice, tidal effects due to the inhomogeneity of the gravitational field would certainly betray it).

[3]The term is defined in [5]. It is a small-scale experiment performed in a shielded free-falling laboratory where self-gravitation effects are negligible.

### Curved space-time

**Geodesics** These reference objects replace the straight world-lines of classical mechanics. As summarized in *Gravitation* [4], 'A geodesic of space-time is a curve that is straight and uniformly parametrized, as measured in each local Lorentz frame [Special Relativity referential] along its way'. In the absence of gravitation, this coincides with the trajectory of classical isolated systems. In General Relativity , it applies *mutatis mutandis* for free-falling particles.

**Curvature tensors** The variation between neighbouring geodesics is described by the behaviour of the separation vector $\zeta$ linking them, perpendicularly to the chosen reference geodesic in the 'equation of geodesic deviation' :

$$\frac{D^2\zeta^\alpha}{d\tau^2} + R^\alpha{}_{\beta\gamma\delta}\frac{dx^\beta}{d\tau}\zeta^\gamma\frac{dx^\delta}{d\tau} = 0 \tag{1.12}$$

$\frac{D^2}{d\tau^2}$ is used following [4] to mark an arbitrary coordinate system.
The tensor $R^\alpha{}_{\beta\delta\gamma}$ is called the Riemann tensor. Its contraction $R_{\mu\nu} = R^\alpha{}_{\mu\alpha\nu}$ is the Ricci tensor.

**Fermi coordinates** For any universe line (a 1 dimensional structure in the 4 dimensions space-time) it is possible to build a local coordinate system $X^\alpha$ using the flat metric, such as $g_{\alpha\beta}(x)|_{line} = \eta_{\alpha\beta}$, with $\eta_{\alpha\beta}$ the special relativity metric, and $\frac{\partial g_{\alpha\beta}}{\partial X^\gamma}|_{line} = 0$. When applied to a geodesic, it is in addition possible to use proper time $X^0 = c\tau$. This is another indication of the adequacy of Special Relativity for locally inertial referentials.

### Effect of geometry on matter

The evolution from Special Relativity to include gravitation requires it is embedded in the metric. Strong constraints were imposed on the form of this modification: existing theories, Newtonian gravitation and Special Relativity, must be recovered in the limit of vanishing gravitational field and small velocities.
The main concern is to provide coordinate change rules between the local inertial referentials that are also satisfying for any other referential.
The always valid metric definition takes the general form

$$g_{\mu\nu} = \nabla_{\alpha\beta}\frac{\partial X^\alpha}{\partial X^\mu}\frac{\partial X^\beta}{\partial X^\nu} \tag{1.13}$$

To retain the referential-independent formulation of physical laws, a new 'covariant' derivation operator must be introduced :

$$\nabla_\nu T^{\mu\nu} = \partial_\nu T^{\mu\nu} + \Gamma_{\nu\sigma}{}^\mu T^{\sigma\nu} + \Gamma_{\mu\sigma}{}^\nu T^{\mu\sigma} \tag{1.14}$$

where the additional terms are factored by the Christoffel coefficients, defined by

$$\Gamma_{\lambda\mu}{}^\sigma = \frac{1}{2}g^{\nu\sigma}(\partial_\lambda g_{\mu\nu} + \partial_\mu g_{\lambda\nu} - \partial_\nu g_{\mu\lambda}) \tag{1.15}$$

This derivation operator replaces standard derivation everywhere in General Relativity. The local metric is the required form both to derive the motion of free-falling systems and, by coordinate change, that of accelerated bodies.

### Effect of matter upon geometry

As mentioned above, gravitation as a force disappears, to be replaced by the metric $g_{\mu\nu}$. The General Relativity generalization must take into account all forms of energy existing locally as sources of gravitation. These are described with the stress-energy tensor $T^{\mu\nu}$. For a perfect fluid of homogeneous mass-energy density $\rho$, isotropic pressure $p$ and local velocity $u$, it is built as :

$$T_{\mu\nu} = (\rho + p)u_\mu u_\nu + pg_{\mu\nu} \tag{1.16}$$

This is a symmetric tensor, containing much information: component $T^{00}$ is the local mass-energy density, $T^{0i} = T^{i0}$ are components of energy fluxes and the remaining terms correspond to stress. The Einstein tensor $(E_{\mu\nu})$ relates geometry and matter and was defined to verify the following properties :

- 0) $E_{\mu\nu} = E_{\mu\nu}(g, \partial g, \partial^2 g)$
- 1) $E_{\mu\nu} = kT_{\mu\nu}$
- 2) $\nabla_\nu E^{\mu\nu} = 0$
- 3) $E_{\mu\nu}(\eta_{\rho\sigma}) = 0$

This compact notation carries important physical constraints: from equation 0) the Einstein tensor is built only as a function of the metric and its derivatives, up to order 2. It must be linearly related - equation 1) - to the source of gravity, the stress-energy tensor. As a tensor it must be invariant by covariant differentiation -equation 2) - which is to say it is not affected by coordinate changes. And finally equation 3) recalls that in a flat space-time the Einstein tensor should vanish. The correct value for the coefficient $k$ is given by the Newtonian limit. The Newtonian Poisson equation also writes as $\Delta\phi = 4\pi\frac{T^{00}}{c^2}$, while the General Relativity limit is $\frac{2}{c^2}\Delta\phi = kT_{00}$. Hence the Einstein equation, those solutions will bring up gravitational waves :

$$E_{\mu\nu} = \frac{8\pi G}{c^4} T_{\mu\nu} \tag{1.17}$$

**The spherical star solution** A simple case of astrophysical relevance is the static spherical body, isolated in vacuum to have $E_{\mu\nu} = 0$ or $R_{\mu\nu} = 0$. Birkhoff's theorem (1923) shows that the spherical symmetry implies a static gravitational field outside the massive body, in spite of any -spherically symmetric- deformation of that body.
To solve the Einstein equation in this case, the 'curvature coordinates' metric is adapted :

$$ds^2 = -e^{\nu(r)}c^2dt^2 + e^{\lambda(r)}dr^2 + r^2(d\theta^2 + sin^2(\theta)d\phi^2) \tag{1.18}$$

The non-zero Christoffel coefficients are then $\Gamma^0_{\mu\nu}$.
For symmetry reasons, $g_{0i} = 0$ so the only non-zero terms are for $\rho = 0$. Besides, $\partial_\mu g_{00} = 0$ for $\mu \neq r$ and the same holds for $\nu$. Note also that $\Gamma^0_{\mu\nu} = 0$ except $\Gamma^0_{0r} = \Gamma^0_{r0} = \frac{1}{2}\frac{d\nu}{dr}$.
The Ricci tensor is, from the same symmetry arguments, given by:

$$\begin{cases} R_{\mu\nu} = 0 \text{ if } \mu \neq \nu \\ R_{\phi\phi} = sin^2(\theta)R_{\theta\theta} \\ R_{\theta\theta} = 1 + e^{-\lambda}(\frac{\lambda' - \nu'}{2}r - 1) \text{ obtained from } \frac{d.}{dr} \\ R_{00} = \frac{e^{\nu-\lambda}}{2}(\nu'' + \nu'\frac{\nu' - \lambda'}{2} + 2\frac{\nu'}{r}) \\ R_{rr} = -\frac{1}{2}(\nu'' + \nu'\frac{\nu' - \lambda'}{2} - 2\frac{\lambda'}{r}) \text{ with } R_{rr} \propto R'_{\theta\theta} \end{cases} \tag{1.19}$$

A linear combination of $R_{00}$ and $R_{rr}$ gives $\lambda + \nu = constant$. Adding the asymptotic behaviour $g_{\mu\nu} \xrightarrow[r\to\infty]{} \eta_{\mu\nu}$ requires $\lambda = -\nu$.
From there, $e^\nu(\nu' r + 1) = 1 = (e^\nu r)'$ or $g_{\nu 0} = -(1 + \frac{K}{r})$. The Newtonian limit is $K = -\frac{2GM}{c^2}$.
The expression of the metric for an isolated spherical body, that was first derived by Schwarzschild in 1916, is thus:

$$ds^2 = -\left(1 - \frac{2GM}{rc^2}\right)c^2dt^2 + \frac{dr^2}{1 - \frac{2GM}{rc^2}} + r^2(d\theta^2 + sin^2(\theta)d\phi^2) \tag{1.20}$$

Note that the singularity at $r_S = \frac{2GM}{c^2}$, called the Schwarzschild radius, is introduced by the coordinate system. It disappears when spherical coordinates are replaced by the isotropic system where $ds^2 = f_1(\rho)c^2dt^2 + f_2(\rho)(d\rho^2 + \rho^2 d\Omega^2)$ with $\rho = A(\sqrt{r} + \sqrt{r - r_S})^2$. The metric then becomes :

$$ds^2 = -\left(\frac{1 - \frac{GM}{2\rho c^2}}{1 + \frac{GM}{2\rho c^2}}\right)c^2dt^2 + \left(1 + \frac{GM}{2\rho c^2}\right)^4(d\rho^2 + \rho^2 d\Omega^2)dx^2 \tag{1.21}$$

The remaining singularity at $\rho = 0$ is of physical origin: it corresponds to a point-mass, which implies an infinite mass density.
The Schwarzschild radius is nonetheless a relevant parameter: for a particle trying to leave the

influence of the massive body, the required escape velocity at $r_{start} = r_S$ is the speed of light. That is to say particles located at $r_{start} \leq r_S$ are bound to the central body. Which implies that what happens at $r < r_S$ is not accessible. Hence the Schwarzschild radius is called the horizon of the massive body. This behaviour has been popularized, notably by Hawking's best-seller [9], for black holes, which are space-time singularities : masses without a physical extension, or infinite density. This is not a commonly observed phenomenon, because for 'ordinary' objects, even stars, $r_S$ is much smaller than the size of the body. And the conditions set above to derive the Schwarzschild solution apply only outside the mass distribution.

For a rotating body, the spherical symmetry is broken as angular momentum $J$ opposes the gravitational pull, so the above calculation does not hold. An horizon still appears, from the spherical coordinates (rotation axis $\theta = 0$ here) Kerr metric :

$$\begin{aligned} ds^2 = \left(1 - \frac{2GM_{star}}{\rho c^2}\right)dt^2 - \left[\frac{4GM_{star}ra\sin^2(\theta)}{\rho c}dtd\phi \right. \\ \left. + \frac{\rho}{\Delta}dr^2 + \rho d\theta^2 + \left(r^2 + a^2 + \frac{2GM_{star}ra^2\sin^2(\theta)}{\rho c^2}\right)\sin^2(\theta)d\phi^2\right] \end{aligned} \tag{1.22}$$

for a $\dot{\phi} > 0$ rotation, with $a = J/(Mc)$, $\rho = r^2 + a^2\cos^2(\theta)$ and $\Delta = r^2 - (2GM_{star}r/c^2) + a^2$. While cylindrical symmetry is maintained, the horizon is shaped along the angle $\theta$, from a maximum radius on the equatorial plane to a minimum along the rotation axis. Overall the horizon delimits a smaller volume for the Kerr solution than for Schwarzschild's.

### 1.1.3 Gravitational waves

There is no generic coordinate-independent definition of gravitational waves . To obtain simple formulas, it is reasonable to consider an almost flat space-time, devoid of matter ($T_{\mu\nu} = 0$) outside of the source, to obtain the development :

$$g_{\mu\nu} = \eta_{\mu\nu} + h_{\mu\nu} \tag{1.23}$$

$$\Box h_{\mu\nu} = 0 \tag{1.24}$$

Simplifications in the analytic expressions are obtained using the 'transverse-traceless' gauge (TT). For $h$ the trace of $h_{\mu\nu}$, the new metric perturbation becomes $\bar{h}_{\mu\nu} = h_{\mu\nu} - \frac{1}{2}\eta_{\mu\nu}h$, of null trace, and other quantities can be derived accordingly.
For an observation far from the source, plane wave solutions are a good starting point. From equation 1.24, the plane wave solution $\bar{h}_{\mu\nu} = C_{\mu\nu}e^{ik_\sigma x^\sigma}$ (with $C_{\mu\nu}$ a tensor) is correct, provided $k_\sigma k^\sigma = 0$. This is obtained for $k_\sigma = (\omega, k^1, k^2, k^3)$ and $\frac{\omega}{c}^2 = \delta_{ij}k^ik^j$: the plane wave propagates at the speed of light, with angular frequency $\omega$.

#### Propagating perturbations of the metric

Using the Fourier decomposition of the Einstein equation with a source term (that is for $T_{\mu\nu} \neq 0$), it can be shown [8] that plane waves provide base of solutions under the far-field hypothesis.

From that analytical manipulation, the physical solution (that propagates forward in time) is derived with retarded-time potentials :

$$\bar{h}_{\mu\nu}(t, \mathbf{x}) = \frac{4G}{c^4}\int \frac{1}{|\mathbf{x} - \mathbf{y}|}T_{\mu\nu}(t - |\mathbf{x} - \mathbf{y}|/c, \mathbf{y})d^3y \tag{1.25}$$

For a slowly moving source, seen from a long distance D, it is useful to introduce the (reduced) quadrupole moment tensor $\bar{q}_{ij}(t) = 3\int y^iy^jT^{00}(t, \mathbf{y})d^3y$ built from the energy density of the source. Using this quantity, the gravitational wave produced by a non-relativistic object at large distance is :

$$\bar{h}_{ij}(t, \mathbf{x}) = \frac{2}{3D}\frac{G}{c^4}\frac{\partial^2\bar{q}_{ij}}{\partial t^2}(t - D/c) \tag{1.26}$$

**Illustration of gravitational wave production** To produce a varying gravitational field takes a mass distribution away from spherical symmetry, with a significant second derivative for the quadrupole moment. These conditions are met by binary stellar systems.

Under the hypotheses of 1.1.3, that imply a weak gravitational field, the orbital motion of the system can be described using Newtonian mechanics. As a first approximation of the system, consider two identical point masses of mass M in circular orbit at radius r of the mass barycenter. The angular frequency of the orbit is $\Omega = (\frac{GM}{4r^3})^{1/2}$, from which the parametric path of the bodies and the energy density can be obtained. Choosing the motion to be in the ($x^1$, $x^2$) plane, with axis $x^3$, the quadrupole moment follows :

$$\begin{cases} q_{11} = & 3Mr^2(1+cos(2\Omega t)) \\ q_{22} = & 3Mr^2(1-cos(2\Omega t)) \\ q_{12} = & q_{21} = 3Mr^2 sin(2\Omega t) \\ q_{i3} = & 0 \end{cases} \tag{1.27}$$

and the metric perturbation:

$$\bar{h}_{ij}(t,\mathbf{x}) = \frac{8GM}{Dc^4}\Omega^2 r^2 \begin{pmatrix} 0 & 0 & 0 & 0 \\ 0 & -cos(2\Omega(t-D/c)) & -sin(2\Omega(t-D/c)) & 0 \\ 0 & -sin(2\Omega(t-D/c)) & cos(2\Omega(t-D/c)) & 0 \\ 0 & 0 & 0 & 0 \end{pmatrix} \tag{1.28}$$

The related energy loss for the system, that translates into an orbital-radius shrinkage (and thus an angular frequency increase), can be represented [10] via the radiated power :

$$P = \frac{G}{5c^5}[\frac{d^3Q^{ij}}{dt^3}\frac{d^3Q_{ij}}{dt^3}] \tag{1.29}$$

where $Q_{ij}$ is the traceless part of the quadrupole moment ($Q_{ij} = q_{ij} - \frac{1}{3}\delta_{ij}\delta^{kl}q_{kl}$). For a circular-orbit equal-mass binary system, the energy loss over a period of motion is :

$$P = \frac{2}{5}\frac{G^4M^5}{(rc)^5} \tag{1.30}$$

**Point of view of the observer**

The plane wave equation is still a fairly generic solution, with 10 coefficients from $C_{\mu\nu}$ and 3 from $k_\sigma$ to be fixed. Specifying the coordinate system, it is possible to reduce the number of free parameters to 3. In the TT gauge, for a wave propagating along $x^3$, the solution further simplifies in :

$$C_{\mu\nu} = \begin{pmatrix} 0 & 0 & 0 & 0 \\ 0 & C_{11} & C_{12} & 0 \\ 0 & C_{12} & -C_{11} & 0 \\ 0 & 0 & 0 & 0 \end{pmatrix} \tag{1.31}$$

and $k_\sigma = (\omega, 0, 0, \omega/c)$.

**Interpretation using Fermi coordinates** To satisfy the conditions for Fermi coordinates, consider the neighbourhood of a geodesic A. There the metric is expressed as

$$g_{\alpha\beta}(x) = \eta_{\alpha\beta} + O(x^2) \tag{1.32}$$

with $g_{00}(x) = -1 - R^{Fermi}_{0i0j}(x,0)x^ix^j + O(x^3)$. This gives

$$\frac{d^2x^i}{dt^2} = -c^2R^{Fermi}_{0i0j}x^j + O(x^2) \tag{1.33}$$

Change the coordinate system according to the hypotheses of paragraph 1.1.3: $\frac{\partial x^\mu}{\partial x^\alpha} = \delta^\mu_\alpha + O(h)$. The resulting Riemann tensor is invariant in h to the first order, hence :

$$R^{Fermi}_{0i0j} = R^{TT}_{0i0j} + O(h^2) = -\partial^2_\nu h^{TT}_{ij} = -\frac{1}{2c^2}\frac{\partial^2}{\partial t^2}h^{TT}_{ij} + O(h^2) \tag{1.34}$$

Thus motions around A are described by :

$$X^i(t) = X^i(0) + \frac{1}{2}h^{TT}_{ij}(t,0)X^j(0) + O(h^2) \tag{1.35}$$

Note $C_{11} = C_+$ and $C_{12} = C_\times$.

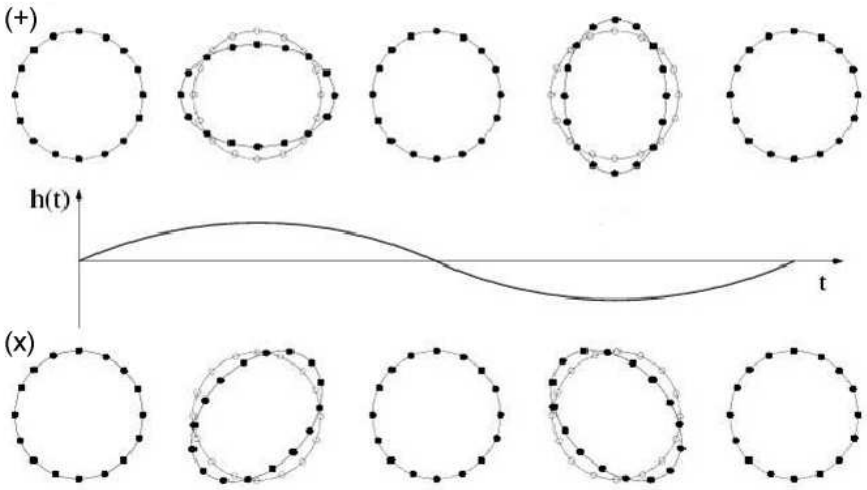


**Figure 1.1:** Motion of a circle of test masses over a period in a gravitational wave with normal incidence. The two polarizations (+) and (×) are shown separately, with respect to the wave amplitude $h(t)$.

**Measurable effect** In the plane normal to the wave incidence (say $x^3$), the motion for a zero-origin test mass can be approximated as :

$$\begin{cases} x = & \frac{1}{2}\left(C_+ \cos(\omega(t-\frac{z}{c})\right) + \left(C_\times \cos(\omega(t-\frac{z}{c}))\right) \\ y = & \frac{1}{2}\left(C_\times \cos(\omega(t-\frac{z}{c})\right) - \left(C_+ \cos(\omega(t-\frac{z}{c}))\right) \end{cases} \tag{1.36}$$

When $C_\times = 0$, the gravitational perturbation is noted $h_+$, the $x$ and $y$ coordinates of the test mass oscillate orthogonally: when $x^1$ increases, $x^2$ decreases and conversely. When $C_+ = 0$, the effect ($h_\times$) is similar but rotated at 45 degrees, the rotation angle transforming $\begin{pmatrix} 0 & 1 \\ 1 & 0 \end{pmatrix}$ into $\begin{pmatrix} 1 & 0 \\ 0 & -1 \end{pmatrix}$.
The two motions $h_+$ and $h_\times$ are orthogonal so any gravitational wave can be decomposed on these two polarizations. This specific motion pattern, illustrated for test masses set along a circle in figure 1.1, is connected to the quadrupolar nature of the gravitational radiation, as opposed to electromagnetic waves.
For a discussion on the difficulty of a classical interpretation for this General Relativity effect, see for instance [11].

It can be shown that axi-symmetric systems would emit linearly polarized gravitational waves. This could to some extent apply for stellar collapse. More generally, waveform interpretation allows to distinguish source types. This point is illustrated in paragraph 1.3 on astrophysical sources.

## 1.2 Detectors

### 1.2.1 General introduction

The first detectors developed in the 1960's were cylindrical metal bars, with a mechanical resonance mode that should be excited by a gravitational wave . There are currently many such instruments in operation [12], with the advantage of a long joint data taking period [13], though still limited in sensitivity to very narrow frequency bands, in spite of regular improvements.
The most sensitive (over a reasonably large frequency band) gravitational wave detectors built or planned all rely on another physical principle, the predicted effect of a passing gravitational wave on free-falling test masses, presented in section 1.1.3. As seen above, the distance between

test-masses, as measured by light time of flight, will be modified.
This thought experiment has been transposed in giant interferometers of similar principle. Five instruments are in operation, from four collaborations, with LIGO [14] (two sites) and Virgo [16] the largest, at respectively 4 and 3 km. Complete sky coverage, detection reliability and source direction estimation are not attained yet, as a full-time network [15] of more than three instruments would be necessary.
The architecture of these instruments and its effect on data analysis is briefly presented, through the example of Virgo.

### 1.2.2 Interferometry

The core experimental setup is the Michelson interferometer. It compares the phase of two light beams following separate paths, defined by reflective end mirrors ($m_1$ and $m_2$) and a central semi-reflective mirror called the beam splitter. In a Michelson interferometer, a laser source of frequency $\omega$ and power $P_{in}$ is injected, and the output is measured on an exit optical port. For an arm length difference $\Delta l = l_1 - l_2$, the light beams accumulate a phase difference $\phi = 2\frac{\omega}{c}\Delta l$ that gives an output power :

$$P_{out} = \frac{P_{in}}{2}[1 + C \times \cos(\phi)] \tag{1.37}$$

where the optical characteristics of the mirrors (their reflectivity $r_i$) are summarized by the contrast $C = \frac{2r_1 r_2}{{r_1}^2+{r_2}^2}$. This formula is only valid for the described simple setup, not for more sophisticated configurations.

This is just the measurement principle needed to observe the effect of a gravitational wave : a 'gravitational wave crossing' will add a small phase difference $\phi = \phi_0 + \phi_{GW}$. A limited expansion to first order of equation 1.37 in $\phi_{GW}$ gives :

$$P'_{out} \simeq \frac{P_{in}}{2}[1 + C\cos(\phi_0) - C\sin(\phi_0)\phi_{GW}] \tag{1.38}$$

implying an output power fluctuation of:

$$\delta P^{GW}_{out} \simeq \frac{P_{in}}{2} C sin(\phi_0)\phi_{GW} \tag{1.39}$$

Interesting values for $\phi_0$ are $\phi_0 = 0[2\pi]$, where $P_{out}$ will be maximum and $\phi_0 = \pi[2\pi]$, the minimum of $P_{out}$. These translate in favored length differences : $\Delta l = k\frac{\lambda}{2}$ for the white fringe, of maximum output power, and $\Delta l = (k + \frac{1}{2}) \times \frac{\lambda}{2}$ for the opposite case, the dark fringe, with $k \in \mathbb{N}$. By making the output proportional to the length asymmetry of the arms $\Delta L = l_1 - l_2$, of mean symmetrical length $L = \frac{l_1+l_2}{2}$, dark fringe tuning allows to directly measure the gravitational wave effect, while suppressing noise components that equally affect both arms. This makes the interferometer a *null instrument*, as exposed in [17].
The gravitational wave signal amplitude measured by the interferometer is directly the ratio between apparent length variation and total length $h \simeq \frac{\Delta L}{L}$. Coupling between a gravitational wave and the instrument transforms a length variation in a light phase change, that can be measured as a light power fluctuation. The efficiency of this conversion depends on relative orientation between the incidence direction and instrument axes.

#### Geometrical acceptance

Given the source sky position ($\alpha$, $\delta$) and the detector position on Earth ($l$, latitude, and $L$, longitude), and the signal polarization $\psi$ the amplitude is :

$$h_{ITF}(t) \approx \frac{\Delta L}{L} = F_+(\alpha, \delta, \psi, l, L, t)h_+(t, source) + F_\times(\alpha, \delta, \psi, l, L, t)h_\times(t, source) \tag{1.40}$$

with $F_+$ and $F_\times$ the antenna coefficients of the instrument. The chosen geometrical coordinates are time-independent, so the effect of the rotation of the Earth must be introduced in the beam pattern coefficients, which gives a cumbersome equation. In the local coordinates of an interferometer, where the source direction is defined by the time-varying spherical coordinates ($\Theta$,$\Phi$) and polarization angle $\Psi$, a much simpler expression is possible :

$$F_+ = \frac{1}{2}(1 + \cos^2(\Theta))\cos(2\Phi)\cos(2\Psi) - \cos(\Theta)\sin(2\Phi)\sin(2\Psi) \tag{1.41}$$

$$F_\times = \frac{1}{2}(1 + \cos^2(\Theta))\cos(2\Phi)\sin(2\Psi) - \cos(\Theta)\sin(2\Phi)\cos(2\Psi) \tag{1.42}$$

A more complete derivation of the geometric acceptance of an gravitational wave detector can be found in [15]. An illustration of the coverage achieved by a single instrument is given in figure 1.2.

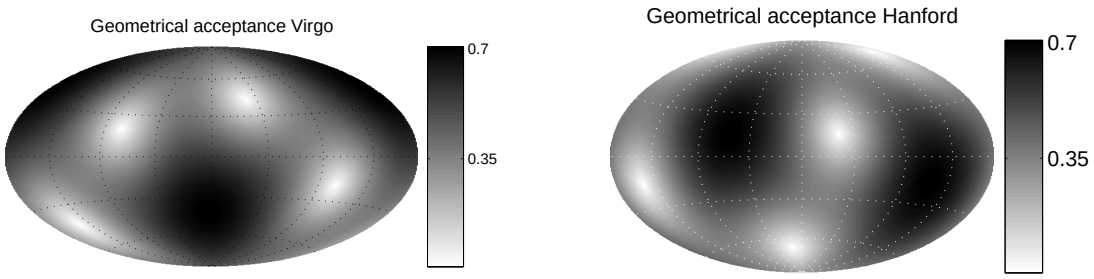


**Figure 1.2:** Antenna coefficient for two interferometers, Virgo and LIGO Hanford, at the same moment, in Galactic coordinates and Hammer Aitoff projection. The value is averaged over polarization angles, hence it never reaches 1.

#### Optical noises

The fundamental quantum uncertainty on any position measurement (the Heisenberg relation) can be expressed as two separated optical noises: the radiation pressure by the laser beam on the mirrors and the photon counting noise, or shot noise. Their spectral density, in $mHz^{-1/2}$, are :

- Radiation pressure : $\hat{x}_{radiation}(f) = \frac{1}{Mf^2}\frac{\sqrt{2\hbar P}}{2\pi^3 c\lambda}$ for a light power P.
- Photon shot noise : $\hat{x}_{photon} = \sqrt{\frac{\hbar c\lambda}{2\pi P_{in}}}$, a frequency-independent spectral density.

Combining these two noise sources, one recovers the standard quantum limit $\hat{x}_{quantum}(f) \approx \frac{1}{fL}\frac{\bar{h}}{M}$ for an object of mass M and a measurement of duration $\Delta t = 1/f$.

These noise sources must be balanced to minimize the noise level in the frequency band of interest. Existing continuous laser sources have a low power ($P \leq 100W$), so the radiation pressure noise is negligible compared to photon shot noise. The reduction of shot noise is a good argument using the dark fringe configuration already mentioned. Actually, the detailed computation shows that the shot noise minimum is reached near the dark fringe, the exact position depending on the contrast of the interferometer.

### 1.2.3 Instrumental choices

To properly dimension an actual instrument, it is important to quantify the limits on measurement performances, and scale or adapt the initial setup.

#### Optical scheme enhancements

To increase the interferometer arm length seen by the light beams, Fabry-Perot cavities are added, by introducing a mirror between the extremity of each arm and the beam splitter. These affect both the effective arm length and the energy stored in the instrument :

$$L_{optical} = L_{arm}\frac{2\mathrm{F}}{\pi} \quad \text{for F the cavity finesse.} \tag{1.43}$$

$$P_{Fabry-Perot} = P_{in}\frac{T_{in}}{(1 - r_{in}r_{end})^2}. \tag{1.44}$$

The maximum stored power depends on the optical coefficients, amplitude reflectivity $r_{mirror}$ and energy transmitivity $T_{mirror}$ of the mirrors forming the Fabry-Perot cavity, with '$in$' the light input. In Virgo, the equivalent optical length reaches 100 km.

Besides, since the available power remains far lower than required for an important radiation pressure contribution, it is acceptable to increase this power through modifications of the optical scheme. A semi-reflexive mirror is added between the beam-splitter and the laser source. With the instrument tuned on a dark fringe, most of the light power goes not to the output optical port but back at the entrance port. Thus the extra mirror will recycle this light back into the optical cavity. Virgo achieves a recycling gain of the order of 50 on $P_{in}$.

**Meeting the free fall condition**

The interaction between a gravitational wave and test-masses, as deduced by General Relativity, requires an experimental condition of free-fall. For a ground instrument, this condition is sought on the horizontal measurement axes. To this end, each test-mass (each mirror of the interferometer ), is attached to a pendulum, or chain of pendulums.
For an isolated free-falling mass, subject to a force $\vec{F}$, the projected equation of motion, on any axis $\vec{x}$, is $F_x = m\ddot{x}$, or, using the Fourier transform, $\frac{\hat{F}_x(\omega)}{-m\omega^2} = x(\omega)$. Now consider a mass, suspended to a pendulum of length $l$, attached at a point $x_0$ assumed to be fixed, and subject to an external force $\vec{F}$. The equation of motion on a horizontal axis, within the small angles approximation and without energy dissipation, is :

$$F_x(t) - m{\omega_0}^2[x(t) - x_0] = m\ddot{x} \tag{1.45}$$

with $\omega_0 = \sqrt{\frac{g}{l}}$ the proper frequency of the pendulum. Applying the Fourier transform gives :

$$x(s) = \frac{\hat{F}_x(\omega)}{m(\omega_0^2 - \omega^2)} \tag{1.46}$$

Hence for frequencies above the pendulum proper mode, such as $\omega_0 << \omega$, it is possible to neglect $\omega_0$, that is to say gravity, so the apparatus behaves basically like a free mass.

The obvious drawback with suspended components is that any external excitation will disturb each part the system independently. As ground experiments cannot be completely isolated from the environment, mechanically nor thermally, as mentioned in section 1.2.5, the optical configuration must be actively maintained. Distances and alignments must remain within tight limits of the operation point. This implies continuous measurement and correction of several degrees of freedom, and constitutes the control of the instrument [18].

**Phase modulation**

Measurement of the arm-length fluctuations is done on a phase-modulated light beam, built using non-linear optics (Pockels cells). In this scheme the output light carries information on three phase frequencies, the 'carrier' frequency $f_c$, given by the light wavelength, and two side-bands $f_c - f_{mod}$ and $f_c + f_{mod}$. When a phase shift $\Phi_{sig}$ (or $\Delta L$ variation) affects the light beam, the output power is amplitude-modulated at frequency $f_{mod}$ with an amplitude proportional to $\sin(\Phi_{sig})$.
This information constitutes an error signal that can drive a feed-back loop to control the instrument.

### 1.2.4 Control and noise coupling in Virgo

As mentioned above, Virgo must be actively kept at its working point. A large part of the commissioning of the instrument has been dedicated to designing a full set of control algorithms. These follow the classical scheme of control theory, with an error signal being computed from the quantity to be controlled, which is then altered to reduce the deviation.
Control loops are well-studied objects, yet a complex system like Virgo, with a large number of degrees of freedom, requires many such loops. This complexity has two main consequences. Firstly, dependencies are created between loops, either due to a coupling of the quantities they control or constraints that must be satisfied for nominal operation. Secondly, noise can propagate between physically separated parts of the instrument through a control loop, thus complicating the interpretation of the output signal.
As understanding the output of the instrument depends on a correct knowledge of its behaviour, laying out the control loops as they are defined now is important.

The number of photo-diode signals is multiplied by the use of the demodulation scheme. For every measured 'DC' power signal [4], two demodulated signals in phase quadrature are available for each demodulation frequency.
The longitudinal control of Virgo, for instance, using the signals from the 'B' photo-diodes of figure 1.3, deals with four independent inter-mirrors lengths, noted $d(mirror_1, mirror_2)$ below (following the naming convention of figure 1.3) :

[4] As the sensitive disk of a quadrant photo-diode is split in four sectors, it provides four such DC signals

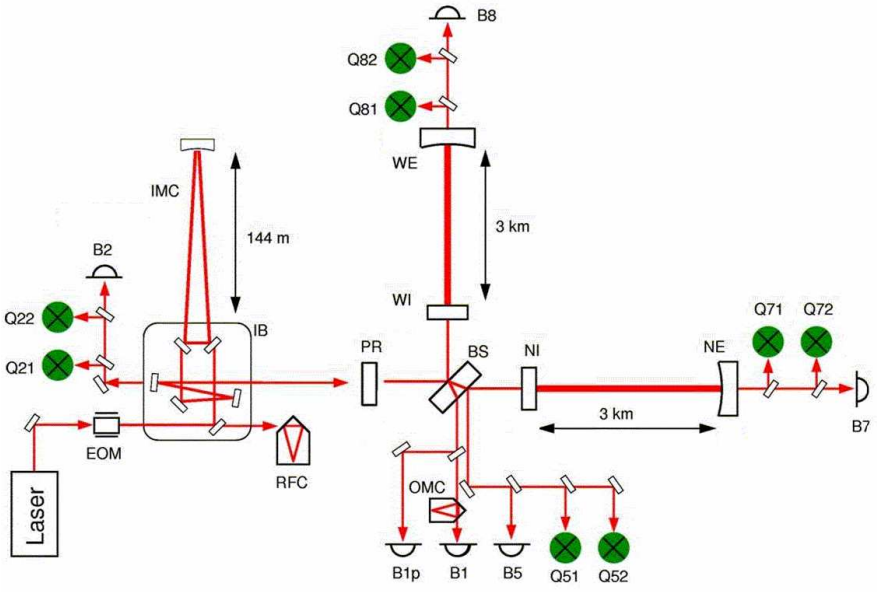


**Figure 1.3:** The mirrors are named according to their position on the West or North arm, at the Input or the End of a Fabry-Perot cavity (WI, WE, NI, NE). Two types of photo-diodes are visible: $B_i$ are standard photo-diodes, while $Q_i$ are quadrant-photo-diodes. Also noted are the Input and Output Mode Cleaners (IMC and OMC) and the Reference Frequency Cavity (RFC).

- MICH: the Michelson length, $d(BS, WI) - d(BS, NI)$
- PRCL: Power recycling mean length, $d(PR, BS) + \frac{d(BS,WI)+d(BS,NI)}{2}$
- DARM: differential arm length, $d(NE, NI) - d(WE, WI)$
- CARM: common arm length, $d(NE, NI) + d(WE, WI)$

that are related to the photo-diode signals *via* an optical matrix :

$$\begin{pmatrix} MICH \\ PRCL \\ DARM \\ CARM \end{pmatrix} = \begin{pmatrix} Optical \\ Matrix \end{pmatrix} \times \begin{pmatrix} Photo-diode \\ signals \end{pmatrix} \tag{1.47}$$

The optical matrix, as experimentally measured, is not diagonal, which introduces the possibility of contamination between quantities that should be independent. The improvements of the control strategy have been visible in the reduction of the noise below 200 Hz. More details, notably a description of the control strategy, are available in [19].

The same approach is used to align the mirrors and check their angular motion, with the quadrant photo-diodes. It is worth noting, as they affect the operation of the instrument, supplementary quantities actively controlled. One is the laser frequency, compared to two reference optical cavities (a small low-expansion material cavity and the whole interferometer ). Another one is the motion of the suspension system, called in Virgo the 'super-attenuator', at very low frequencies, influenced by tidal effects and seismic activity.

### 1.2.5 Assessment of instrumental noise for Virgo

A few noise sources, secondary with respect to the above fundamental limits, complete the actual sensitivity of the instrument :

- Seismic noise : Ground vibrations locally couple to instrument parts.
- Thermal noise : Thermal excitation feeds mechanical resonances.

The spectral power density of seismic noise on reasonably quiet sites is approximately described by :

$$\hat{x}_s(f) \approx \frac{10^{-7}}{f^2} \quad (\mathrm{mHz}^{-1/2}) \tag{1.48}$$

To limit the influence of seismic noise, pendulums are again called upon, specifically for the isolation they provide at frequencies above the pendulum resonance frequency. Combining several pendulums into a 'super-attenuator', as described in [20], it is possible to suppress very efficiently seismic noise transmission for frequencies above a few Hertz. The contribution of seismic noise to the detector then becomes :

$$\tilde{h}_{seismic}(f) \approx \frac{2}{3000}\sqrt{(\frac{1}{f^{14}})^2 + [2.35 \times 10^{-4}\frac{1}{f^{12}}]^2} \times 10^{-11}(\frac{10\mathrm{Hz}}{f})^2 \quad (\mathrm{Hz})^{-1/2} \tag{1.49}$$

This noise term is dominant below 4 Hz and negligible above 10 Hz.

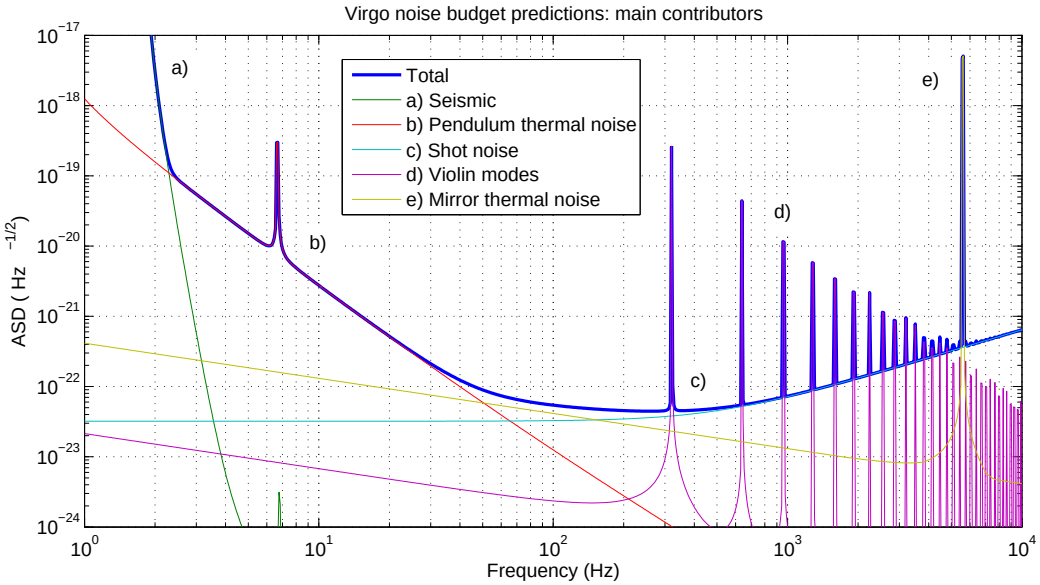


**Figure 1.4:** Virgo target noise budget, from [22].

Thermal noise is only penalizing for mechanical elements with resonant modes that interact with the laser beam. This includes the mirrors and their suspension system. The suspension wires that hold the mirrors behave like taut violin cords, while for the mirrors an analogy to drums is correct. These resonances, fed by thermal noise [5], introduce high spectral power features, identified as thermal lines. They are modeled as harmonic oscillators [21] and contribute globally to the noise budget as :

$$\tilde{x}_{thermal}(f) = \frac{1}{3000}\sqrt{\frac{4k_BT}{f}} \times \sqrt{\sum_{n=1}^{\infty} \frac{1}{(2\pi)^3 M_n f} \frac{{\nu_n}^2 \phi_n(f)}{({\nu_n}^2 - f^2)^2 + {\phi_n}^2(f){\nu_n}^4}} \quad (\mathrm{Hz})^{-1/2} \tag{1.50}$$

where, for each oscillation mode $n$, $\phi_n$ is the loss angle, defining the energy dissipation over a period of motion and $M_n$ an equivalent mass (distinct from the inertial mass actually involved) to be estimated. From the terms after the summation symbol in equation 1.50, the spectral density for each thermal noise component has three parts: at $f \simeq \nu_n$ the resonance peak, for $f \ll \nu_n$ a slope in $f^{-1/2}$, for $f \gg \nu_n$ a much larger slope in $f^{-5/2}$. This shape has a critical impact on the sensitivity curve of Virgo, up to 1 kHz.

[5] Note that the connection between mechanical and thermal systems started with Einstein, who proposed the correct interpretation to Brownian motion.

Indeed the mirror suspension has a pendulum mode (rigid bar motion) at 0.6 Hz with a very large quality factor and a vertical oscillation mode at 6.7 Hz (from the vertical-motion attenuation stages), converted into horizontal motion by the curvature of the Earth between the mirrors (tilted with respect to each over). The pendulum mode is excited by seismic noise, very large at low frequency. Its $f^{-5/2}$ tail is therefore the dominant feature up to 50 Hz, as shown in figure 1.4. It is important to note that the integrated contribution from a thermally excited resonance does not depend on its parameters. To mitigate it impact, it is however possible to concentrate most of the energy in a very narrow frequency band, around the resonant frequency.
This choice forces the selection of materials with high quality factors, and explains the forest of lines predicted for the instrument sensitivity, due to the resonances of the suspension wires (the violin modes) and the deformation of the mirrors themselves (drum modes). While the former only affect sensitivity at their resonance frequency, the later have important below-resonance tails that strongly contribute to limit the sensitivity between 50 Hz and 1 kHz, although their resonance frequencies are above 5.5 kHz.
Violin modes, as detailed in [22], are harmonics of a 320 Hz fundamental (more accurately, one fundamental frequency per suspension wire). More details are provided in Chapter 3, dedicated to resonances.

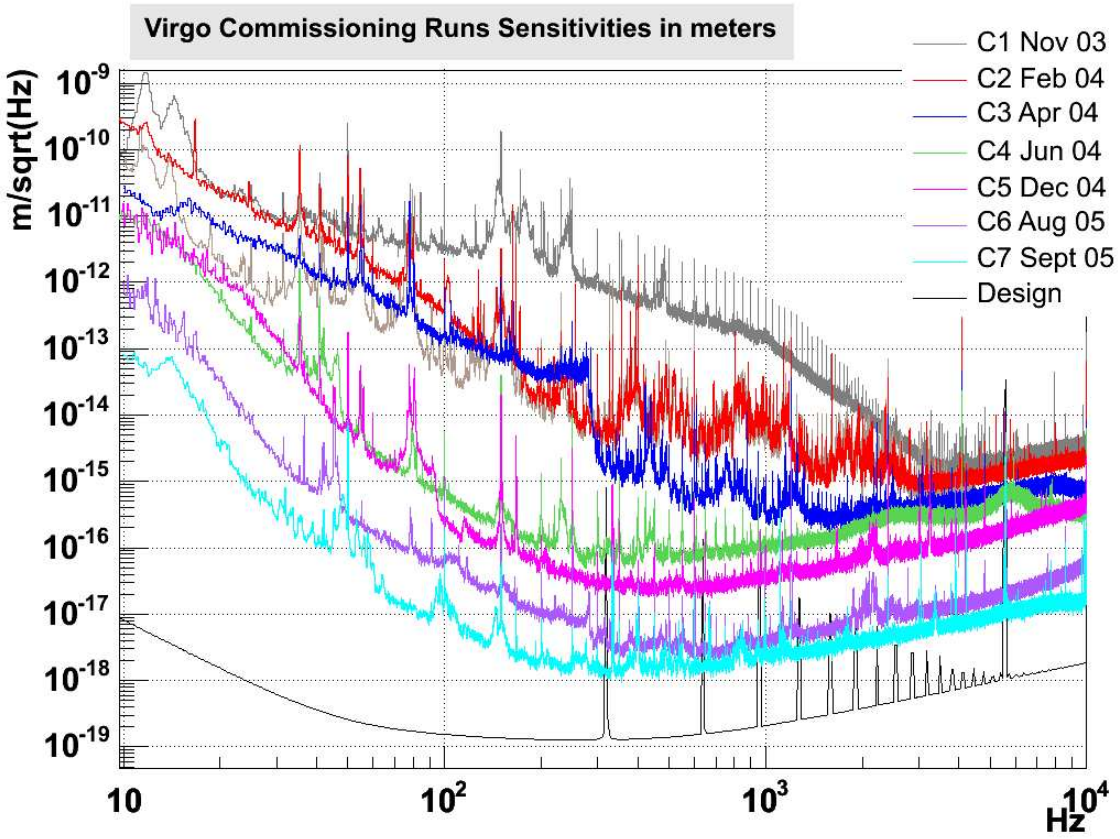


**Figure 1.5:** Virgo sensitivity evolution during the Commissioning phase.

### Commissioning of Virgo

An additional limitation to the sensitivity comes from the complex nature of the instrumental noise. Variations on all time-scales have been observed, that are not well described using a Gaussian noise model. The target sensitivity has not been reached yet, though progress is continuous. Figure 1.5 illustrates successive steps in the optical setup and instrument control.
In the Commissioning run C1 and C2, the configuration included only one Fabry-Perot cavity at the time. The Michelson interferometer was controlled from C3 on, with an improved automatic optical alignment for C4, in June 2004. The last mirror, for power recycling, was controlled in December 2004 for C5, with a reduced input power, to suppress instability due to back-scattered light.

A permanent solution was designed, to be implemented during the hardware update scheduled for Summer 2005. This lowered power did not prevent sensitivity improvements in C6 and C7, organized before the shutdown, in relation to finer control and optical alignment strategies. Besides gains on sensitivity, the stability of the operating point increased between C5 and C7, allowing for longer continuous data segments, up to 40 hours during C6 and 14 hours in C7, where occasional control tunings were required.
The observed behaviour of the instrument at its best sensitivity so far is the subject of Chapter 4.

## 1.3 Astrophysical sources

Embarking on a gravitational wave observation program, it is useful to survey what source populations exist, the rate of observation, the signals they would generate and the information that could be extracted. The indications below are optimistic, since they assume a complete and permanent sky coverage and an optimal signal recovery, guaranteed only when the waveform is known [23].

Production of gravitational waves only depends on the dynamics of high mass density systems. This implies a decoupling from static or low density masses and independence from mechanisms for electromagnetic emission, that constitutes the bulk of existing astrophysical data. For this reason, gravitational waves are a potentially rich source of information on so far unaccessible objects and matter states.

### 1.3.1 Astrophysical approximations

The first parameter to consider for a gravitational wave source is the emitted power, roughly estimated using :

$$P \approx \frac{c^5}{G}\alpha^2 \left(\frac{R_s}{R}\right)^2 \left(\frac{v}{c}\right)^6 \tag{1.51}$$

where R and $v$ are the characteristic size and velocity of the source, $R_S$ the Schwarzschild radius for the source and $\alpha$ an asymmetry parameter for the mass distribution ($\alpha = 0$ for spherical symmetry).
Hence critical parameters are compactness ($R \to R_S$), velocity ($v \to c$) and object asymmetry. Compactness, noted $\epsilon = \frac{R}{R_s} = 2\frac{GM}{Rc^2}$ reaches 0.2 for neutron stars and 1 at the horizon of a non-rotating black hole, compared to $\epsilon < 10^{-5}$ for the weak field conditions met in the solar system.
Several types of astrophysical objects satisfy these criteria and are therefore good gravitational wave candidate sources. Signal frequency should also fall in the surveyed range, say 10 Hz - 10 kHz for ground interferometers.
Here follows a brief review of potentially observable objects and the accessible populations.

### 1.3.2 Binary systems

The emission of gravitational waves by a close-orbit pair of compact objects was already mentioned. This General Relativity prediction is consistent with the high precision measurements obtained from the binary pulsar PSR 1913+16, discovered by Hulse and Taylor. A review of radio observation of relativistic systems can be found in [24].

#### Inspiral phase

This energy loss induces a reduction of the distance between the two objects, and the associated increase in orbital velocity. This is the so-called inspiral phase, whose catastrophic ending is the fusion of the two bodies. As details of the nature of the objects is secondary in their production, gravitational waves produced during this phase have been described with great precision, for instance in [25].
The quadrupole approximation, for a system of masses $M_1$ and $M_2$, at distance $d$, seen with an inclination angle $i$ from its rotation axis, gives, see for instance [26], two gravitational wave

polarizations :

$$h_+ = \frac{4(G\mathcal{M})^{5/3}}{dc^4}\frac{1+\cos^2(i)}{2}(\pi f(t))^{2/3}\cos(\phi(t)) \quad (1.52)$$

$$h_\times = \frac{4(G\mathcal{M})^{5/3}}{dc^4}\cos(i)(\pi f(t))^{2/3}\sin(\phi(t)) \quad (1.53)$$

with $\mathcal{M} = \mu^{3/5}M^{2/5}$ the chirp mass, $M = M_1 + M_2$ the total mass and $\mu = \frac{M_1 M_2}{M_1+M_2}$ the reduced mass of the system. In the above equation, the signal frequency (twice the orbital frequency) and phase vary with time. In the Newtonian approximation, for a set merger time $t_c$, they behave as :

$$\phi(t) = -2\left(\frac{G^{5/3}}{c^5}\right)^{-3/8}\left(\frac{t_c - t}{5\mathcal{M}}\right)^{5/8} \quad (1.54)$$

$$f(t) = \frac{1}{\pi}\left(\frac{256}{5}\frac{(G\mathcal{M})^{5/3}}{c^5}(t_c - t)\right)^{-3/8} \quad (1.55)$$

The detection range for inspiraling neutron star-neutron star binaries has been estimated for the target Virgo sensitivity in [27] as :

$$d \approx 20Mpc\left(\frac{\mathcal{M}}{1.22M_\odot}\right)^{5/6} \quad (1.56)$$

Analysis techniques used for this search should allow the identification of the signal parameters [28], but it is not a guaranteed result, especially when considering finer computations, for rotating objects. See for instance in [29] the complexity of possible waveforms and its consequences.
Binary systems are visible in radio astronomy when at least one member star is a pulsar, then used as a probe to identify the nature of the system. This explains why only eight such systems (only 5 confirmed by mass estimation, see [24]) have been found so far. This makes occurrence rate estimations very imprecise, see below.

**Merger**

The end of the inspiral phase is marked by the inadequacy of the 'pure' gravitation approximation. After the so-called Last Stable Orbit, the two bodies fall in and merge. For neutron stars, physical properties, deformation by tidal pull, equation of state and micro-physics like neutrino transport critically constraint the evolution.
Numerical simulations are the only way to follow the system through the merger. The dependency of the gravitational waveform on equation of state, specifically its effect on the frequency of the gravitational wave at last stable orbit, was exposed in [30] and [31]. The additional impact of spin was shown in [32] for the departure from the inspiral phase predictions till the post-merger black hole gravitational wave signal. In complement, for large masses, an intermediate 'hyper-massive' neutron star state was proposed by [33], of short lifetime but characteristic signature.
The case of black hole binaries is somewhat different, since there is no micro-physics to be included.

The merger phase of a binary neutron stars system is also a studied model for short GRB events [34]. An important issue being the possibility of jet-like structures. Observations are still analyzed for meaningful correlations ([35] and references therein), while models do not all validate this hypothesis [36].

The behaviour of the nascent compact object is discussed in Section 1.3.5.

### 1.3.3 Gravitational collapse

Disregarding black holes, the state equation of massive objects is dominated by the equilibrium between gravitational attraction and a pressure term. The latter is provided either by photon radiation, with thermonuclear fusion reactions as the energy source, or, for so-called dead stars, degeneracy pressure from electron gas when fusion is no more possible (Fe core) for a white dwarf, or strong force interactions for a neutron star. Knowing these mechanisms, extreme masses can be derived for degenerate stars [37]: stable white dwarfs are expected to have $M < M_{Chandrasekhar} = 1.46M_\odot$ and for neutron stars $M \lesssim 3M_\odot$, depending on the equation of state, still hypothetical. A star

with a core mass above the neutron star limit cannot balance the gravitational inward force and collapses into a black hole.
Transitions toward a neutron star or a black hole occur quickly, and large amounts of energy are expected to be emitted. They satisfy the conditions for gravitational waves sources. Another positive element for gravitational wave emission, hints for asphericity in supernova explosions were found [38] by interpreting spectroscopic data.

Supernovae (SNe) are very luminous objects, plus large sources of neutrinos. The mechanisms involved in the explosion concern nuclei and elementary particle physics, as reviewed in [39]. Categories of supernovae have been identified from optical spectra features. Type Ia SNe are thought to be white dwarfs with a companion star that provides accretion material till a final explosive thermonuclear reaction. The absence of a compact object reduces the interest of Type Ia supernovae as gravitational waves sources.
Type II supernovae (SNII) are large mass stars (presumably $M \gtrsim 8M_{\odot}$) that reach the end of the main sequence with too much mass to evolve into white dwarves. Details of the rapid evolution to neutron star or black hole, including envelop explosion, are still been refined by comparing observations and numerical simulations, see [40] for an up-to-date discussion.
The rest, type Ib and Ic SNe, should behave mostly as SNII, but parameters affecting optical spectra, like envelop mass and composition, may vary. They are commonly referred to as gravitational supernovae (SNg).

Numerical General Relativity is now a widely used tool for the study of the source dynamics / gravitational wave relation, see for instance [41] and references therein for a review. Simulations also provide plausible waveforms, that help define data analysis requirements, as discussed in chapter 2.
A common *caveat* for numerical simulations is the difficulty to actually obtain a supernova explosion. Most models end with a stalled explosion. Continuous improvements have included more accurate treatments of General Relativity effects, less constraints on spatial symmetry (from 1-dimensional models with spherical symmetry to full 3-dimensional codes) and more realistic physical processes, starting with hydrodynamics, then equation of state, the nuclear processes and finally neutrino transport.

With axi-symmetric stellar models, simulated in 2-dimensional numerical General Relativity, it was possible to identify the sequence of the core collapse, its timescales, and implications for gravitational wave signature. From [42], the iron core contraction starts slowly, initiated by electron capture and neutrino losses that become more efficient with increasing density, till neutrinos are trapped (about 200 ms after the process begins). A rapid contraction of the inner core then takes place, halted either by centrifugal forces or central densities exceeding the nuclear matter limit ($\lesssim$ 20 ms). The first strong gravitational wave is associated with the following core bounce, pushed by a pressure wave (a few milliseconds).

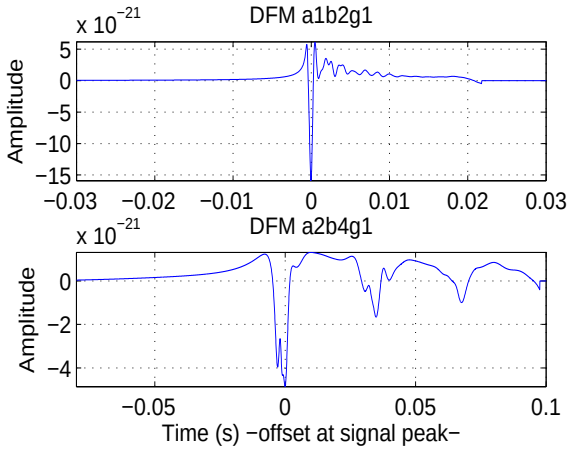


**Figure 1.6:** Two DFM waveforms from different families, 'regular' a1b2g1 (*Top*) and 'delayed' a2b4g1 (*Bottom*). Note the different time and amplitude scales.

The remaining inner core will oscillate while the outer layers will either be ejected in a supernova explosion, or fall back over longer durations, except where very high angular momentum brings about successive bounces of smaller amplitude.
Later work confirmed this scenario, while exploring the parameter space of stellar angular momentum and equation of state. Two catalogs of gravitational waves were produced, ZM [43] and DFM [44]. The three selected parameters (two concerning the rotation of the star, one its equation of state) were sufficient to distinguish three main families: firstly 'regular' collapse, with a short ($< 5$ ms) peak or double peak of large amplitude followed by small fluctuations, secondly 'delayed' collapse, with several long ($\gtrapprox 20$ ms) peaks of reduced amplitude, illustrated in figure 1.6, and finally 'fast' collapse, with little or no bounce but an short ($\approx 10$ ms) series of dampened oscillations for the proto neutron star.

Data analysis dedicated to core-collapse gravitational waves focus on short duration signals, with DFM-type or oscillatory waveforms as references.

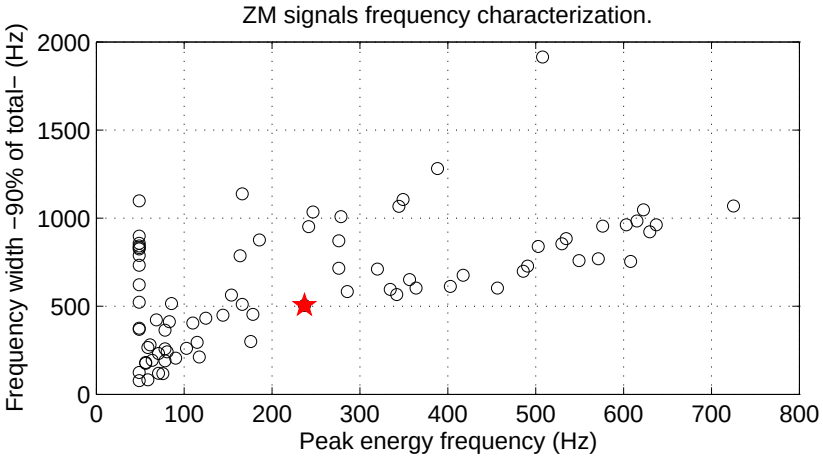


**Figure 1.7:** The ZM waveform family, frequency characterization. Bandwidth corresponds to the minimum to recover 90 % of the total energy, starting from the peak frequency.
The group of peak frequencies at 50Hz corresponds to a forced minimum: many waveforms have a large peak in the Fourier domain at very low frequencies, which will not be accessible to Virgo. The star indicates ZM a1b2g1, similar to DFM a1b2g1.

Work on 3-dimensional codes, for instance [45], suggest that non axi-symmetry dynamics could emerge, notably for fast-rotating stars, with apparition of bar-like motion during the collapse, an efficient gravitational wave generator geometry, producing essentially periodic signals, damped in time.

Analytic models for neutrino transport, like [46], suggest that the failure to produce a supernova explosion could come from under-estimating the energy input from the neutrino flash sometime during the bounce, as well as envelop convection. A simulation comparison to SN 1987 A, the closest supernova event in modern times, was proposed in [47], with convection at different scales and anisotropic neutrino fluxes.

With the growing complexity of simulations, additional supernova driving (and gravitational wave emission) mechanisms have been proposed. In [48], acoustic waves from the proto neutron star are proposed as an important energy source for late-time evolution and produce delayed (500 ms and more after the bounce) periodic gravitational waves. If verified as a generic and energetic component of SNg dynamics, this signature may call for novel analysis strategies.

Meanwhile, it is important to remark that there is a good agreement on the description and amplitude of the gravitational waves from the initial bounce. The order of magnitude in [49] for the amplitude of bounce gravitational wave has been updated from numerical Relativity studies [50] :

$$h \approx \frac{1}{8}\sqrt{\frac{15}{\pi}}\sin^2(\theta)\frac{{A_{20}}^{E2}}{3.09\times 10^{18} cm}\frac{10kpc}{d} \tag{1.57}$$

with ${A_{20}}^{E2}$ the quadrupole wave amplitude, of the order of 10 centimeters.
Predictions are that, with binary coalescence, SNg are the most efficient gravitational wave emitters. However there has been no detection yet, but improving upper limits for the Galactic event rate [51]. They are also possible sources for long GRB events, as explored in [52].

Probably less frequent, but more energetic than a regular SNII, hypernovae. These supermassive stars have a very rapid evolution (see [53]) that ends up in a collapse of very high energy. Complex behaviour could occur, see [54] and [55] for instance, favorable to gravitational wave emission. These are still secondary sources owing notably on population uncertainties.

### 1.3.4 Event rates

Progenitor populations are estimated from astronomical object catalogs. This represents more than a hundred objects for SNII, less than ten for neutron star binaries and an empty set for stellar black hole binaries. In that case, models of stellar population [56] are used to constrain somehow the figures. The final interpolation to observable event rate must take into account the distribution of stars in the Galaxy and its neighbourhood.

| Source type | NS - NS | NS - BH | BH - BH | SNII |
|---|---|---|---|---|
| Galact. rate ($y^{-1}$) | $\sim 2\,10^{-5}$ | $< 10^{-5}$ | $< 10^{-5}$ | $10^{-2}$ |
| Detection rate ($y^{-1}$)(a) | $5\,10^{-3}$ to 0.3 | $< 10^{-1}$ | $< 10^{-1}$ | $10^{-2}$ |
| Max. detect. dist. (b) | 20 Mpc | 42 Mpc | 100 Mpc | 10 kpc |
| Frequency (Hz) | $10^3$ (LSO)(c) | $10^2$ (LSO) | 320 (LSO)(d) | $200 - 10^3$ |

**Table 1.1:** Estimations by source type. (a) For present sensitivities. (b) For 1.4 $M_\odot$ NS and 10 $M_\odot BH$. (c) Last Stable Orbit. (d) For two 10 $M_\odot$ objects. Values from [57], compatible with recent work, see [58] and [59].

### 1.3.5 Excited compact objects

Many other circumstances for gravitational wave emission have been proposed, in the limits of source characteristics highlighted in Section 1.3.1. They present either a low-efficiency conversion to gravitational wave, and therefore weak signal amplitude, very low -if not unknown- occurrence rate, or still poorly constrained mechanisms.
For instance accretion disks and matter jet formation could be low efficiency sources of gravitational waves possibly accessible for close objects. The probable discovery of Galactic stellar-mass black holes [60] make these mechanisms very attractive.
Low amplitude signals, from weak or very distant sources, could constitute a gravitational wave stochastic background, that may be interpreted in relation with other cosmological observations.

An illustrative list of candidates is given hereafter.

#### Non-symmetrical compact objects

A rotating neutron star, with moment of inertia $I$ with respect to the rotation axis, if departing from a symmetric shape by a characteristic value $\epsilon$, related to its quadrupole moment, see [61], would emit gravitational waves at the rotation frequency $f_{rot}$ and $2 \times f_{rot}$, with an amplitude of the order of :

$$h = 4.21 \times 10^{-23} \left[\frac{f_{rot}}{kHz}\right]^2 \left[\frac{10kpc}{d}\right] \left[\frac{I}{I_{NS1.4M_\odot}}\right] \left[\frac{\epsilon}{10^{-6}}\right] \tag{1.58}$$

for $I_{NS1.4M_\odot} = 10^{38}\ kg\ m^2$ a typical value for the principal moment of inertia of a neutron star.
These signals should be accessible from any close neutron star, which is not the case for the very directed pulsar emission, although extraction from the data of existing instruments would require very long integration times (several years). Thus it has not been possible yet to detect any gravitational counterpart for several known pulsars [62]. The observation of such a signal would allow refinements of neutron stars composition and structure models.

Finally short duration crust quakes [63] on compact objects could contribute gravitational wave signals as well. It may even be possible to see the counterpart of pulsar period glitches, possibly related to angular momentum transfer [64] in a core / crust model neutron star.

**Relaxation of proper modes**

Instead of static symmetry defects, a young neutron star is likely to have an evolving shape, owing to excess energy remaining from its formation. Using a simple liquid drop model, it can be shown that some deformations are privileged, resulting in oscillations with a noticeable life time [65]. These so-called Quasi-Normal Modes would produce gravitational waves and dissipate the excess energy till the neutron star reaches a quiescent state.
This process should also apply to newly-formed black holes, for which the only proposed energy dissipation channel is gravitational wave emission. These damped oscillations have been described analytically [66] with a characteristic frequency $f_c$ and a quality factor $Q$ :

$$\begin{aligned} h(t) &\propto e^{-\frac{\pi f_c}{Q}(t-t_0)} \sin(2\pi f_c(t-t_0)+\phi_0) \\ f_c &\simeq 32\left(\frac{M_\odot}{M}\right)[1-\alpha(1-a)^\beta] \text{ kHz} \\ Q &\simeq 2(1-a)^\gamma \end{aligned} \tag{1.59}$$

where $t_0$ is the arrival time at the detector, $\phi_0$ the initial phase, and $a \in [0,1[$ a (non-dimensional) parameter for initial angular momentum. The Greek letters represent numerical constants : $\alpha = 63/100$, $\beta = 3/10$ and $\gamma = -9/20$.
Numerical Relativity agrees with these predictions, for instance in [67], which is an encouraging indication of the maturity of black hole treatment in simulations.

## 1.4 Physics from gravitational wave astronomy

From the test of theories of gravitation to cosmology and particle physics, gravitational wave astronomy could uniquely contribute in many active fields.
The required proximity of core collapse sources for a gravitational wave observation using available instruments should also allow measurement of the neutrino flux, characteristic of the onset of envelop expansion, plus the electromagnetic evolution, already well understood. Besides, the plausible Gamma Ray Burst connection would relate a gravitational wave signal from a coalescing binary to optical data.

### 1.4.1 Theory of gravitation

As sketched above, gravitational wave sources involve relativistic objects. This implies that the information brought to us by this new messenger could provide new constraints on strong field gravity [5].
Where General Relativity proposes only two polarizations for a gravitational wave, some alternative theories suggest more. While a single-instrument observation cannot be used to extract this information, a network of instruments whose spatial orientations are complementary could be used to recover the polarization [68]. Considering the coupling $\ddot{x} = -R_{0i0j}x^j$ of gravitational wave with a pair of test-masses separated by $x^i$, the six polarization coefficients (free parameters in $R_{0i0j}$) could be recovered from a network of six gravitational wave antennas if the source direction is obtained externally, from optical or high energy photons data. This could discriminate, see for instance [69], between General Relativity and the Brans-Dicke generalization of the theory.

### 1.4.2 Cosmology and 'standard candles'

The greatest interest of gravitational waves from binary systems is the source information extraction it allows, by inversion of the detected waveform shape from first General Relativity principles. When an observation network is available and large numbers of coalescence events have validated the waveform predictions, signal amplitude could provide source distance indications, possibly up to the Giga-parsec horizon expected for second generation instruments. Before that, a small number of events occurring within 100 Mpc may be sufficient, even without highly accurate waveform interpretation, to estimate the Hubble constant to a few percents, as suggested in [70].

This would complement results from the Ia supernovae 'standard candle', see for instance [71]. These observations may be extended to other cosmological parameters studies, as pursued in deep optical SNIa surveys like [72], to estimate the cosmological constant and the dark matter proportion.

### 1.4.3 Particle physics

String theory spawned scenarios for the cosmological evolution of the Universe, among which the existence of cosmic strings, that could produce under certain conditions characteristic gravitational waves. As discussed for instance in [73], these could be detected by ground instruments with the current sensitivity or the next generation.
Once a large catalog of SNg-type gravitational wave observations has been compiled, with complementary optical and neutrino counterparts, it will also be possible to extract constraints on the neutrino mass [74], using the delay in arrival time. Gravitational waves could prove more useful than the electromagnetic flare, for they should be emitted for the most part at the moment of greatest core evolution, close to the deconfinement of the neutrino flux.
The same strategy could work for graviton mass limits, from core-collapses, between gravitational wave and optical observations. The error on the graviton to light velocity ratio would come predominantly from the emission process models, necessary to fix the emission delay. Alternatively, it is predicted that the velocity of a massive graviton would be dependent on wave frequency. As the gravitational wave from an inspiraling binary sweeps a large frequency band, a phase-delay should accumulate, hopefully identified by waveform matching. See [75] for a discussion on these possibilities, which should be at least at the level of the upper limit $\lambda_g = \frac{h}{m_g c} > 2.8 \times 10^{12}$ km for a Yukawa-type $V(r) = \frac{GM}{r} e^{-r/\lambda_g}$ gravitational potential, as obtained in [76] from solar-system mechanics.

### 1.4.4 Black hole observation

Black holes are reliable sources of gravitational waves, which would provide direct information on the properties of the object. The eventual observation of a signal will provide a direct proof of the existence of these objects, as described by General Relativity. Besides, black hole astronomy would open to stellar mass black holes, in complement to today's indirect results, from the interpretation of stellar orbits [77] and accretion disk observations [78]. Galactic mass distribution and stellar evolution models would gain from these results.

## 1.5 Conclusions

### 1.5.1 Gravitational wave astrophysics

The Virgo project, started in 1989, now reaches potentially interesting sensitivity levels, comparable with that of the other instruments of close design.
The convergence of the analysis of these instruments will allow a better simultaneous sky coverage, via coincident and coherent data processing. The aim will be improved detectability and source direction reconstruction.
Upgrades scheduled for the coming years should give a factor 10 in observation horizon, hence a 1000 volume increase, and improved detection odds for the sources mentioned above.
Other source types, at very low frequency ($10^{-4}$ Hz to 1 Hz), will eventually become accessible when the space interferometer LISA [79] starts operating.
This expected multiplication of gravitational wave observations will facilitate multi-messenger studies and add to the understanding of high energy phenomena in the universe.

### 1.5.2 Scope of this work

In the context of Virgo final commissioning stage, two issues summarize the work presented hereafter. The first one is the development of novel detection algorithms for impulsive signals, robust with respect to received energy and waveform. The second concerns the possibility of removing well-modeled noises in stored data.
The final part deals with the transition from simulation to real data for the developed tools, the

information that could be derived concerning the workings of the instrument and strategies to work around some current limitations.

# Bibliography


[1] E. Klein and M. Spiro (editors) "Le temps et sa flèche", Colloque SFP (Flammarion, France, 1996).

[2] P. Binétruy *et al*,*Relating incomplete data and incomplete theory*, *Phys. Rev.* D **70**, 095006 (2004).

[3] G. Esposito-Farez, Graduate introductory course on General Relativity, (I.A.P., 2005).

[4] C.W. Misner *et al*, "Gravitation" (W.H. Freeman & Company, 1973).

[5] C.M. Will, "Theory and experiment in gravitational physics" (Cambridge University Press, UK, 1993).

[6] S.M. Carroll, *Lectures notes on General Relativity* <gr-qc/9712019> (1997).

[7] R. Hakim, "Gravitation relativiste" (CNRS-Editions, France, 2001).

[8] S. Weinberg, "Gravitation and Cosmology : Principles and Applications of the General Theory of Relativity" (Wiley, New York, 1972).

[9] S. Hawking, "A brief history of time" (Bantam Press, UK, 1988).

[10] P.C. Peters & J. Mathews, *Gravitational radiation from point masses in a keplerian orbit*, *Phys. Rev.* **131**, 435 (1963).

[11] D. Garfinkle, *Gauge invariance and the detection of gravitational waves*, Am. J. Phys. **74**, 3 (2006).

[12] V. Fafone, *Resonant-mass detectors: status and perspectives*, *Class. Quant. Grav.* **21**, 5 (S377).2004

[13] P. Astone *et al*, *Methods and results of the IGEC search for burst gravitational waves in the years 1997 2000*, *Phys. Rev.* D **68**, 2 (022001).2003

[14] <http://www.ligo.caltech.edu>

[15] N. Arnaud *et al*, *Coincidence and coherent data analysis methods for gravitational wave bursts in a network of interferometric detectors*, *Phys. Rev.* D **68**, 102001 (2003).

[16] <http://www.virgo.infn.it>

[17] P.R. Saulson, "Fundamentals of interferometric gravitational wave detectors" (World Scientific, Singapore, 1994).

[18] N. Arnaud *et al*, *The Global Control of the Virgo experiment*, *Nucl. Instrum. Methods* A **550**, 467-489 (2005).

[19] S. Kreckelbergh, "Contrôle longitudinal et caractérisation optique du détecteur Virgo" (LAL 05-102, PhD thesis, 2005).

[20] The Virgo Collaboration (F. Acernese et al.), *Measurement of the seismic attenuation performance of the Virgo super-attenuator*, Astroparticle Physics **2**, 557 (2004).

[21] P.R. Saulson, *Thermal noise in mechanical experiments*, *Phys. Rev.* D **42**, 2437 (1990).

[22] M. Punturo, *The Virgo sensitivity curve*, Virgo Note VIR-NOT-PER-1390-51 (2004).

[23] N. Arnaud *et al*, *Comparison of filters for detecting gravitational wave bursts in interferometric detectors*, *Phys. Rev.* D **67**, 062004 (2003).

[24] D.R. Lorimer ,*Binary and millisecond pulsars*, Living Rev. Relativity **8**, 7 (2005). [Online article]: cited [January 2006], <http://www.livingreviews.org/lrr-2005-7>.

[25] L. Blanchet, T. Damour, G. Esposito-Farese *et al*, *Gravitational radiation from inspiralling compact binaries completed at the third Post-Newtonian order*, *Phys. Rev. Lett.* **93**, 091101 (2004).

[26] D. Blair in "The detection of gravitational waves", ed. D. Blair (Cambridge University Press, UK, 1991).

[27] P. Hello, in "Proceedings of 2nd GWDAW", ed. M. Davier & P. Hello Frontieres, 1998.

[28] C. Cutler & E.E. Flanagan, *Gravitational waves from merging compact binaries: How accurately can one extract the binary's parameters from the inspiral waveform?*, *Phys. Rev.* D **49**, 2658 (1994).

[29] P. GrandClément & V. Kalogera, *Searching for gravitational waves from the inspiral of precessing binary systems: Problems with current waveforms*, *Phys. Rev.* D **67**, 042003 (2003).

[30] M. Bejger *et al*, *Impact of the nuclear equation of state on the last orbits of binary neutron stars*, A.A. **431**, 297 (2005).

[31] F. Limousin, D. Gondek-Rosin'ska & E. Gourgoulhon, *Last orbits of binary strange quark stars*, *Phys. Rev.* D **71**, 064012 (2005).

[32] M. Ruffert & H.T. Janka, *Coalescing neutron stars - A step towards physical models III. Improved numerics and different neutron star masses and spins*, A.A. **380**, 544 (2001).

[33] M. Shibata *et al*, *Merger of binary neutron stars with realistic equations of state in full relativity*, *Phys. Rev.* D **71**, 084021 (2005).

[34] T. Piran in "Proceedings 16th international conference on General relativity and Gravitation", ed. N.T. Bishop & S.D. Maharaj (World Scientific, Singapore, 2002).

[35] N.R. Tanvir *et al*, *An origin in the local Universe for some short gamma-ray bursts*, Nature **438**, 991 (2005).

[36] S. Rosswog, *Mergers of neutron star-black hole binaries with small mass ratios: nucleosynthesis, gamma-ray bursts, and electromagnetic transients*, Ap.J. **634**, 1202 (2005).

[37] M.S. Longair, "High energy astrophysics" vol. 2 (Cambridge University Press, 2000).

[38] P.A. Mazzali *et al*, *An asymmetric energetic type Ic supernova viewed off-axis, and a link to gamma ray bursts*, Science **308**, 1284 (2005).

[39] H.A. Bethe, *Supernova mechanisms*, *Rev. Mod. Phys.* **62**, 801 (1990).

[40] S. Woosley and T. Janka, *The physics of core-collapse supernovae*, Nature Physics **1**, 147 (2005).

[41] C.L. Fryer & K.C.B. New, *Gravitational waves from gravitational collapse*, Living Rev. Relativity **6**, 2 (2003). [Online article]: cited [January 2006], <http://www.livingreviews.org/lrr-2003-2>.

[42] R. Mönchmeyer *et al*, *Gravitational waves from the collapse of rotating stellar cores*, A.A. **246**, 417 (1991).

[43] Zwerger & E. Müller, *Dynamics and gravitational wave signature of axisymmetric rotational core collapse*, A.A. **320**, 209 (1997).

[44] H. Dimmelmeier, J.A. Font & E. Müller, *Relativistic simulations of rotational core collapse II. Collapse dynamics and gravitational radiation*, A.A. **393**, 523 (2002).

[45] M. Shibata & Y. Sekiguchi, *Three-dimensional simulations of stellar core collapse in full general relativity: Nonaxisymmetric dynamical instabilities*, *Phys. Rev.* D **71**, 024014 (2005).

[46] H.T. Janka, *Conditions for shock revival by neutrino heating in core-collapse supernovae*, A.A. **368**, 527 (2001).

[47] K. Kifonidis *et al*, *Non-spherical core collapse supernovae. II. The late-time evolution of globally anisotropic neutrino-driven explosions and their implications for SN 1987 A*, submitted. Online text: astro-ph/0511369.

[48] A. Burrows *et al*, *A new mechanism for core-collapse supernova explosions*, submitted. Online text: astro-ph/0510687.

[49] K.S. Thorne in "300 Years of Gravitation", ed. S.W. Hawking & W. Israel (Cambridge University Press, 1986).

[50] E. Müller *et al*, *Toward gravitational wave signals from realistic core-collapse supernova models*, Ap.J. **603**, 221 (2004).

[51] M. Ando *et al*, *Observation results by the TAMA300 detector on gravitational wave bursts from stellar-core collapse*, *Phys. Rev.* D **71**, 082002 (2005).

[52] Z. Bosnjak *et al*, *Gamma-ray bursts associated with supernovae: a systematic analysis of BATSE data*, A.A. **447**, 121 (2006).

[53] I. Baraffe, A. Heger, S.E. Woosley, *On the Stability of Very Massive Primordial Stars*, Ap.J. **550**, 890 (2001).

[54] T.W. Baumgarte, S.L. Shapiro, *Evolution of Rotating Super-massive Stars to the Onset of Collapse*, Ap.J. **526**, 941 (1999).

[55] M.H.P.M. van Putten, *Gravitational Wave Frequencies and Energies in Hypernovae*, Ap.J. **583**, 374 (2003).

[56] R. Voss & T.M. Tauris, *Galactic distribution of merging neutron stars and black holes - prospects for short $\gamma$-ray burst progenitors and LIGO/Virgo*, M.N.R.A.S. **342**, 1169 (2003).

[57] K.S. Thorne in *Proceedings Snowmass 94*, ed. E.W. Kob & R. Peccei (World Scientific, Singapore, 1995).

[58] E. Cappellaro *et al*, *A new determination of supernova rates and a comparison with indicators for galactic star formation*, A.A. **351**, 459 (1999).

[59] V. Kalogera *et al*, *The cosmic coalescence rates for double neutron star binaries*, Ap.J. **601**, L179 (2004).

[60] I.F. Mirabel, L.F. Rodriguez, *Microquasars in our Galaxy*, Nature **362**, 673 (1998).

[61] S. Bonazzola & E. Gourgoulhon, *Gravitational waves from pulsars: emission by the magnetic field induced distortion*, A.A. **312**, 675 (1996).

[62] A. Abbott *et al*, (the LIGO collaboration), *Limits on gravitational-wave emission from selected pulsars using LIGO data*, *Phys. Rev. Lett.* **94**, 181103 (2005).

[63] N. Andersson, D.I. Jones & K.D. Kokkotas, *Strange stars as persistent sources of gravitational waves*, Mon.Not.Roy.Astron.Soc. **337**, 1224 (2002).

[64] B. Link, R.I. Epstein & J.M. Lattimer, *Pulsar constraints on neutron star structure and equation of state*, *Phys. Rev. Lett.* **83**, 17 (3362).1999

[65] K.D. Kokkotas & B.G. Schmidt, *Quasi-normal modes of stars and black holes*, Living Rev. Relativity **2**, (1999). [Online article]: cited [January 2006], <http://www.livingreviews.org/lrr-1999-2>.

[66] F. Echeverria, *Gravitational-wave measurements of the mass and angular momentum of a black hole*, *Phys. Rev.* D **40**, 3194 (3203).1989

[67] J.G. Baker *et al*, *Binary black hole merger dynamics and waveforms*, submitted. Online version: gr-qc/0602026.

[68] C.M. Will, *Update to 'The confrontation between General Relativity and experiment'*, submitted to *Living Rev. Relativity*, gr-qc 0510072.

[69] M. Maggiore & A. Nicolis, *Detection strategies for scalar gravitational waves with interferometers and resonant spheres*, *Phys. Rev.* D **62**, 024004 (2000).

[70] B.F. Schutz, *Determining the Hubble constant from gravitational wave observations*, Nature **323**, 310 (1986).

[71] M. Stritzinger & B. Leibundgut, *Lower limits on the Hubble constant from models of type Ia supernovae*, A.A. **431**, 423 (2005).

[72] P. Astier *et al*(The SNLS collaboration), *The Supernova Legacy Survey: Measurement of* $\Omega_M$, $\Omega_\Lambda$ *and w from the first year data*, To be published in A.A.

[73] T. Damour & A. Vilenkin, *Gravitational radiation from cosmic (super)strings: Bursts, stochastic background, and observational windows*, *Phys. Rev.* D **71**, 6 (2005).

[74] N. Arnaud *et al*, *Gravity wave and neutrino bursts from stellar collapse: a sensitive test of neutrino masses*, *Phys. Rev.* D **65**, 033010 (2002).

[75] C.M. Will, *Bounding the mass of the graviton using gravitational-wave observations of inspiraling compact binaries*, *Phys. Rev.* D **57**, 2061 (1998).

[76] C. Tamadge *et al*, *Model-independent constraints on possible modifications of Newtonian gravity*, *Phys. Rev. Lett.* **61**, 1159 (1988).

[77] R. Schodel *et al*, *A star in a 15.2-year orbit around the supermassive black hole at the centre of the Milky Way*, Nature **419**, 6908 (694).2002

[78] M. Cadolle Bel, *The broad-band spectrum of Cygnus X-1 measured by INTEGRAL*, A.A. **446**, 591 (2006).

[79] <http://www.jpl.nasa.gov>

# Chapter 2

# Time-frequency data representations

## Contents



## 2.1 Introduction

This work is motivated by the search for 'burst' events in gravitational wave interferometer data. Typical duration is less than 0.1 second, making for potentially large frequency-bandwidth signals. Detection is particularly challenging due to the expected variety of astrophysical waveforms and the issue of discriminating them from instrumental noise, dominant in data from ground interferometers. There is a consensus that robust methods are required, that achieve reasonable detection performances over a wide range of signals.
Many transforms exist, but no performance hierarchy has yet been established, though work on that topic has began in earnest, notably in a joint LIGO-Virgo working group, in preparation of multi-instrument analysis, see [1] and [2]. The simulation results presented here were for the most part obtained in this collaborative work.

### 2.1.1 Wiener filtering

The generic form for the linear filtering of a data stream $h$ with an arbitrary kernel function $\phi$ is the correlation equation :

$$h * \phi(t) = \int_{-\infty}^{\infty} h(\tau)\phi(t-\tau)\, d\tau \tag{2.1}$$

This time-domain integral is conveniently computed in the Fourier domain, since $\mathcal{F}[f * g(t)](\nu) = \mathcal{F}[f(t)] \times \mathcal{F}[g(t)](\nu)$, for $\mathcal{F}$ the Fourier transform (FT). Hereafter the Fourier transform of a series $h$ will be noted $\hat{h} = \mathcal{F}(h)$.
Wiener worked on the problem of recovering a known signal $u$ mixed with additional Gaussian noise $n$, using a linear filter. To quantify the recovery, he considered the minimum least square error on the estimated signal $\tilde{u}$, given by :

$$\epsilon = \int_{-\infty}^{\infty} |\tilde{u}(t) - u(t)|^2\, dt \tag{2.2}$$

He showed, see [3] for details, that the best kernel $\phi$ was the actual sought waveform, normalized by the spectral power density of the noise $P_n(f)$ :

$$\hat{\phi}(f) = \frac{\hat{u}(f)}{S_n(f)} \tag{2.3}$$

This constitutes the Wiener filter. The optimal visibility of the waveform in the noise, or signal to noise ratio (SNR) $\rho$ is then given by :

$$\rho^2 = \int_{-\infty}^{\infty} \frac{|\hat{u}(f)|^2}{S_n(f)}\, df \tag{2.4}$$

The SNR will appear several times here, as it is a convenient way to quantify the visibility of a waveform while taking noise into account.
While the output of the filter in the presence of the signal is given by the SNR, it is necessary to estimate the output for noise only. A linear filter preserves the statistical distribution of the data. For a time series with zero mean and variance $\sigma$, the probability distribution $f$ of the output value is :

$$f(x) = \frac{1}{\sigma\sqrt{2\pi}} e^{-x^2/2\sigma^2} \tag{2.5}$$

A result valid also for the Wiener filter, and useful when adjusting a detection decision threshold: $f$ gives the probability of a false detection, or false alarm, for a given SNR threshold.

### 2.1.2 Match filtering

The result from Wiener is the origin of the match-filtering scheme, or correlation between data and a fixed template, which is either the exact sought waveform, an approximation of the signal, or a more simple shape likely to be present in a signal. For a time series h, match with a template s is defined as :

$$\begin{aligned} c(t) &= \frac{< s(t), h(t) >}{||s||} \\ with \qquad < s(t), h(t) > &= \int_{-\infty}^{\infty} \frac{\hat{s}(f)\hat{h}^*(f)}{P_h(f)}\, df \\ and \qquad ||s|| &= max_t < s(t), s(t) >^{1/2} \end{aligned} \tag{2.6}$$

where $P_h(f)$ is the power spectral density of the noise. The norm is the maximum value of the match, over time.
When an analytic description of the searched signal exists, as mentioned in Chapter 1 for binary inspiral or black hole relaxation, looking for this waveform seems to be the best strategy. As analytic formulas are parametrized by one or several physical quantities, there is an infinity of possible waveforms.

**Template selection**

Any actual search must rely on a limited number of templates. It is therefore essential to define a set of complementary templates to maximize coupling with signal. This can be quantified by the mismatch between template and signal given by the ambiguity function $\Gamma$ between templates $\phi$ and $\psi$ :

$$\Gamma(\phi, \psi) = max_t < \phi(t), \psi(t) > \tag{2.7}$$

using the conventions of equation 2.6 and normalized templates ($||\phi|| = ||\psi|| = 1$). This formula estimates the overlap between two templates, defined by a set of parameters, and satisfies the criteria for a scalar product in the parameter space of the templates.
For practical purposes, the ambiguity function can be approximated, within the hypothesis of close narrow-band templates previously normalized, as :

$$\Gamma(\phi, \psi) = \int_{-\infty}^{\infty} \phi(t)\psi(t)\, dt \tag{2.8}$$

Setting a minimum match (MM) in the form $\Gamma > 1 - MM$, a tiling of the parameter space with a close to minimum template number can be proposed.
When waveforms depend on two parameters, this set can be provided using the method of [4]. Another tiling scheme for black hole ring-down is discussed in [5], with its implementation and performances.

**The Peak Correlator filter**

Peaks are simple features to look for in data, as they are frequent in physically motivated waveforms. The Gaussian peak is a compact waveform, both in time and frequency, very easy to manipulate analytically. Using the template selection principle outlined above, a bank of Gaussian waveforms can be built and applied, as in the burst search method Peak Correlator [6].
For a Gaussian kernel, the simplified ambiguity function is :

$$\Gamma_{Gaussian}(\sigma_1, \sigma_2) = \sqrt{\frac{2(\sigma_1 \times \sigma_2)}{\sigma_1^2 + \sigma_2^2}} \tag{2.9}$$

which for a fixed minimum match and a starting template $\sigma_{min}$ gives the tiling relation :

$$\sigma_k = (1 + 2\sqrt{1 - MM})^{k-1}\sigma_{min} \qquad \forall k \in \mathbb{N}^* \tag{2.10}$$

The normalization guarantees that the output value is scaled to the noise spectrum and provides a signal to noise ratio (SNR), and suppresses static or slow-varying coloration of the data.

### 2.1.3 Filter performance estimators

Having quantified the visibility of a waveform with the signal to noise ratio, it remains to establish easy to interpret representations suitable for filter comparison.
Detection is classically presented as a decision problem, between absence or presence of an interesting signal in the data under scrutiny. As sketched above, the definition of an 'interesting' signal is at the heart of the design of the detection method. Significance can then be established by comparison of output values with one or several thresholds.
Coined terms for a wrongly tagged noise fluctuation and unseen signal are false alarm and false dismissal. For a single-output method and Gaussian noise, false alarm rate is obtained from equation 2.5. Using a single-threshold decision rule for a chosen false alarm rate over a given observation time minimizes the false dismissal rate. This is the 'Neyman-Pearson observer' situation, as discussed in [7].
Judging the ability to discriminate signal from noise, one does not need to know the applied threshold. The detection efficiency (number of recovered signals normalized to the total number of signals present) for any false alarm rate summarizes performances independently of method details. These are the Receiver Operating Characteristics (ROC) curves, first developed for radar detection, and now commonly used in signal analysis. See [8] for such results on the PC filter.
Following [7], in the case of a completely known waveform, Gaussian noise and a linear filter, the

false alarm probability $F$ and detection probability $D$ depend on the SNR $\mu$ of the signal and the selected threshold $\phi$ by :

$$F(\phi) = Q(\frac{\phi}{\mu}) \tag{2.11}$$

$$D(\phi) = Q(\frac{\phi}{\mu} - \mu) \tag{2.12}$$

where $Q(x) = \frac{1}{\sqrt{2\pi}} \int_x^\infty e^{-z^2/2}\, dz$.
ROC curves will be the main tool here for method comparison.
Another convenient indication of filter performances is the signal amplitude requested to obtain a fixed efficiency. From results on discrete signal amplitudes, it is possible to adjust a sigmoid curve model to the ($F$,$D$) points.

## 2.2 Generalities on time-frequency transforms

It has been recognized that the time-frequency (TF) space could provide a valuable representation of time series, where signal isolation from noise could be achieved without waveform-type discrimination (see for instance [9]).
Time-frequency does not designate a specific group of methods, but loosely includes any transform that develop a time series into a time-frequency (TF) plane, where each coefficient gives an instantaneous energy or amplitude spectral density (localized in frequency). This transposition is restricted by the Heisenberg-Gabor incertitude $\Delta t \times \Delta f \geq \frac{1}{4\pi}$, with $\Delta t$ the signal duration and $\Delta f$ its bandwidth.
Before getting to the methods developed in this study, the two examples below provide background material on time-frequency analysis.

### 2.2.1 Gabor transform

A classical example is the Gabor transform, a spectrogram where data is windowed by a Gaussian window, to increase time resolution. For the Gabor transform, using the generic formula 2.1, the transformation kernel is :

$$\phi_\sigma(t, \mu) = \frac{1}{\sigma\sqrt{2\pi}} e^{-t^2/2\sigma^2} e^{i\mu t} \tag{2.13}$$

The normalization factor guarantees an equal energy when the time width, given by $\sigma$, changes while the complex exponential selects the central sampled frequency $\mu$. Its Fourier transform

$$\Phi_\sigma(\nu) = e^{-2(\pi(\nu-\mu)\sigma)^2} \tag{2.14}$$

illustrates the resolution limit: bandwidth is set by the product $\sigma \times \mu$, a systematic coupling for time-frequency transforms.
Practically, the Gabor transform is obtained in the time domain by the formula :

$$G_\sigma(h, t, \mu) = \mathcal{F}^{-1}\left[\int_{-\infty}^{\infty} \hat{h}(\nu) e^{-2(\pi(\nu-\mu)\sigma)^2}\, d\nu\right](t) \tag{2.15}$$

Provided an accurate estimation of the Fourier transform for discrete duration-limited data segments, the computation requested by equation 2.15 is less than for time-domain correlation, since all time indexes are treated simultaneously. In the original Gabor transform, the width parameter $\sigma$ is fixed, which simplifies further this computation.

### 2.2.2 Wavelet transform

The wavelet transform (see [11] for a throughout introduction) illustrates the benefits of modifying the width of the kernel function. It relies on the decomposition of the signal by successive convolutions with waveforms derived by time dilatations of a 'mother' waveform (or wavelet) $\phi$, following :

$$W_h(t, s) = \int_{-\infty}^{\infty} h(u) \frac{1}{s} \phi^*(\frac{u-t}{s})\, du \tag{2.16}$$

and separation of a residual of the decomposition, to be the input of the following step. The kernel function $\phi$ must satisfy some conditions, mostly to guarantee the full decomposition of the data, and the invertibility of the transform. Namely, it must have a null average and satisfy the so-called admissibility condition :

$$\int_{-\infty}^{\infty} \frac{|\hat{\phi}(\omega)|^2}{\omega} d\omega < \infty \tag{2.17}$$

Plus its norm must be normalized to 1 and its shape be centered at time $t = 0$. In the original 'dyadic wavelet' algorithm for instance, the dilatation coefficient is a power of two, with each decomposition level called a scale. Besides, the decomposition was not computed for each time bin but sparsely, with the same power of two step used to establish the wavelet.
To obtain frequency localization with wavelets, analytic kernels (with $\hat{\phi(\omega)} = 0$ for $\omega < 0$) were introduced. They extract information over a characteristic duration $\sigma_t$, defined as :

$$\sigma_t{}^2 = \int_{-\infty}^{\infty} t^2 |\phi(t)|^2 \, dt \tag{2.18}$$

and frequency bandwidth $\sigma_\omega$ around a central frequency $\nu$ according to :

$$\nu = \int_{0}^{\infty} \omega |\hat{\phi}(\omega)|^2 \, d\omega \tag{2.19}$$

$$\sigma_\omega{}^2 = \frac{1}{2\pi} \int_{0}^{\infty} \omega_\nu{}^2 |\hat{\phi}(\omega)|^2 \, d\omega \tag{2.20}$$

### 2.2.3 Data segmentation scheme

As a technical solution to the problem of edge effects in the Fourier transform of a data segment of limited size, the Welch overlapping scheme [12] is applied whenever the Fourier transform appears. Data is treated in chunks of size N, with an overlap of N/2. Each chunk is windowed by the Hann function $w(i) = \frac{1}{2}(1 - \cos(\frac{2\pi i}{N-1}))$, and the two outputs of the transform for the same data bin, from successive chunks, are summed to provide the final coefficient.
This is possible here since all methods have a linear behaviour and phase information, when available, is not exploited.

### 2.2.4 Time-frequency events

The elementary output of a time-frequency transform is a coefficient indexed both in time and frequency. Analysis relies on maps of coefficients, or TF 'pixels', over a selected range of time and frequencies.
Once in the time-frequency plane, some basic image processing is required to extract meaningful events, based on a definition for the significance of the TF coefficients and the hypothesis that adjacent coefficients refer to close, if not identical, signal components.
Similar techniques are applied for the different filters: suppression of individual TF coefficients below a set threshold and clustering of adjacent coefficients. The output events, or clusters, are composed of a list of pixels of known position and value. Quantities like event time and frequency can then be extracted, either from the position of the maximum value (the peak energy) of the list, or as a composite (average or barycenter) of all elements. In addition are kept the length of the pixel list for each event, that defines a size for the event, and the sum of all coefficients values, the total energy of the event ($E = \sum_{i \in event} pixel_i$).

## 2.3 Selected transforms

The logical relation between the methods tested here starts with a wavelet transform, already briefly introduced. The following changes aimed at improving on the shortcomings of the previous approach, without reproducing an algorithm already available.
Three methods are compared, representing major families: wavelets, short-time windowed Fourier transforms and match filtering.

### 2.3.1 The 'à trous' wavelet transform

Wavelet analysis can be carried either in the time domain or Fourier domain. For the 'à trous' algorithm (AT), presented in [13], the main particularity is that the original sampling rate is maintained through all the scales.
The decomposition separates the data $h$ in trace $t$ and residual $r$, such as $h = t + r$. the trace is computed with the correlation formula 2.1, recursively from the residual of the previous scale. In the time domain, for a discrete time series and a wavelet $w$ of size $2N+1$, the dyadic decomposition, initialized with $h_0 = h$, gives at scale $s$ :

$$t_s(k) = \sum_{i=-N}^{N} h_s(k + i * 2^s) \times w(i) \quad (2.21)$$

$$r_s(k) = h_s(k) - t_s(k) \quad (2.22)$$

$$h_{s+1}(k) = r_s(k) \quad (2.23)$$

Note that due to the dyadic scaling of the decomposition, the frequency sampling is far from regular, as shown in figure 2.1. There is an over-representation of the low frequency region, while high frequencies are grouped in a few scales.

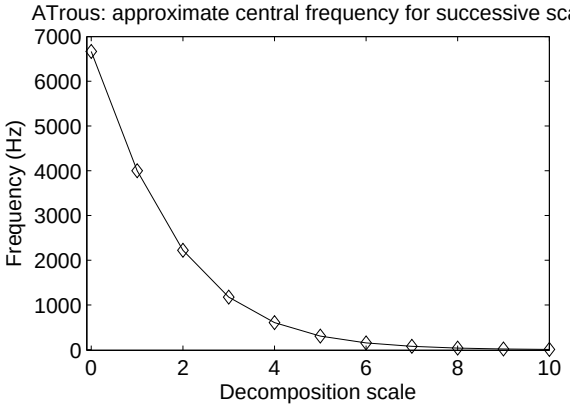


**Figure 2.1:** Approximate central frequency of the selected wavelet for increasing scale factors. The formula $f = f_{sampling}/(1 + 2 \times 2^{scale})$ was used.

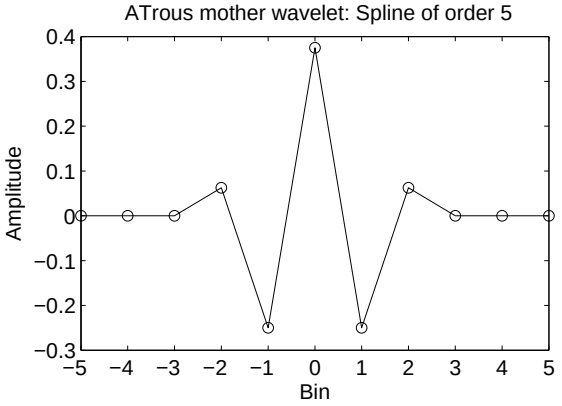


**Figure 2.2:** The mother wavelet selected for the implementation of the 'à trous' algorithm.

The transform is still invertible, but now highly redundant with respect to the sparse wavelet. As a compensation it is shift-invariant: the output of the transform does not depend on the location of the start time of the analysis window, as happens when overlooking some coefficients. For signal detection, it is an interesting property, along with keeping the highest time resolution available. The 'à trous' algorithm is applicable on 2-dimensional data, and has been used in astronomy for noise removal [14].
The chosen mother wavelet, shown in figure 2.2, is very simple, with a small duration allowing high frequency exploration, a symmetry *a priori* useful for timing accuracy while the oscillation is a rough approximation of a common feature in reference waveforms.

#### Implementation

A generic issue with wavelet decomposition of finite size data is the treatment of the edges of data segments. Especially when using the fast algorithm based on the Fourier transform. Standard practices are either to mirror the coefficients about the edge ( $h_{mirror}(-i) = h(i)$ or $h_{mirror}(N + i) = h(N - i)$ for a chunk $[0\ N]$), or wrap the data chunk in a loop to use the values from the other end of the segment ($h_{mirror}(-i) = h(N - i)$ or $h_{mirror}(N + i) = h(i)$). The proposed implementation uses the scheme described in Section 2.2.3, and zero-padding before applying the loop wrapping to guarantee that there is no edge effect.

### Pre-processing

The tested implementation of the transform relies on a whitening pre-process to avoid large variations in the energy density of the different scales, and their pollution by thermal lines. Figure 2.3 shows the decomposition of the DFM a2b4g1 waveform with this implementation of the 'à trous' wavelet transform (ATw).

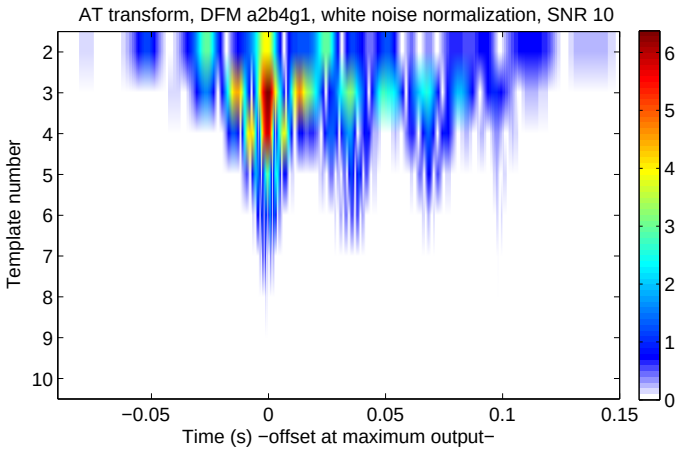


**Figure 2.3:** AT transform of a DFM a2b4g1 waveform, normalized for a white noise background.

## 2.3.2 The S transform

The S Transform (ST) is an invertible transform (see [15] for details) that can be derived from the Gabor transform, by introducing for each sampled frequency $f_s$ an adjusted width $\sigma = 1/f_s$. Its original formula, using the Fourier domain approach of equation 2.15, is :

$$st(h,t,\nu_0) = \frac{\nu_0}{\sqrt{2\pi}} \int_{-\infty}^{\infty} \hat{h}(\nu) e^{-2(\pi(\nu-\nu_0)/\nu_0)^2} e^{i2\pi(\nu-\nu_0)t}\, d\nu(t) \tag{2.24}$$

It can also be seen as a modified Gabor analytic wavelet, of kernel $\phi_s(t,\mu) = \frac{1}{s\sqrt{2\pi}} e^{-\frac{1}{2}(\frac{t}{s})^2} e^{i\mu t}$. For such a complex wavelet, the zero-mean condition is expressed in the Fourier domain as $\hat{\phi(0)} = 0$, verified for $s^2\mu^2 \gg 1$.
The scaling coefficient allows the transform to be inverted, using $\int_{-\infty}^{+\infty} \hat{st}(\tau,\nu)\, d\tau = \hat{h}(\nu)$, for the time series h. Here the scaling factor was modified into $1/\sqrt{2\pi\nu}$, giving a frequency domain kernel equal to

$$\phi(\nu_0,\nu) = \frac{1}{\sqrt{\nu_0 2\pi}} e^{-2(\pi(\nu-\nu_0)/\nu_0)^2} \tag{2.25}$$

With this altered formula (noted $S$ hereafter), the transform of a white noise has a flat profile :

$$S(h,\nu_0,t) = \frac{1}{\sqrt{\nu_0 2\pi}} \int_{-\infty}^{\infty} \hat{h}(\nu) e^{-2(\pi(\nu-\nu_0)/\nu_0)^2} e^{i2\pi(\nu-\nu_0)t}\, d\nu(t) \tag{2.26}$$

The frequency spacing was kept linear, with an overlap between successive templates that grows with frequency, but an alternative non-linear spacing was also tested (see Section D.2). Both are illustrated in figure 2.4. The linear choice requires more templates to cover the same interval and at low frequencies the coverage appears patchy. However, this is the regular method for the S transform, and as such was used for this study. Conversely, the non-linear spacing controls the minimal coverage. Yet toward high frequencies, each template represents a very broad spectral band. Even if taken into account when normalizing, the lower frequency discrimination may affect signal separation.
Another weakness of the S transform comes from its sensitivity to narrow spectral features, especially at low frequency, due to the width of the Gaussian frequency selection. This is most damaging for long lasting features, such as spectral lines. These tend to mask all information over a wide bandwidth, as shown in figure 2.5, in relation with the affected frequency windows.

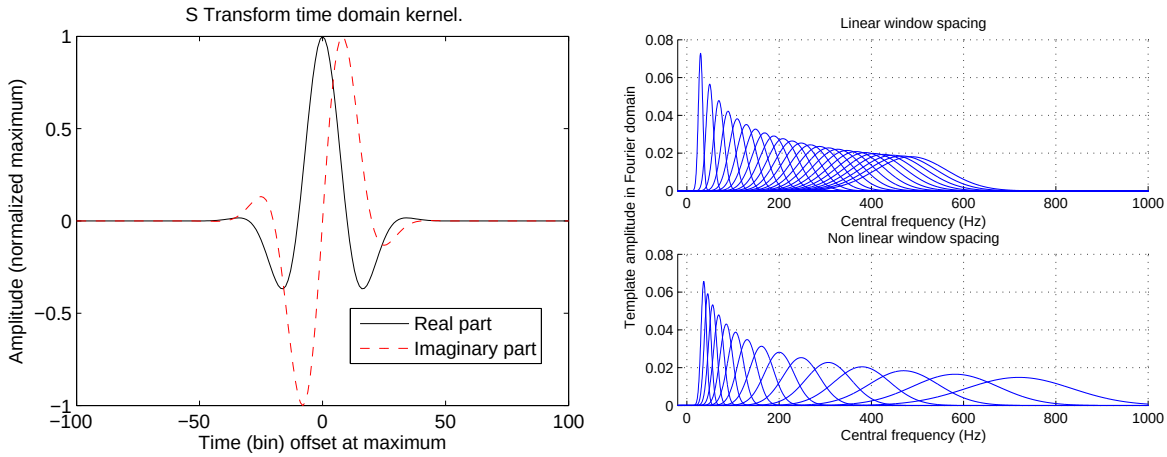


**Figure 2.4:** *Left* Scale invariant S Transform time kernel: the applied kernel is the complex sum of the two plotted polarizations. *Right* Frequency profile of S transform's templates. Two placement methods are shown: regular spacing and non-linear spacing.

### Implementation

The actual computation involves the discrete time definition of the transform, expressed in the frequency domain for efficiency. For N the data bin number, at time $t_j$ and for frequency $f_n$ the transform is expressed as :

$$S_N(t_j, f_n) = \frac{1}{\sqrt{2\pi} f_n} \sum_{m=0}^{N-1} \hat{h}(f_n + f_m) e^{-2\pi^2 f_m^2 / f_n^2} e^{i2\pi f_m t_j} \qquad n \neq 0 \tag{2.27}$$

which does not apply when $f_n = 0$. In this case, the mean of the series is used, computed directly as :

$$S_N(t_j, 0) = \frac{1}{N} \sum_{m=0}^{N-1} h(t_m) \tag{2.28}$$

Formula 2.27 indicates that for each frequency included in the final map, coefficients can be obtained by an inverse FT, after adequate windowing of the FT of the time series. The output of the filter being complex, its squared modulus serves as the output of the transform :

$$S_N(t_j, f_n) = \frac{1}{2\pi f_n} \left| \sum_{m=0}^{N-1} \hat{h}(f_n + f_m) e^{-2\pi^2 f_m^2 / f_n^2} e^{i2\pi f_m t_j} \right|^2 \qquad n \neq 0 \tag{2.29}$$

To work with colored noise, since the method does not take into account the noise power spectral density (PSD), an intermediate step is necessary before isolating events as defined in Section 2.2.4. There are two simple solutions: either use a set of frequency-specific and possibly time-dependent thresholds or normalize the time-frequency map frequency-wise in order to apply a unique threshold.
The latter approach is retained here: for each frequency template, the ST output is normalized to zero mean and unit variance. This normalization is done independently from the quality of the spectral density of the data, notably to improve the adaptivity to a fluctuating noise level.

### Pre-processing

To carry on meaningful analysis, it proved necessary to pre-process the data in order to remove narrow features like thermal lines. Two options are available: targeted feature removal, using for instance Kalman filters as mentioned for figure 2.5, or full data whitening, using a standard algorithm (see Annex C for some details).
Performances for the two configurations are discussed here. As correctly tuned Kalman filters do not affect event detection, as shown in Chapter 3, this comparison illustrates the effect on performances of the waveform alteration introduced by the whitening step.

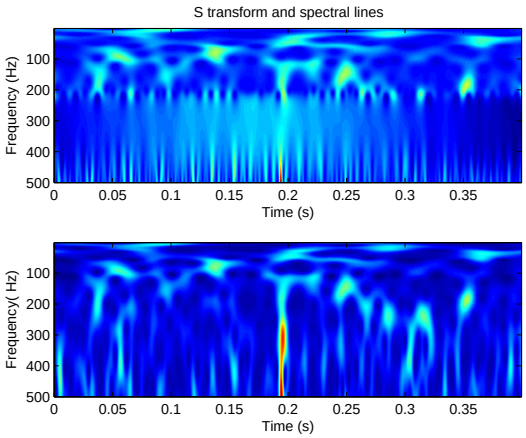


**Figure 2.5:** S Transform and Kalman filtering of thermal lines. Both TF representations are for the same broadband noise and injected waveform (DFM a1b2g1). The top map is spoiled by spectral lines (most notably one at 320 Hz, and a superposed beat effect between close high frequency lines). The bottom map was built after applying Kalman filters (discussed in Chapter 3) to eliminate all lines. The injected signal is visible at time 0.2 s as a broadband feature in the bottom map. It is almost completely hidden by the broad line effect in the top figure.

### Map whitening

This is the pre-thresholding conditioning of a map. It consists in the normalization, for each frequency, of the series of coefficients to zero mean and unity variance :

$$S_N^{white}(t_j, f_n) = \frac{S_N(t_j, f_n) - < S_N(t_j, f_n) >}{\sigma(S_N(t_j, f_n))} \tag{2.30}$$

where the mean and standard deviation are estimates from the current data segment of size N. For the same injected waveform, this background adjustment affects the representation, as illustrated in figure 2.6. For Virgo-type noise, there is a clear visibility enhancement in the best-sensitivity frequency range, from 100 to 400 Hz.

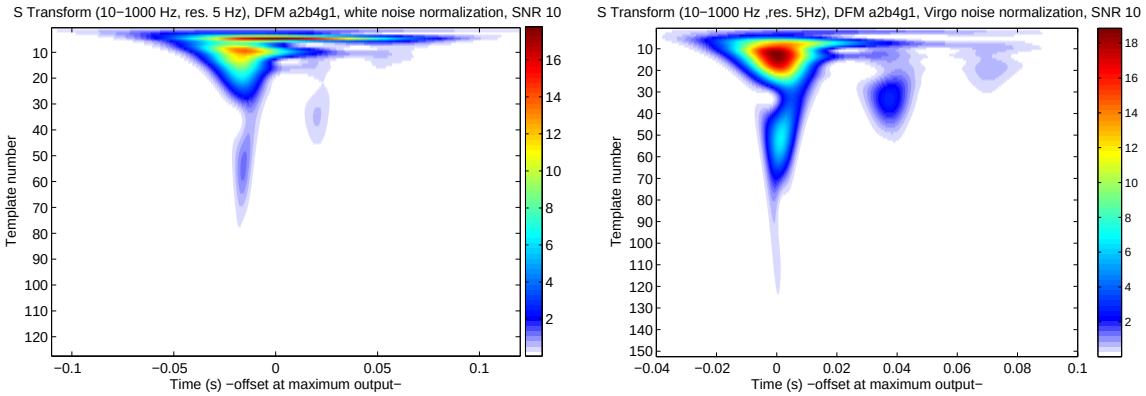


**Figure 2.6:** S Transform of a DFM a2b4g1 waveform, between 10 and 1000 Hz, with a linear template spacing of 5 Hz. The effect of normalization is illustrated: *Left* on white noise, *Right* for Virgo noise (without spectral lines).

Data non-stationarity is not explicitly accounted for. This is done when data statistics are estimated, independently for each ST map. Because the quality of the map whitening process depends on the accuracy of the first statistical moments, it appeared that increasing the map duration could affect performances: estimators derived from longer time series should be more accurate. This dependency is even more important when using self-normalization, where a well-localized signal might be partially suppressed with respect to the noise background.

A clear effect is visible in figure 2.7, that most interestingly concerns almost exclusively the valid detection-type events. Obviously, noise non-stationarities of time-scales below the map duration will not be treated properly. This is potentially an issue for non-Gaussian (real) data.

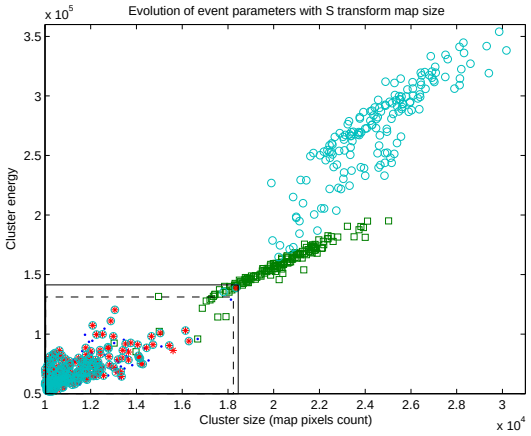


**Figure 2.7:** Evolution of event energy and size for an increased map size, for a 4ms Gaussian waveform. Noise events are marked . and * , for a map size of $2^{16}$ and $2^{18}$ bins, □ and ∘ indicate signal events respectively for the same sizes. Boxes enclose the noise events.
Events were obtained from a noise only analysis (noise events), and a signal + noise analysis (signal events), from which events matched in the noise events list were discarded. Signal events falling in the noise box can be interpreted as noise structures enhanced by their proximity in time to the injected signal.

### 2.3.3 Exponential Gaussian Correlator

This is an application of matched filtering, like the PC method, with a different kernel shape. The motivation for using match filter was improving the robustness of the transform with respect to spectral features. Thanks to the match filter formula, the noise spectral density is treated in the transform and the outputs are normalized to be compatible with the Wiener filter SNR, without the need for a map whitening step. As this is done at the frequency resolution of the PSD, thermal lines, if stable in time, are not an issue.
Complex Exponential Gaussian envelop (EG) waveforms are described by two free parameters, the oscillation frequency $f$ and the width of the Gaussian window $\sigma$. In relation to the Heisenberg resolution limit, another couple of parameters is favored: (f, Q) with $Q = \sigma \times 2\pi f$ a quality factor. Hence, for EG templates :

$$\begin{aligned} \phi_{f_0,Q}(t) &= e^{-t^2 2\pi^2 f_0^2/Q^2} e^{-i2\pi f_0 t} \\ \Phi_{f_0,Q}(f) &= \frac{1}{\sqrt{2\pi}} \frac{Q}{f_0} e^{-(\frac{f-f_0}{f_0})^2 Q^2/2} \end{aligned} \tag{2.31}$$

The match between data and a given template is then :

$$c_{(f_0,Q)}(t) = \frac{1}{\sqrt{2\pi}} \frac{Q}{f_0} \int_{-\infty}^{\infty} \frac{e^{-(\frac{f-f_0}{f_0})^2 Q^2/2} \times H^*(f)}{S_h(f)} e^{i2\pi f t}\, df \tag{2.32}$$

Note that in this case (complex-valued templates) c is a complex.
An essential element is that the correlation values in equation 2.32 are indexed in time, frequency and quality factor (or duration). This additional information can be exploited to constraint event coincidences on extra characteristics, or to describe event populations.

While no signal could match a complex domain template, the orthogonality (defined as a null correlation) between the real and imaginary parts

$$e^{-t^2 2\pi^2 f_0^2/Q^2} \cos(2\pi f_0 t) \qquad \text{and} \qquad e^{-t^2 2\pi^2 f_0^2/Q^2} \sin(2\pi f_0 t) \tag{2.33}$$

makes this implementation equivalent to the use of both Gaussian-Cosine and Gaussian-Sine real templates. In the case of a well-matched Gaussian-Cosine/Sine signal, the output SNR of EGC is only $\frac{1}{\sqrt{2}}$ of the optimal reconstructed value. For any other signal, the comparison to Wiener filtering is not meaningful, so this scaling effect is not corrected for.
The approximate ambiguity function, introduced in Section 2.1.2, for EG templates is :

$$\Gamma_{EG}(f_1, Q_1, f_2, Q_2) = \sqrt{2}\sqrt{\frac{f_1/Q_1 \times f_2/Q_2}{(f_1/Q_1)^2 + (f_2/Q_2)^2}} \times e^{-\frac{(f_1-f_2)^2}{2((f_1/Q_1)^2+(f_2/Q_2)^2)}} \tag{2.34}$$

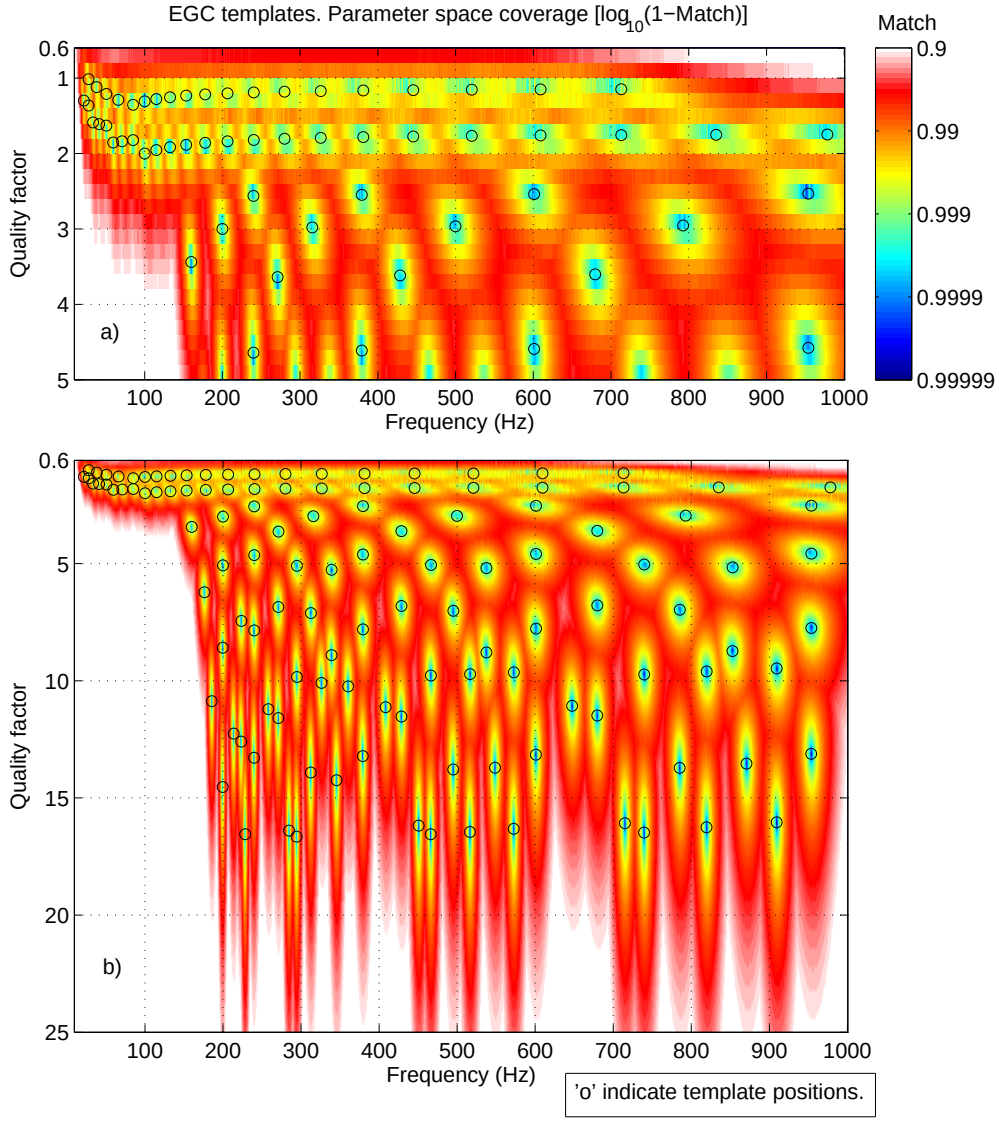


**Figure 2.8:** Coverage of the (f, Q) parameter plane with the selected EG tiles. Figure a) is a close-up of the low Q region of b). Both figures show a circle for each template, and a color scale indicating at each point the maximum match between the waveform corresponding to these parameter values and the templates in the list. It was built by computing the match at random locations in the plane with all templates in the list, then interpolating to create the actual plot.

The full EG ambiguity function is close to what is obtained when separating real and imaginary parts (Gaussian cosine and sine), with a simpler normalization from the single complex exponential involved.

The parameter space is bounded by minimum and maximum frequency and quality factor plus a maximum template length, estimated by the width of the Gaussian envelope $\sigma_{max} \geq \frac{Q}{f}$. This ensures that only short duration structures would be matched, at any frequency. With these elements, a bank of templates of close-to-minimal size was obtained by calling an *ad hoc* tiling algorithm [4], applicable when the ambiguity depends on two parameters, as for EG templates.
The retained list of template parameters is shown in figure 2.8, with the obtained coverage of the parameter space. Two areas were defined in the parameter space. For quality factors above 3, well-matched signal candidates would be oscillatory with a frequency close to a template value. The short duration hypothesis allows to discard low frequencies, and cover $100 \leq f \leq 1000$ Hz. The upper bounds in frequency and quality factor, $Q \leq 16$, are arbitrarily set to limit the number of templates. Templates with $1 < Q \leq 3$, have more generic shapes, from Gaussian-like to 'Mexican-hats' for the cosine polarization, respectively at $Q \approx 1$ and higher values of Q, and symmetric 'double-peak' for sine polarizations. It seemed important to cover a large range of waveform durations, hence the limits $10 \leq f \leq 1000$ Hz. For quality factors below 1, the approximate ambiguity function 2.34 is much less accurate, while templates do not exhibit additional shapes.

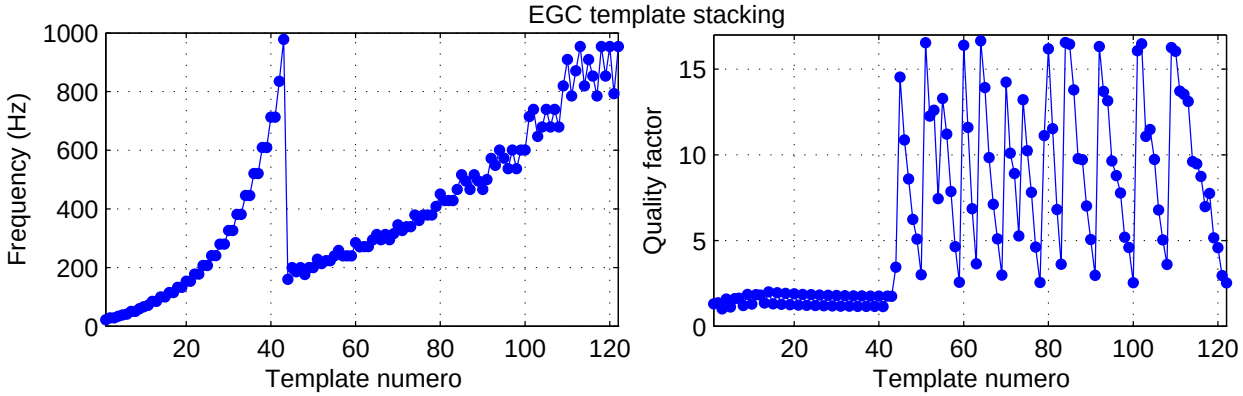


**Figure 2.9:** Order of EGC templates in the output time-frequency map.

Once selected the templates, care must be taken of the order they are stacked in the time-frequency map. When implementing a discriminating clustering algorithm, it is necessary to reproduce the time-narrowing behaviour identified with increasing frequency for single Q templates. For the griding scheme, the templates are ordered by groups of equal Q and increasing frequency, with Q decreasing between successive groups. For the tiling scheme, parameters cannot be expected to remain equal between templates. As shown in figure 2.9, templates with $1 < Q \leq 2.2$ are ordered by increasing frequency while for higher Q, they are regrouped by 50 Hz wide frequency bands, where they are ordered by decreasing quality factor.
As with any matched filtering, spurious matching with random time series (that do have the same form as the template) cannot be discriminated from low SNR exact matches. Thus only high SNR values can be retained with confidence.
As for the S Transform, it is the squared modulus that serves in subsequent analysis :

$$EGC_{(f_0,Q)}(t) = \frac{1}{2\pi}\frac{Q^2}{{f_0}^2}\left|\int_{-\infty}^{\infty} \frac{e^{-(\frac{f-f_0}{f_0})^2 Q^2/2} \times H^*(f)}{S_h(f)} e^{i2\pi f t}\, df\right|^2 \tag{2.35}$$

Illustrations of waveform transforms are given in figure 2.10 while the similarity with the S Transform for a similar template placing is shown in figure 2.6. When varying Q, and stacking templates as described above, the interpretation of the resulting map is more complex. Whereas ST provides imprecise but consistent event frequency estimations, the result for EGC may be less reliable, due to low Q templates. A match with the real (symmetric) polarization at low Q corresponds to a Gaussian-like waveform, for which the frequency information is less relevant than characteristic duration $\frac{Q}{f}$, that can be recovered for individual templates.
EGC and ST differ mostly by the signal extraction / rejection quality of EGC, related to match filtering. While the absence in the time series of oscillatory-type or near-Gaussian shapes will give low outputs with EGC, ST only highlights energy concentration at different frequency and time scales, for noise and signal alike.

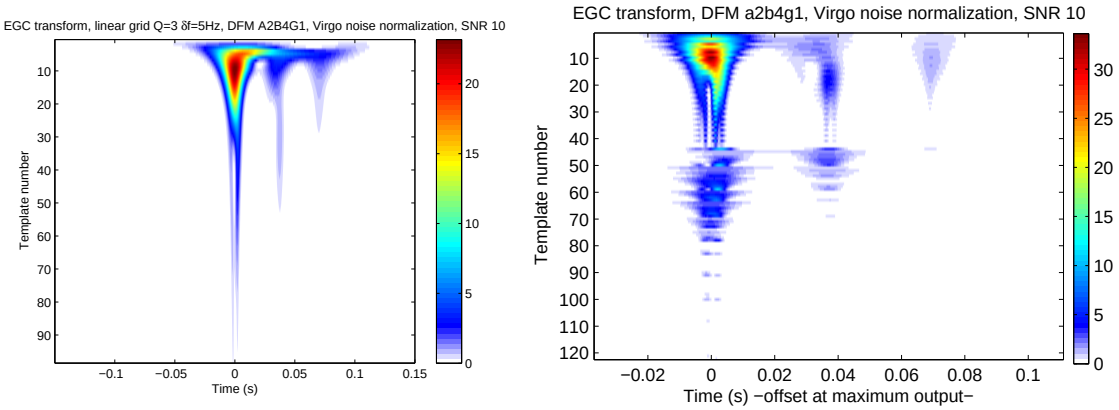


**Figure 2.10:** EGC transform of DFM a2b4g1 waveform, with a colored noise normalization. *Left* The templates follow the regular spacing scheme used for ST, with a distinct Q=3. *Right* The templates were selected using the tiling algorithm and equation 2.34.

### 2.3.4 Statistical distributions

Using single-template configurations, the output value distribution is recovered.
The AT transform is linear and it is applied on whitened data, with zero mean and variance $\sigma$, hence the probability distribution of its output follows equation 2.5 mentioned for Wiener filtering.
ST and EGC initially produce complex-valued coefficients. Both real and imaginary parts are linear transforms of the input time series. Thus here they both follow a zero-mean Gaussian distribution, with standard deviation $\sigma$. When extracting the square modulus, the probability density function is changed into $f_{ST}(y) = \frac{f(\sqrt{y})+f(-\sqrt{y})}{2\sqrt{y}}$ for $y \geq 0$, $f_{ST}(y) = 0$ otherwise. This expression simplifies into :

$$f_{ST}(y) = \frac{1}{2\sigma^2} e^{-\frac{y}{2\sigma^2}} \qquad \text{for } y \geq 0 \tag{2.36}$$

known as the exponential distribution (of parameter $\lambda = \frac{1}{2\sigma^2}$), and recovered in simulation for EGC (figure 2.11).
Considering instead the modulus of the filter output, a Rayleigh probability distribution is obtained :

$$\begin{aligned} f(x) &= \frac{x}{\sigma^2} e^{-\frac{x^2}{2\sigma^2}} \qquad \text{for } x \geq 0 \\ f(x) &= 0 \qquad \text{otherwise} \end{aligned} \tag{2.37}$$

with the same standard deviation as the Gaussian variables. For simplicity, the exponential distribution was preferred.

Knowing the filter output distribution, the event probability from Gaussian noise for a selection threshold $\phi$ is :

$$\tau_{AT}(\phi) \approx \frac{1}{\sqrt{2\pi}\sigma} \int_{\phi}^{\infty} e^{-u^2/2\sigma^2}\, du \qquad (= \frac{1}{2}\, erfc\,(\frac{\phi}{\sqrt{2}\sigma})) \tag{2.38}$$

$$\tau_{EGC}(\phi) \approx \lambda \int_{\phi}^{\infty} e^{-u\lambda}\, du \qquad (= e^{-\phi\lambda}) \qquad \text{for } x \geq 0 \tag{2.39}$$

This provides a false alarm rate estimate, to be corrected for any event manipulation, like time coincidence or selection from secondary parameters, as discussed below. See [7] for more detailed false alarm rate estimations for a non-optimal filter in the Gaussian noise hypothesis. It is expected that real data will differ from the Gaussian model, and the obtained filter output distributions as well.

The template bank logic does introduce irregularities in the frequency distribution of events, as shown in figure 2.12. This comes in part from the quality factor parameter, hidden in this distribution. In any case, the average peak energy, shown in the same figure, is close to flat. This confirms that the method is not biased with respect to event frequency, and allows an eventual discrimination of event groups according to frequency.

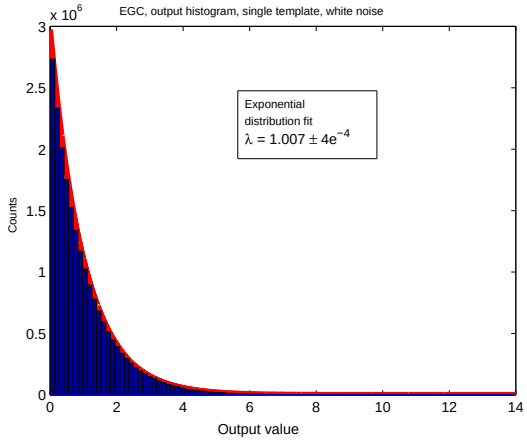


**Figure 2.11:** Distribution of EGC coefficient value for a single template analysis, on Gaussian noise.

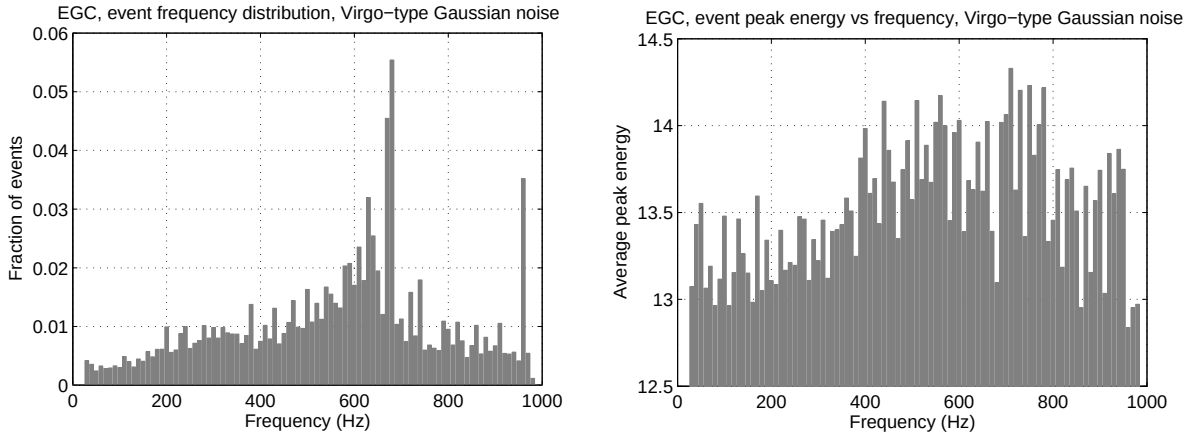


**Figure 2.12:** Distribution of events according to composite frequency. *Left* Event distribution, normalized to total event number. Large irregularities are introduced by the template bank. *Right* Event averaged peak energy, smoothing out most of the irregularity.
Results obtained from 24 h of Virgo-type simulation data.

### 2.3.5 Event clustering algorithm

Given the possibly complex TF structure of astrophysical signals (see for example figures 2.6 and 2.10), some clusters that belong to the same signal could be splitted into different events, as defined in Section 2.2.4, by the threshold on coefficient value. Associating these 'orphan' clusters would increase the visibility of the signal in the final event list.
This is obviously complicated by the risk of combining noise events. Some descriptive properties can be extracted for each event: start, central and end (barycentric or mean) values for time and frequency, summed 'energy' and size.
The most evident clustering algorithm considers that all neighbouring (in 8-connectivity, including horizontal, vertical and diagonal connections) selected pixels belong to the same event. This reduction is achieved here using the Hoshel-Kopelmann algorithm, summarized in figure 2.13, which requires one sweep only to group connected pixels. The standard algorithm [17] is completed by a border-bridging step, to merge clusters artificially splitted at map generation due to data segmentation.

To include *a priori* information, qualitative expectations for the energy distribution in any TF plane were tested: a localized oscillation (for instance a Gaussian-cosine with a low Q) has a narrower time expansion at higher frequency, so coincidence of events could be tested by decreasing central frequency, and only strict time inclusion considered as valid. The model signal, that would be well reconstructed, would be composed of a (relatively) long duration "base" component at low

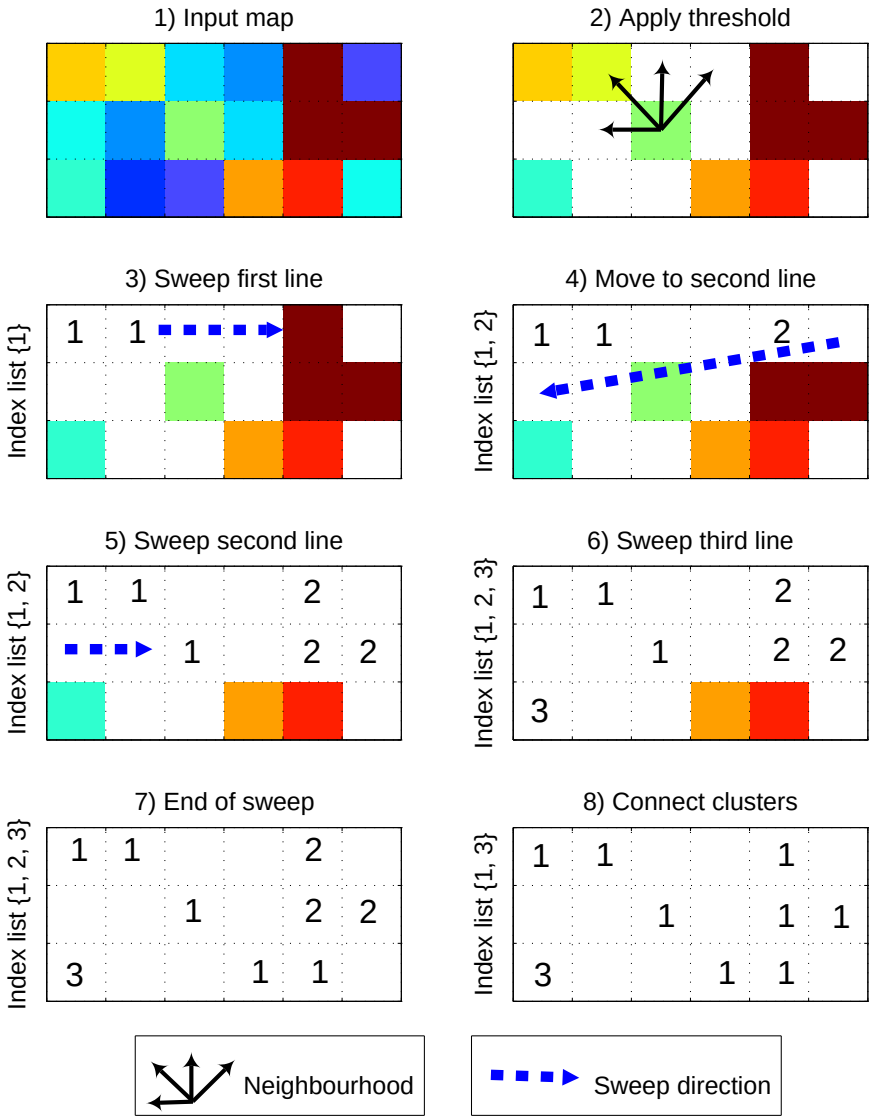


**Figure 2.13:** Illustration of the Hoshel-Kopelmann clustering algorithm.

frequency plus eventually shorter ones at higher frequency, all occurring within the "base" time window. This is the case in figure 2.6.
This scheme has several drawbacks, notably the necessity of a low frequency component to hold all higher frequency structures together. This hypothesis on signal structure does not necessarily hold, for instance for oscillatory waveforms, and it could prove difficult to maintain for low SNR signals, where any low frequency part could be missed as noise background.
Hence an alternative clustering method was selected, where three thresholds are applied :

- a) Background restriction : A low threshold is applied to map coefficients, to discard most of the noise-consistent elements.
- b) Clustering : Events are created from all adjacent remaining pixels.
- c) Simultaneity test : Events overlapping in time or separated by less than a set delay are merged.
- d) Energy selection : The candidate list contains only events with a total energy above a final threshold.

In time-frequency maps, the noise background for ST shows many wide-spread ridges of pixels with low to intermediate values. This is not the case for EGC so an additional clustering is possible,

using 'background suppression'. Between b) and c), a threshold higher than in step a) is applied to cluster elements, to remove as much as possible of the remaining noise coefficients, without separating embedded higher energy structures. This allows a lower initial threshold, hopefully preserving more of the signature of a signal.
To produce ROC curves, a varying energy threshold is applied at step d). The peak energy is used, as it was found to give the best results. An investigation of the threshold choice is presented in Annex D.

## 2.4 Monte Carlo performance studies

Once set the analysis chain and the filter parameters, performance tests were carried out, taking advantage of the LIGO-Virgo analysis exercise. This allowed direct comparison of the filter with other methods developed for the same purpose. Using candidate waveforms, the efficiency of the methods is characterized through Receiver Operating Characteristics (ROC) curves [8], where detection efficiency is plotted against false alarm rate, without explicit mention of the thresholding algorithm nor values.

### 2.4.1 Data

Though data from operating instruments does not follow a Gaussian distribution, this is the minimum hypothesis model, and as such a necessary first step in the evaluation of analysis methods. Both white and colored noise power spectral densities are considered. White noise provides an absolute limit on filter performances, while colored noise brings us closer to real data.

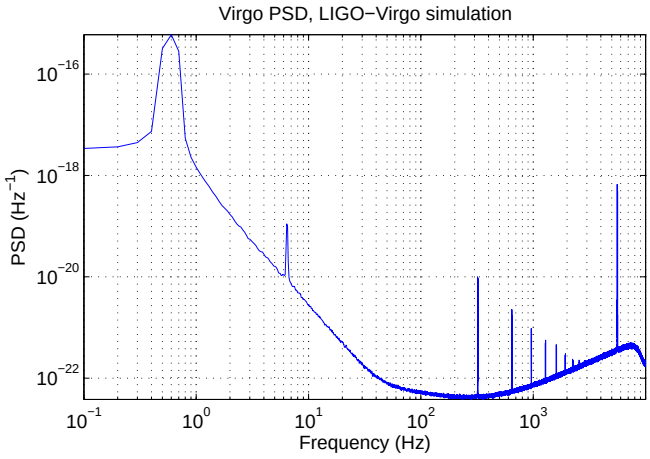


**Figure 2.14:** Simulated Virgo noise Power Spectral Density, for the the time series used for algorithm comparison by the LIGO-Virgo joint working group.

Note that pre-processing spectrum-whitening methods, as they allow a simplification of data properties, may be required by the transforms, as will be precised in the text, but the signal alteration they introduce and its negative effect on performances is not specifically discussed.

The noise series used here is a three hours stretch produced for the joint LIGO-Virgo analysis group. The power spectral density is close to the target Virgo sensitivity, see figure 2.14, including for spectral lines due to the suspension system or mirror internal resonance modes, as distinctive features of Virgo. The main differences are the drop at high frequency, a data generation artefact, and the absence of the very low frequency seismic component, to reduce the dynamics.
All analysis are done with the same noise, allowing direct comparison of detection efficiency from limited duration data.
The test waveforms used in this work were chosen to cover very different categories. There are six regular waveforms: two Gaussian signals, of characteristic duration $\sigma_t$ 1 and 4 milliseconds, plus four Gaussian-cosine waves, of frequency 235 and 820 Hz, and quality factor Q 5 and 15, derived from the duration $\sigma_t$ of the Gaussian envelop by $Q = 2\pi f_0 \sigma_t$. The last two signals come from the DFM catalog mentioned in Chapter 1, figure 1.6.

Injected amplitudes are normalized in units of SNR, as described in Section 2.1.1. Where two results are provided for the same signal, they concern SNR values 10 and 5.

### 2.4.2 ' à trous' performances

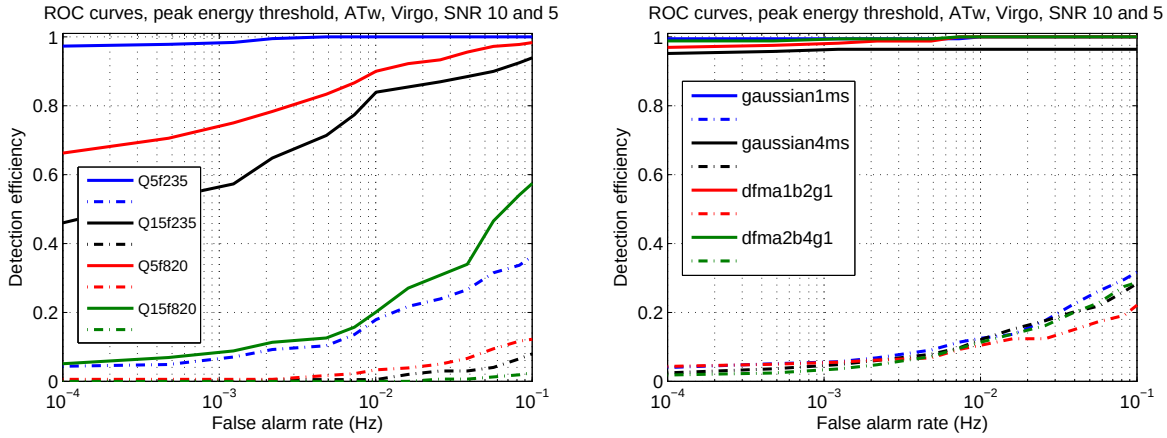


**Figure 2.15:** ATw ROC curves. *Left* for Gaussian-cosine waveforms. *Right* for Gaussian and DFM waveforms. All injected with SNR 10 -plain lines- and 5 -dotted lines-.

The low detection efficiency at low false alarm rates, for high frequency signals even at SNR 10, and the overall poor performances for SNR 5 indicate that this simple wavelet filter is not adapted to the circumstances.

### 2.4.3 S Transform

#### Generic remarks

All waveforms were processed with the same detection chain.
Owing to the sensitivity of the transform to spectral lines, pre-processing of some sort is required. Two solutions were partially compared. The first series of results, of figure 2.16, were obtained with a noise without spectral lines, assuming that perfect line removal was possible. The second series, summarized in figure 2.17, applied a commonly used whitening algorithm to suppress most of the dynamic of the colored noise, including lines.
The first threshold was defined beforehand, using simulated Virgo noise to test the analysis pipeline, as a compromise between signal suppression and noise events density. It remained fixed for all the analysis. The second one can be changed for a given list of clusters. This is used to vary the lists of selected noise and injection events according to their energy and therefore build ROC curves.
In all the presented ROCs (for the same parameters), there is a similar efficiency relation with false alarm rate. In particular the same noise events are responsible for the low false alarm part of the ROCs, and the abrupt increase in efficiency before reaching $3 \times 10^{-4}$ Hz alarm rate. This effect would probably be suppressed when improving the statistics.

#### Line removal pre-processing

As higher frequency resolutions improve signal extraction, a central frequency spacing around 2.5 Hz was selected. To limit computer resources demands, the frequency band was limited to 10 - 500 Hz, except for DFM a1b2g1.
Compact waveforms, in the TF sense, are the most easily recovered, as their SNR is very localized. This is true for both Gaussian and Gaussian-cosine waveforms considered. Performances, summarized in figure 2.16, are the best for Gaussian injections, on par with other algorithms (in [8] for instance). There is a decrease in performances for Gaussian-cosine, that are well localized but at higher frequencies, where there is more spread of both noise and signal over the templates.
The DFM waveforms have much more complex structures. Thus, their S Transform representations are more diluted, making the injection harder to differentiate from noise events, which implies lower performances.

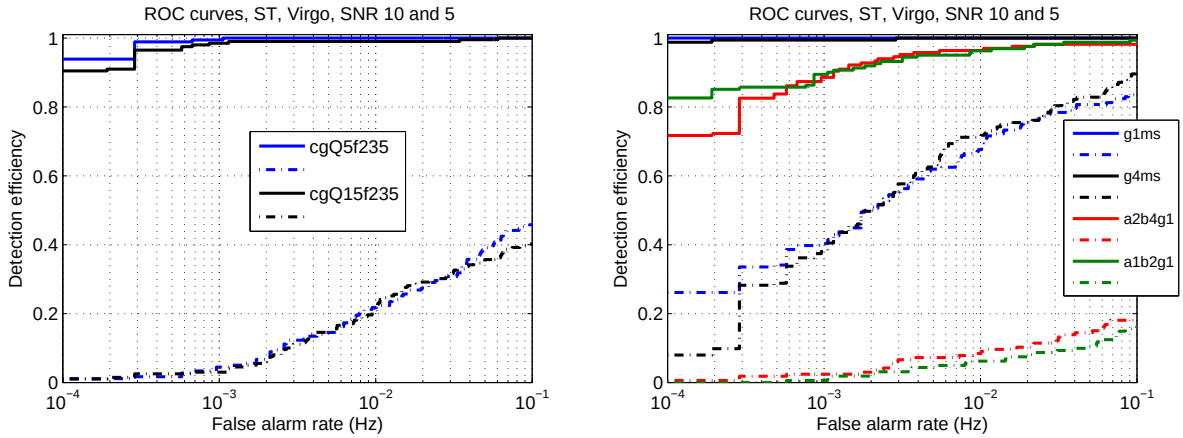


**Figure 2.16:** ST ROC curves. *Left* for Gaussian-cosine 235 Hz waveforms. *Right* for Gaussian and DFM waveforms.
All curves were obtained with a 10-500 Hz analysis, except for a1b2g1, where the 10-1000 Hz range was first introduced. The limited band explains the absence of 820 Hz Gaussian-cosine. Injected SNR: 10 -plain lines- and 5 -dotted lines-.

For the a1b2g1 waveform, the transform cut raise, to 1 kHz, was required by the spread of the waveform energy to higher frequencies. Although an increase in the number of false alarms was expected, the achieved performances are very close for both DFM waveforms, and unimpressive.

### Data whitening pre-processing

To complement this study of the performances of the S Transform, a whitening step was introduced (hence STw in the figures) as an alternative for spectral regularization, in place of the Kalman filters, with results in figure 2.17.
Consider first the SNR 5 injections. Gaussian-cosine, with no energy located at low frequency, should not be affected. For the 235 Hz signals, there are some local differences in the curves, but no overall performance change.
Waveform alteration from the whitening step notably affect Gaussian shapes, and this is the probable reason for the large drop in performances. Actually, the 'whitened Gaussian' seem to be no more visible to the filter than the DFM waveforms, which are not touched by the pre-processing.

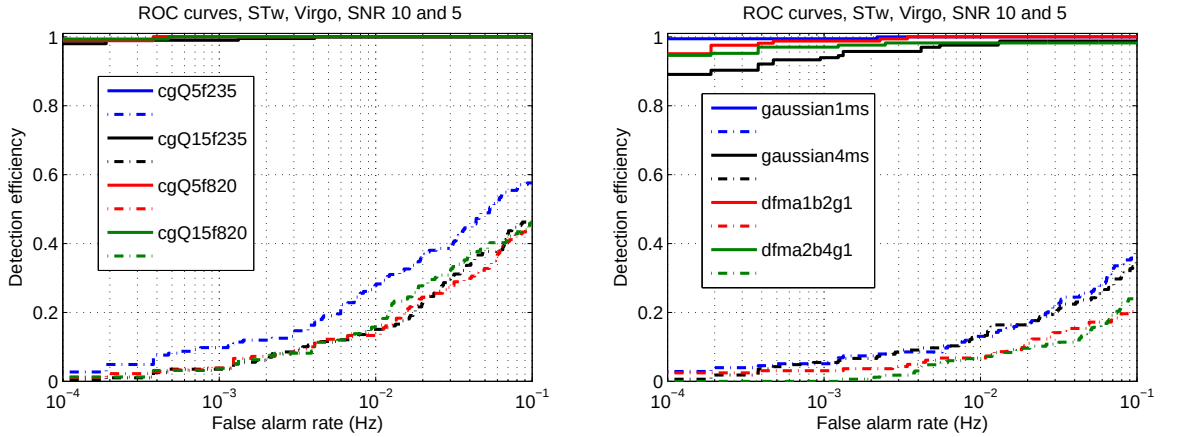


**Figure 2.17:** STw ROC curves. *Left* for Gaussian-cosine waveforms. *Right* for Gaussian and DFM waveforms. All injected with SNR 10 and 5 (ordered by decreasing efficiency).

The conclusion would be clearly not to use the whitening pre-processing, except that at SNR 10, there is a notable gain for DFM waveforms at all false alarm rates. This might originate in performance alterations for ST, possibly due to the Kalman filters. Re-estimation of ST performances on smooth Virgo-type PSD is under way.

### 2.4.4 EGC performances

Using the same data set and injected waveforms, the performances of the EGC filter were tested. Overall performances are satisfying, there are no unexpectedly good results. For Gaussian-cosine waveforms, the filter is at its best, as it was tuned to match these waveforms. For Gaussian and DFM signals, templates with a quality factor around 1 are useful, as the cosine polarization is then close to a Gaussian shape.

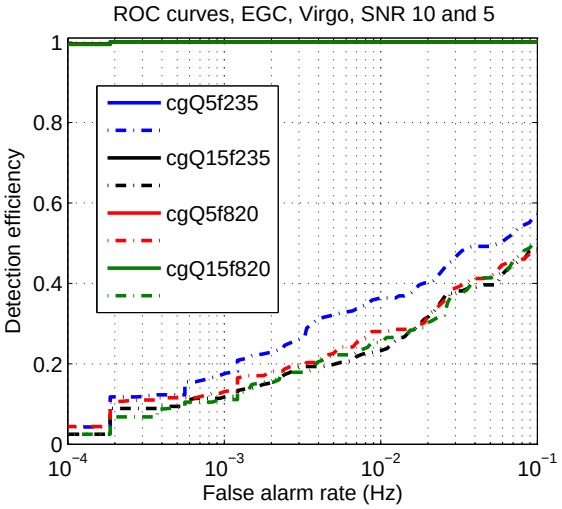


**Figure 2.18:** EGC ROC curves for Gaussian-cosine waveforms, injected with SNR 10 and 5 (ordered by decreasing efficiency).

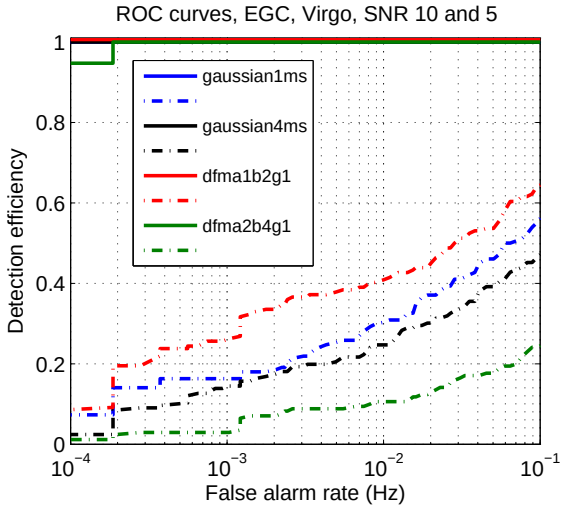


**Figure 2.19:** EGC ROC curves for Gaussian and DFM waveforms, injected with SNR 10 and 5 (ordered by decreasing efficiency).

#### Events characteristics analysis

The nominal behaviour of the filter is obtained with the Gaussian-cosine signals. The similarity of the performances as summarized in the ROC curves of figure 2.18 illustrates this point. Figure 2.20 shows for detection events parameters for the peak template. Peak frequency accuracy is good for both waveforms, with a larger spread for the 820 Hz signal. Overall the same is true for quality factor, to a lesser extent. This is related to tolerance to parameter error in a match filter approach as illustrated by the (f, Q) plane coverage mapped in figure 2.8. Remark that those observations are not SNR-dependent, again in agreement with match filtering principles.
This is different for SNR estimation. For injections at SNR 10, a perfect reconstruction with EGC would give $10^2/2 = 50$, consistent with simulations. Simulations give a $\pm 20$ extra variation from noise. For SNR 5 signals, it is difficult to conclude much, except a larger spread of estimated SNR. This is a positive effect, given that optimum value would be SNR 12.5, where noise events become frequent.
The duration of the signal also affects extracted events, as best seen again for the Gaussian-cosine waveforms, figure 2.21. For similar peak energies the total energy is increased by a factor slightly larger than 3, while the duration ($\sigma$ of the waveform envelop) varies between 3 ms and 10 ms, in agreement with the definition $E_{cluster} = \sum {E_{pixel}}^2$.
Note finally that the averaged energy per pixel seems to be higher for signal events than noise events. This is extrapolated from the linear relation observed for noise events between size and total energy, and the position of signal events, most clearly for SNR 10 injections, above that line.

The two DFM waveforms were selected to provide very different characteristics. This difference is indeed kept in the output of the EGC filter, see figure 2.19, but the detection principle applies equally. It is illustrated in figure 2.22, that shows how the polarizations of EGC templates match the main structure of the signal. For both the Gaussian-cosine shape fits the initial peak, and maybe the second one for DFM a2b4g1, with a similar shape. They are all at low quality factors (figure 2.23), something to be expected for signals without long oscillation. Note that the match between EGC templates and the signal peak is worse for a2b4g1, as the amplitude of the structure is lower.

This difference and the lower amplitude of all features of a2b4g1, that are also longer, give lower peak energies at low quality and low frequency. The possibility of recovering a good efficiency by changing the sorting parameter is discussed in Annex D.1.

The event duration distribution confirms the behaviour for each waveform seen for event size. In addition, it appears that noise events of all durations are found, up to about 0.1 seconds. There is no signal discrimination possible from this parameter.

### Timing accuracy

Timing accuracy is very good, as illustrated in figure 2.24, with at SNR 10 an average bias below the millisecond for all signals, with average delay below the millisecond for most signals, except DFM a2b4g1, and always less than 2 ms. This distinctive delay for a2b4g1 comes from the asymmetry of the waveform near its maximum absolute value (the timing reference). As seen in figure 2.22, the match takes into account the whole peak, not the small asymmetry. The variance is also small, below the millisecond except for Gaussian-cosine 235 Hz Q 5. As expected, shorter ($Q = 5$ compared to $Q = 15$) Gaussian-cosine are better located. For the Gaussian $\sigma = 4$ ms the performance is particularly good, of the order of match filtering, as expected from the discussion on figure 2.22.

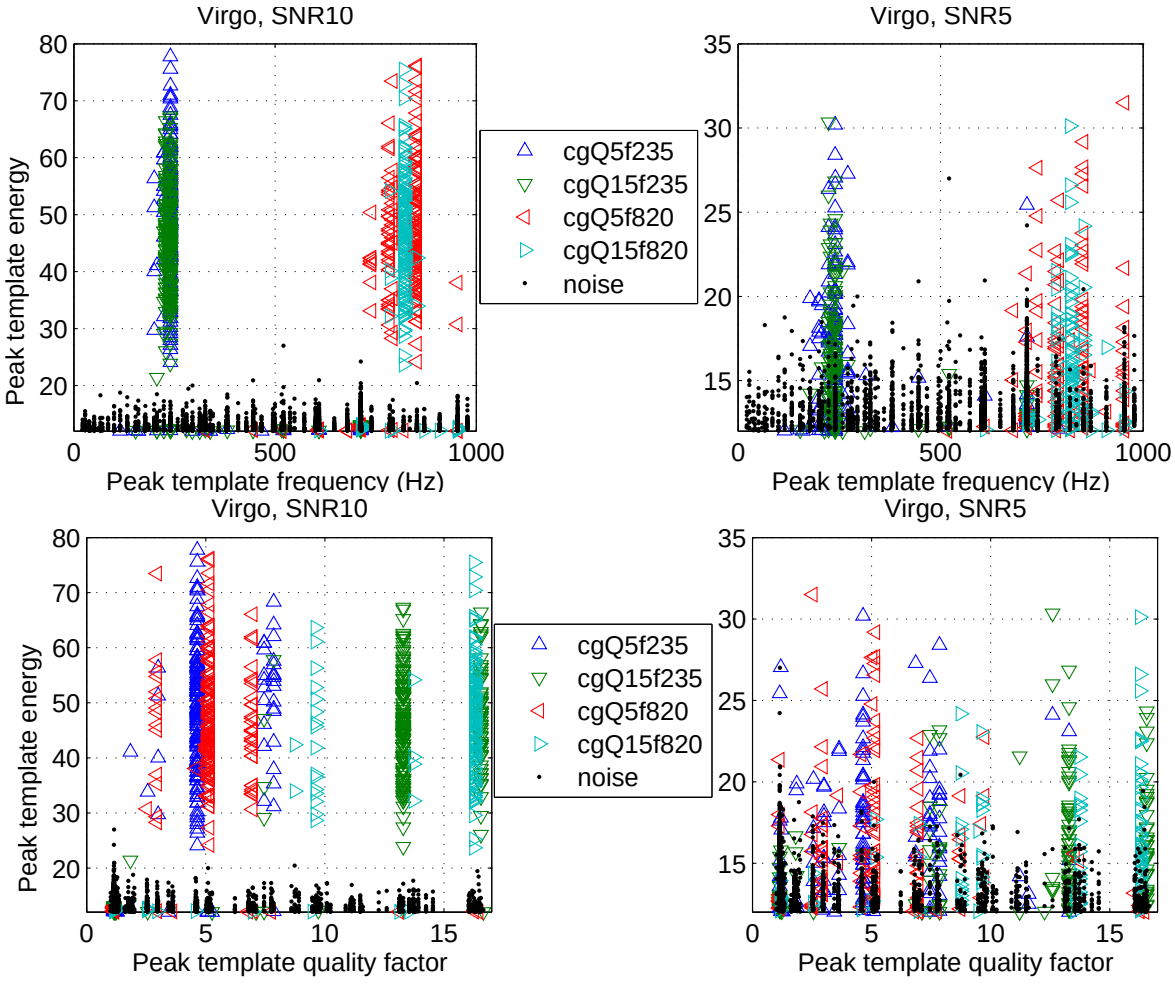


**Figure 2.20:** EGC trigger characteristics for Gaussian-cosine injections. For all events, grouped by category, noise false alarm or injected waveform, extracted parameters are plotted pairwise : *Top* Peak energy against peak frequency. *Bottom* Peak energy against peak quality factor.
Injected SNR 10 (*Left*) and 5 (*Right*).

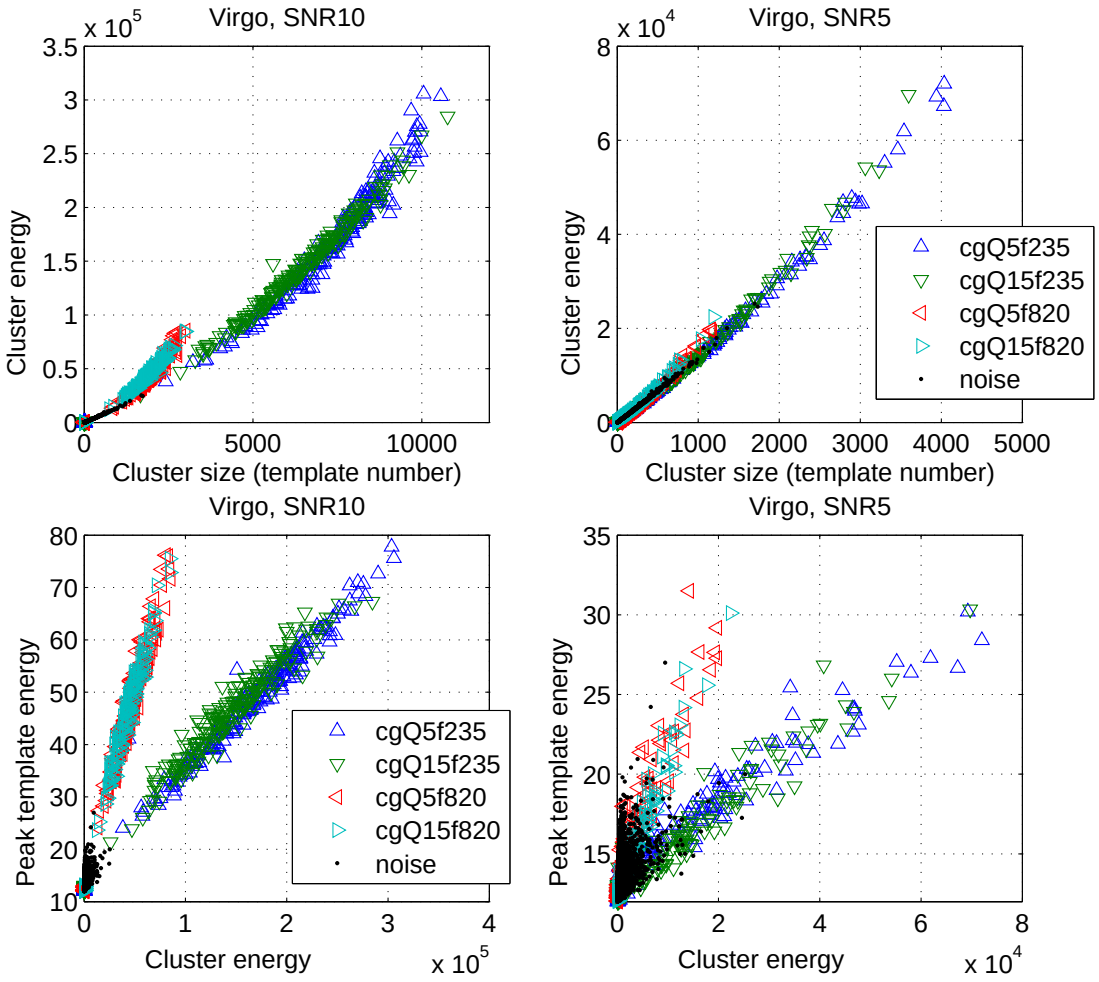


**Figure 2.21:** EGC trigger characteristics for Gaussian-cosine injections. All events are shown, identified by type. Plotted parameter pairs are : *Top* Event total energy against size (pixel number). *Bottom* Peak energy against event total energy.
Injected SNR 10 (*Left*) and 5 (*Right*).

### 2.4.5 Monte Carlo conclusion

Even though the amount of data was not very large, it was sufficient to establish the interest of the S Transform analysis as described above. Performances were on par with other methods, but not better, and at the cost of specific line-removal to suppress all narrow-band features, a data-cleaning process that might prove difficult to reproduce on real data.
Unless data pre-processing is shown to be efficient enough, with line removal and perhaps spectrum whitening, this method seems to be too fragile with respect to noise behaviour. This was the main argument for testing EGC, where noise is normalized using the PSD.

## 2.5 Comparison to other time-frequency filters

The three transforms introduced above have similar oscillatory kernels, though different pathways for extracting the information for a given time-frequency location. As can be expected, similar paths have been explored elsewhere. In this section alternative algorithms are introduced and some elements of comparison are proposed.

### 2.5.1 Description of equivalent filters

**Wavelet analysis** The 'à trous' algorithm is a simple wavelet transform, with limited frequency resolution. A more evolved wavelet application has been developed in the LIGO collaboration, the Waveburst filter [20].

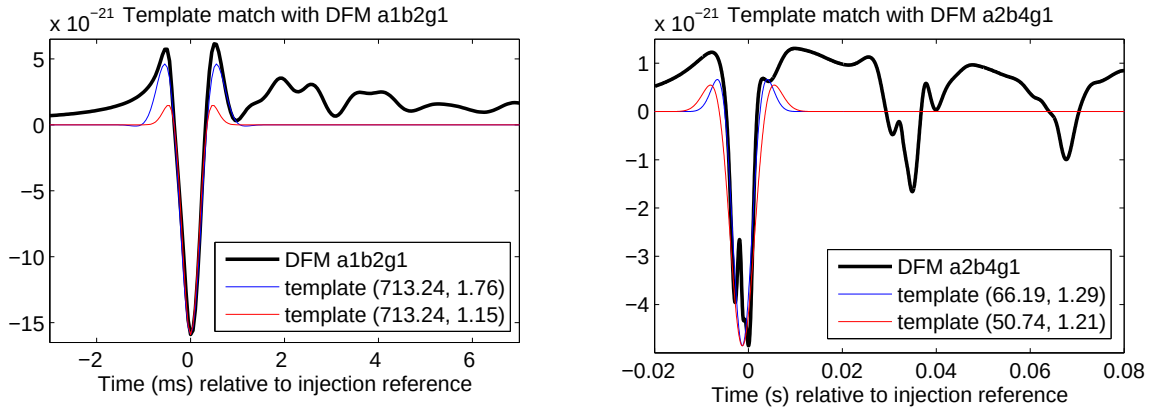


**Figure 2.22:** Match of EGC templates with waveform structures : *Left* with DFM a1b2g1. *Right* with DFM a2b4g1.

Waveburst decomposes the time series over a wavelet tree, to keep a linear frequency spacing, that includes several wavelet families. The final decomposition sieves through the available coefficients to retain the highest values. Event extraction was originally designed for a multi-instrument configuration, which complicates performance comparison.

**Short Fourier transform** The S Transform can be compared to excess power filters, like Power Filter [21], developed in the Virgo collaboration.
Power Filter (PF) produces TF information on coarse-resolution overlapping frequency bands, from short duration Fourier transforms of different lengths. Each band is normalized separately, and relevant coefficients are compared to select the highest power with a reduced overlap at each time.
This is a much more evolved algorithm than ST, although built from the same windowed-Fourier transform. PF was included in the LIGO-Virgo filter comparison work, discussed further down.

**Template bank method** As for EGC, it is close to the Q transform (QT), also from the LIGO collaboration, described in [22].
In QT, a Hanning-shaped complex exponential kernel is applied in groups of fixed quality factor (ratio between window width and wave frequency). These groups are then compared in order to extract maximum-amplitude non-overlapping coefficients. Some sparsity is gained by defining for each template a time coverage, and only computing the transform for adjacent times. A specific anti-causal whitening pre-processing step is included.
QT was also part of the LIGO-Virgo study.

### 2.5.2 LIGO-Virgo results

The collaborative work between LIGO and Virgo on detection methods aimed in the first place at comparing filter performances, to verify the *a priori* equivalence of the tools. This background work provided key figures to establish where EGC stands compared to other filters, for different waveforms. The full set of results will be found in [23], while some values are grouped in table 2.1. ATw, ST and STw were excluded from this study because they were already out-performed by EGC.
While EGC is not the best performing filter for the tested waveforms, it maintains a second to best position for all of them. This regularity is not seen for other methods.
The different sensitivity of the LIGO instruments slightly affects detection performances for identical injected SNR but do not alter the conclusions reached for Virgo.

## 2.6 Conclusion

Successive corrections to simple detection principles permitted to propose the EGC algorithm, a versatile time-frequency method for the extraction of impulsive signals. Performance tests on Gaussian noise indicate a satisfying behaviour compared to several other available algorithms.

| Waveform | EGC | QT | PF | PC |
|---|---|---|---|---|
| a1b2g1 | 5.3 *(2)* | 6.6 | 5.9 | 5.6 |
| a2b4g1 | 6.5 *(2)* | 6.8 | 6.6 | 5.8 |
| Gaussian 1 ms | 5.5 *(2)* | 5.9 | 5.9 | 4.9 |
| Gaussian 4 ms | 5.7 *(2)* | 7.0 | 7.3 | 5.2 |
| Gaussian-cosine (235,5) | 5.5 *(2)* | 5.2 | 6.6 | 6.6 |
| Gaussian-cosine (235,15) | 5.7 *(2)* | 5.1 | 8.9 | - |
| Gaussian-cosine (820,5) | 5.7 *(2)* | 5.1 | 5.7 | - |
| Gaussian-cosine (820,15) | 5.6 *(2)* | 5.3 | 5.7 | - |

**Table 2.1:** Required signal SNR for a detection efficiency of 50 % with a false alarm rate of $10^{-2}$ Hz. Results are provided for several detection methods, from simulations of Virgo-type noise. Efficiency for PC on some Gaussian-cosine waveforms was too low to extract a significant result. The rank of EGC among the presented methods is given *(n)* for each waveform.

The intermediate AT(w) and ST methods may lead to satisfying analysis tools, but much additional work is expected to this end. Forging ahead with EGC appears to be the best choice at the moment.

| Method | DFM a1b2g1 | Gaussian 1ms | Gaussian-cosine 235 Hz Q 5 |
|---|---|---|---|
| ATw | 0.11 (166) | 0.14 (159) | 0.17 (195) |
| ST | 0.08 (122) | 0.83 (178) | 0.21 (186) |
| STw | 0.07 (167) | 0.14 (165) | 0.25 (199) |
| EGC | 0.40 (166) | 0.32 (162) | 0.33 (198) |

**Table 2.2:** Efficiency for the four analysis methods proposed in this work, with a false alarm rate set to 10 mHz and injection SNR to 5. The number of injections is added (n).

The care taken of noise normalization in the context of Virgo data analysis aims at preserving most of the detection efficiency on real data. The characterization of signal time-frequency clusters in frequency, duration and energy hopefully will provide a reference for the study of unknown burst-like structures in the data.
The application of EGC to Virgo commissioning data is developed in Chapter 4.

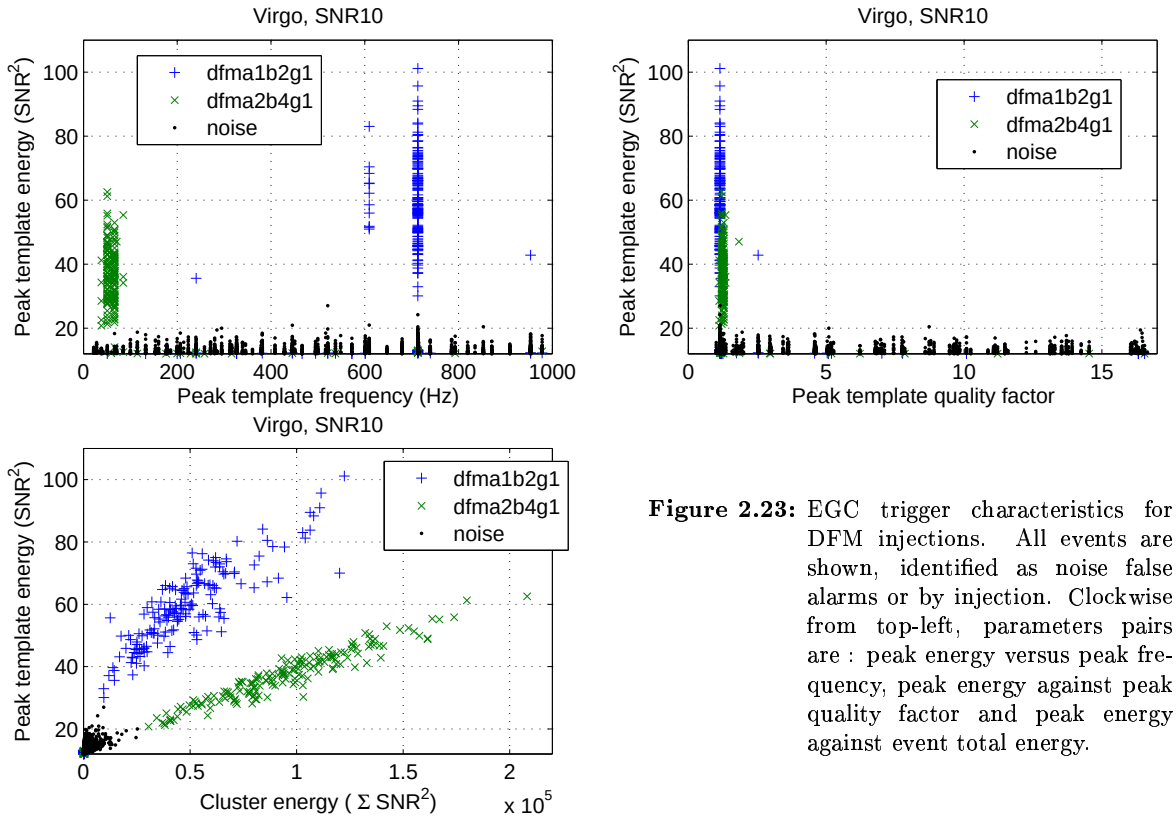


**Figure 2.23:** EGC trigger characteristics for DFM injections. All events are shown, identified as noise false alarms or by injection. Clockwise from top-left, parameters pairs are : peak energy versus peak frequency, peak energy against peak quality factor and peak energy against event total energy.

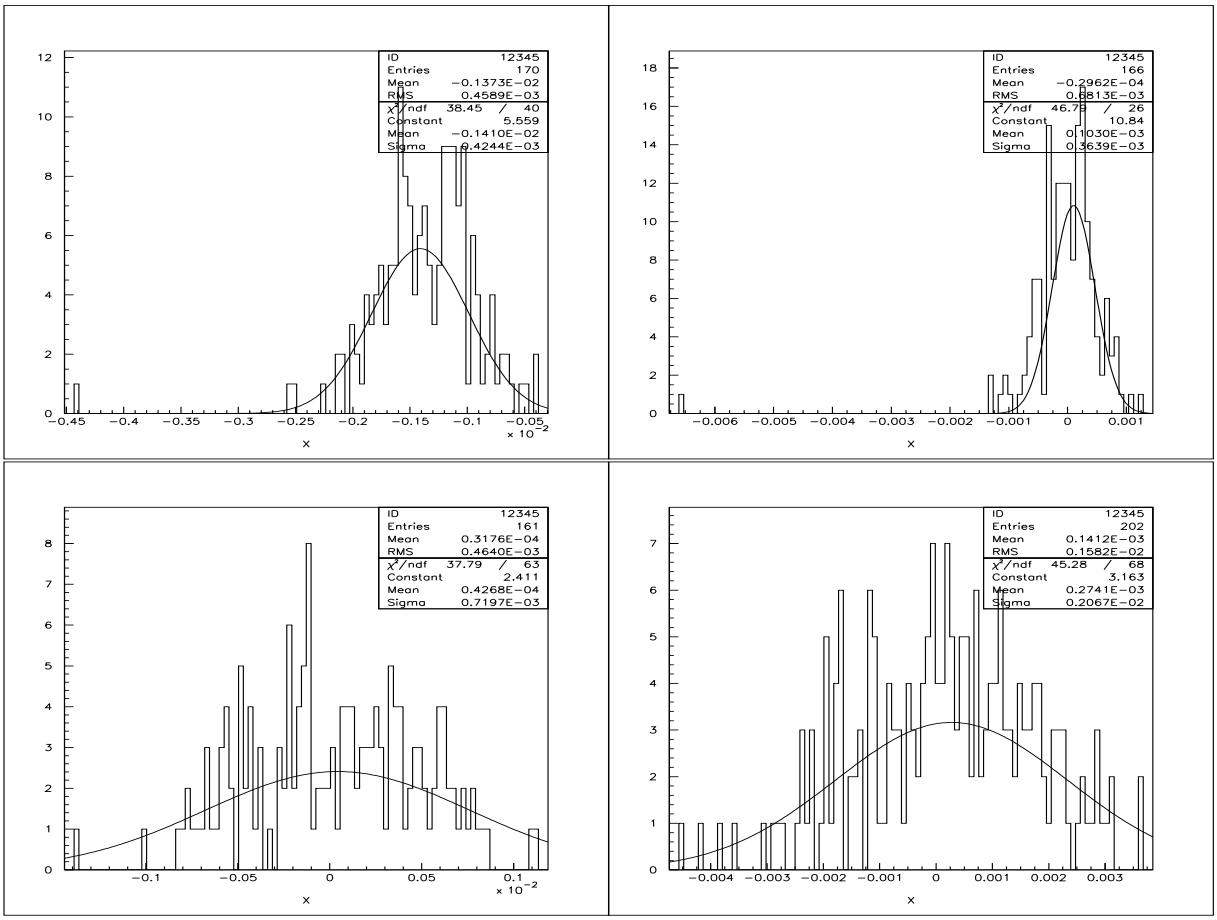


**Figure 2.24:** EGC detection delay histogram and Gaussian fit from detection events on four waveforms. Clockwise from top left : DFM a2b4g1, Gaussian 4 ms, SG Q=15 f=820 and SG Q=15 f=235.

# Bibliography


[1] M. Zanolin *et al*, *LIGO-Virgo analysis group: Burst search*, GWDAW 2004, CQG **S22**, 1381 (2005).

[2] F. Beauville *et al*, *LIGO-Virgo analysis group: Binary coalescence search*, GWDAW 2004, CQG **S22**, 1381 (2005).

[3] A. Papoulis, "Signal analysis" (McGraw-Hill, 1994).

[4] N. Arnaud *et al*, *An elliptical tiling method to generate a two-dimensional set of templates for gravitational wave search*, *Phys. Rev.* D **67**, 102003 (2003).

[5] Y. Tsunesada *et al*, *On detection of black hole quasinormal ringdowns: Detection efficiency and waveform parameter determination in matched filter*, *Phys. Rev.* D **71**, 103005 (2005).

[6] N. Arnaud *et al*, *Detection of gravitational wave bursts by interferometric detectors*, *Phys. Rev.* D **59**, 082002 (1999).

[7] L.A. Wainstein & V.D. Zubakov, "Extraction of signals from noise" (Prentice-Hall, 1962)

[8] N. Arnaud *et al*, *Comparison of filters for detecting gravitational wave bursts in interferometric detectors*, *Phys. Rev.* D **67**, 062004 (2003).

[9] J. Sylvestre, *Time-frequency detection algorithm for gravitational wave bursts*, *Phys. Rev.* D **66**, 102004 (2002).

[10] P. Flandrin, "Temps-fréquence" (Hermès, Paris, 1993).

[11] S. Mallat, "A Wavelet Tour of Signal Processing" (Academic Press, 1999).

[12] P.D. Welch, *The Use of Fast Fourier Transform for the Estimation of Power Spectra: A Method Based on Time Averaging Over Short, Modified Periodograms*, IEEE Transactions on Audio and Electroacoustics **15**, 70 (1967).

[13] M.J. Shensa, *Discrete Wavelet Transforms: Wedding the a trous and Mallat algorithms*, IEEE Transactions on Signal Processing **40**, 2464 (1992).

[14] F. Murtagh *et al*, *Multiresolution in astronomical image processing: a general framework*, Int. J. Imaging Systems and Technology **6**, 332 (1995).

[15] R.C. Pinnegar and L. Mansinha, *Time-local Spectral Analysis for Non-Stationary Time Series: The S-Transform for Noisy Signals*, Fluctuation and Noise Letters **3-3**, 357 (2003).

[16] C.R. Pinnegar and D.W. Eaton, *Application of the S transform to prestack noise attenuation filtering*, Journal of Geophysical Research **108-B9**, 2422 (2003).

[17] J. Hoshen and R. Kopelman, *Percolation and cluster distribution. I. Cluster multiple labeling technique and critical concentration algorithm*, *Phys. Rev.* B **14**, 3438 (1976).

[18] S.L. Finn and S. Mukherjee, *Data conditioning for gravitational wave detectors: A Kalman filter for regressing suspension violin mode*, *Phys. Rev.* D **63**, 062004 (2001).

[19] A.C. Clapson *et al*, *Kalman filter for violin modes suppression*, (Virgo note VIR-NOT-LAL-1390-267, 2004)

[20] S. Klimenko *et al*, *Performance of the WaveBurst algorithm on LIGO data*, *Class. Quant. Grav.* **21**, S1685-S1694 (2004).

[21] G.M. Guidi *et al*, *A power filter for the detection of burst events based on time frequency spectrum estimation*, *Class. Quant. Grav.* **21**, 5 (S815).2004

[22] S. Chatterji *et al*, *Multi-resolution techniques for the detection of gravitational-wave bursts*, *Class. Quant. Grav.* **21**, S1809-S1818 (2004).

[23] M.A. Bizouard *et al*, *Strategy for searching burst gravitational waves with LIGO and Virgo detectors*, in preparation.

# Chapter 3

# A phase-space method for spectral lines removal

## Contents



## 3.1 Introduction

In the predicted noise budget of Virgo, described in Chapter 1, the resonance modes of the wires and mirrors, so-called violin and drum modes, are the main narrow-band features above the broadband smooth spectrum shape. They complicate the whitening of the spectral distribution, an operation described in Annex C, that is mandatory before the application of some burst detection filters, as described in [1]. Correlator-type filters do not require separate whitening, but they are affected by fluctuations in spectral lines amplitude: reference spectra are typically established over long segments of data, resulting in averaged energy spectral densities. Analyzed segments must generally be smaller, for implementation reasons. This results in discrepancies between short-segments spectral densities and reference values, which can become important for large spectral power densities, typically achieved by those modes.

Overall, data analysis would gain from efficient resonance modes suppression. This is the aim of the work described hereafter, that expands on work done within the LIGO collaboration [2].
The central idea, classic in control theory, is to use model-based filtering, here with the equations derived by Kalman [3].

## 3.2 Thermal lines

### 3.2.1 Pendulum model

The physical processes under consideration can be represented with good accuracy using the model of the linear pendulum. The equation of motion for the test mass at the end of a pendulum seen as a damped harmonic oscillator is $m\ddot{x} + b\dot{x} + k(x - x_{init}) = 0$. Its solution is an exponentially-dampened sinusoid, with an impulse response :

$$p(t) = e^{-t/\tau \frac{{f_0}^2}{f_d}} sin(2\pi f_d t) \tag{3.1}$$

where $\tau = \frac{2m}{b}$, $f_0 = \frac{1}{2\pi}\sqrt{\frac{k}{m}}$ and $f_d = f_0\sqrt{1 - \frac{b^2}{4km}}$.

The pendulum model depends in the end on the damping relation. The position-related factor $k$ is analog to a spring recoil, while the velocity-related viscosity term $b$ provides so-called fluid damping.

When excited by a force $u$, the displacement $x$ of a damped oscillator is described by :

$$\begin{aligned} m\ddot{x} + b\dot{x} + kx &= u \\ \text{or} & \\ \ddot{x} + \frac{\omega_0}{Q}\dot{x} + {\omega_0}^2 x &= \frac{u}{m} \end{aligned} \tag{3.2}$$

with $\omega_0 = \sqrt{\frac{k}{m}}$ the proper angular frequency and $Q = \frac{\sqrt{km}}{b}$ the quality factor of the oscillation. The quality factor is in inverse relation with the energy dissipated per oscillation period and therefore to the exponential decay time $\tau$ of the resonance amplitude, by $Q = \omega_0\tau/2$.

### 3.2.2 Violin modes

Violin modes are mechanical resonances of the mirrors' suspension wires. Motion is assumed to occur along one axis only, by considering the departure from the equilibrium position to be small. Using the linear displacement coordinate $x$, with the origin at the equilibrium position, simplifies the equations and is consistent with the motion amplitude of Virgo mirrors.
The model of Section 3.2.1 does not use the actual energy-loss process for a suspension of Virgo. For a system in vacuum, loss will (slowly) happen through internal damping, modeled with :

$$m\ddot{x} + k(1 + i\phi(f))x = 0 \tag{3.3}$$

where the anelasticity is introduced by $\phi(f)$, interpreted as the angle between the direction of the driving force and the response of the spring (through $k$). Viscous damping will however be preferred here for simplicity, since both models predict identical spectral densities $\hat{x}$ around the resonance, where the modes will be above other noise components, as shown in figure 3.1. Losses in both models are related to the loss angle $\phi$, linked to the quality factor by $Q = 1/\phi$ as a first approximation.

A suspension wire can be modeled as a flexible thin bar clamped at both ends. A suspension system experiences tension, from the weight of the suspended mass $m$ as $T = \frac{mg}{n_w}$, with $g$ the gravity acceleration, that can be supposed uniform along the wire and distributed among the eventual $n_w$ wires of the suspension. Wires are also stiff, which explains the energy dissipation through elastic deformation, with a global spring constant $k_{el} = n_w\sqrt{TEI}/2L^2$ depending on wire length $L$ and the moment of inertia $I$ of the wire cross-section. Young's modulus $E$ relates the effective wire deformation with the required constraint through the Hooke law.
Both $E$ and $I$ are empirical characteristics, to be measured.

As detailed in [6], for a wire along the $x$ axis oscillating along the $y$ direction, the equation of motion is :

$$T\frac{\partial^2 y}{\partial x^2} - ES\frac{r_{wire}}{2}\frac{\partial^4 y}{\partial x^4} = \rho_{wire} S\frac{\partial^2 y}{\partial t^2} \tag{3.4}$$

with $r_{wire}$ and $\rho_{wire}$ the radius and density of the bar of cross-section $S$.
Solving equation 3.4 with test mass $m_{mirror}$ and chosen boundary conditions gives a discrete set ($n \in [1, \infty[$) of allowed oscillation frequencies, the resonances of the bar :

$${f_0}^n = n \times \frac{1}{2L}\sqrt{\frac{T}{\rho_{wire} S}}\left(1 + \frac{2}{L}\sqrt{\frac{ES{r_{wire}}^2/4}{T}}\right) \tag{3.5}$$

The quality factor for a given resonance frequency can be estimated from energy loss considerations by :

$$Q(f) = \frac{2mgL}{n_w\sqrt{TEI}}\frac{1}{\phi_0 + \Delta\frac{f/f_r}{1+(f/f_r)^2}} \tag{3.6}$$

This equation replaces the simple relation $Q = 1/\phi$ and highlights frequency-dependent thermoelastic effects in $\phi_{th}(f) = \phi_0 + \Delta\frac{f/f_r}{1+(f/f_r)^2}$. This formula involves material-specific coefficients : the relaxation strength $\Delta = \frac{\alpha^2 E T_K}{c_{th}}$ and the relaxation frequency $f_r \simeq \frac{2.16\kappa}{4{r_{wire}}^2 c_{th}}$, with $\alpha$ the linear expansion coefficient, $c_{th}$ the specific heat, $T_K$ the temperature and $\kappa$ the thermal conductivity of the wire material. The constant loss angle term $\phi_0$, represents losses at the attachment points and must be experimentally estimated. A finer model is proposed in [7], giving :

$${Q^n} = \frac{1}{\phi_{th}({f_0}^n)}\frac{k_e L}{2}\left(1 + \frac{(n\pi)^2}{2k_e L}\right)^{-1} \tag{3.7}$$

for $k_e = \sqrt{T/EI}$.

### 3.2.3 Mirror internal modes

While suspension wires oscillate in response to thermal excitation, the mirrors, also excited, respond in fashion. Important motions concern the reflective surfaces, whose motion affect the measurement. It was shown, see [8] for instance, that mirrors have several eigenmodes that make their surfaces oscillate. Like for violin modes, damping is dominantly by internal friction. A simple model replaces the mirror by a point mass on a spring, as in Section 3.2.1. More physical descriptions, applied to Virgo in [9], consider the number of nodal diameters on the mirror surface and the eventual phase difference between the two sides.
Numerical computations and experimental verifications give for Virgo-type mirrors frequencies above 3.3 kHz for all modes.
All models are compatible with the thermal motion equation of Chapter 1, and therefore the generic parameters detailed above for violin modes, proper frequency, quality factor and (equivalent) mass can be estimated for mirror internal modes. Thus the following work, where physical details are neglected, applies as well to both types of spectral lines.

### 3.2.4 Incidence of thermal noise

Thermal noise excitation is a broadband force, noted $F_{th}$, whose power spectral density is described by the fluctuation-dissipation theorem [4] as white noise. It couples to a pendulum of fluid damping coefficient $b$ with the power spectral density :

$$\hat{F}_{th}^2 = 4k_B T_K b \tag{3.8}$$

where $k_B$ is the Boltzmann constant and $T_K$ the temperature, see [5] for details. The equation of motion for a prototype pendulum, using the parameters introduced above, is then :

$$\ddot{x} + \frac{\omega_0}{Q}\dot{x} + {\omega_0}^2 x = \frac{4k_B T_K}{m_{test}}\frac{\omega_0}{Q} \tag{3.9}$$

The energy stored by the system depends on initial conditions, $x_0$ and $\dot{x}_0$, the damping factor and the external excitation. With a thermal noise excitation, the peak displacement spectral power density is :

$$\hat{x}^2(\omega_0) = \frac{4k_B T_K Q}{m_{test}{\omega_0}^3} \tag{3.10}$$

The spectral sharpness of the resonance is defined by $Q = \frac{\omega_0}{\Delta\omega}$, for $\Delta\omega$ the usual full width at mid-height of the spectral peak. This relation completes the time-domain interpretation of $Q$.

When considering alternative dissipation models, the spectral shape of the oscillation will be different as well. The viscous damping model, those equations are fairly simple, gives an energy spectral density of :

$$\hat{x}^2_{viscous}(f) = \frac{4k_BT}{(2\pi)^3}\frac{f_0}{m_{test}Q}\frac{1}{({f_0}^2 - f^2)^2 + (\frac{f f_0}{Q})^2} \tag{3.11}$$

For the internal damping model, more realistic for systems in vacuum, the energy spectrum is :

$$\hat{x}^2_{internal}(f) = \frac{4k_BT}{(2\pi)^3}\frac{f_0}{m_{test}Qf}\frac{1}{({f_0}^2 - f^2)^2 + (\frac{{f_0}^2}{Q})^2} \tag{3.12}$$

supposing the loss angle is constant $\phi(f) = 1/Q$.

It is clear from the above equations that the details of the dissipation model will not affect narrow lines, where most of the energy is located near the resonance frequency. From equation 3.12, the energy in the tails drops in $f^{-5}$ at high frequency, and varies in $f^{-1}$ toward low frequencies, as visible in figure 3.1. This guarantees that away from the resonance equation 3.11 underestimates the effect of thermal noise.

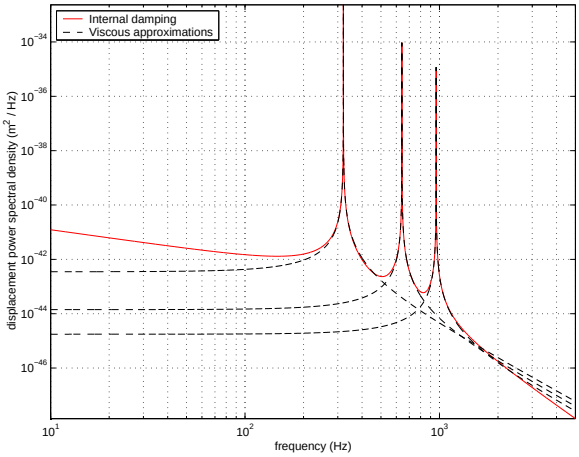


**Figure 3.1:** Comparison of motion spectral signatures, for internal damping and viscous simplification, for parameters compatible with Virgo specifications. Virgo noise background is expected at $\approx 10^{-38}\ m^2/Hz$ around these modes.

### 3.2.5 Noise budget estimation

When considering the noise budget of Virgo, a multiplicative factor of $\frac{1}{L_{arm}}$ must be introduced to scale the power spectral density of a line, derived for mirror motion, to the strain measurement. Besides, the violin modes concern only the suspension wires that maintain the mirror, not the whole seismic isolation chain, hence $L \approx 30$ cm.
The four-wire suspension of a Virgo mirror, once described with the equations introduced above, can be modeled as a generic resonant system, excited by $F_{th}$, with the test mass replaced by a specific [10] equivalent mass $M$ :

$$M^n = n^2 \times \frac{\pi {m_{mirror}}^2}{2\rho_{wire}{r_{wire}}^2 L} \tag{3.13}$$

$$= n^2 m_0 \tag{3.14}$$

$${f_0}^n = n \times \frac{\pi}{L}\sqrt{\frac{m_{mirror}g}{4\pi {r_{wire}}^2\rho_{wire}}}(1 + \frac{2}{Y}) \tag{3.15}$$

$$= nf_0 \tag{3.16}$$

$$Q^n = \frac{Y}{2\phi_{th}({f_0}^n)}\frac{1}{1 + \frac{n^2\pi^2}{2Y}} \tag{3.17}$$

| Violin modes | | |
|---|---|---|
| $f_0$ (Hz) | Q ($10^6$) | M ($10^6$ kg) |
| 320.4 | 0.5 | 11.7 |
| 640.9 | 0.4 | 46.9 |
| 961.3 | 0.4 | 105.6 |
| 1281.7 | 0.5 | 187.7 |
| 1602.2 | 0.5 | 293.2 |
| 1922.6 | 0.6 | 422.2 |
| 2243.1 | 0.7 | 574.7 |
| 2563.5 | 0.8 | 750.6 |
| 2883.9 | 0.9 | 950.0 |
| 3204.4 | 0.9 | 1172.8 |

| Mirror internal modes | | |
|---|---|---|
| $f_0$ (Hz) | Q ($10^6$) | M (kg) |
| 5580.0 | 0.7 | 6.5 |
| 5640.0 | 10.0 | 6.5 |

**Table 3.1:** Predicted values for the main thermal lines. *Left* The violin modes visible in the sensitivity curve. *Right* The main mirror mode, for the two mirror types of the Fabry-Perot cavities.

with $Y = L\sqrt{\frac{m_{mirror}g}{Er_{wire}^2}}$ and $n \geq 1$ the violin mode number in the harmonic series.
All numerical values are available in [10]. The predictably visible violin modes for Virgo are listed in table 3.1. Note that precise values will differ for each wire, owing to small physical differences, thus in practice any predicted line will be divided in four independently excited lines, one for each mirror, and probably sub-divided in 4 very close resonances, one per suspension wire.
The table also includes the parameters for the main internal mirror modes. There are two sets, each concerning two mirrors, although the exact values will again be unique to each mirror.

### 3.2.6 Phase-space formalism

Moving to sampled data, a discrete-time formalism is necessary. It is then possible to define a deterministic system by its state at a given time, plus the rules to compute its state at a following time. The state of the system is the value of all its dynamical variables and relevant parameters at that time. Things are easier if the transition rule is linear with respect to the variables: time update simplifies into an algebraic operation. This explains the preference given to viscous over internal dissipation, whose equations involve complex quantities.

The transformation to a first order system of the pendulum equation 3.2 is straightforward, with the introduction of a second system variable, velocity $\dot{x}$ :

$$\begin{pmatrix} \dot{x}(t) \\ \ddot{x}(t) \end{pmatrix} = \begin{pmatrix} 0 & 1 \\ -{\omega_0}^2 & -\frac{\omega_0}{Q} \end{pmatrix} \cdot \begin{pmatrix} x(t) \\ \dot{x}(t) \end{pmatrix} + \begin{pmatrix} 0 \\ \frac{u}{m} \end{pmatrix} \tag{3.18}$$

The following step is to shift to discrete time, after solving the differential equation. Consider a generalized form of equation 3.18 :

$$\dot{X}(t) = A_c.X(t) + B_c.U(t) \tag{3.19}$$

with $X(t) = \begin{pmatrix} x(t) \\ \dot{x}(t) \end{pmatrix}$, $A_c$ and $B_c$ matrices. $A_c$ describes the physical process, whose state is given by vector $X$ :

$$A_c = \begin{pmatrix} 0 & 1 \\ -{\omega_0}^2 & -\frac{\omega_0}{Q} \end{pmatrix} \tag{3.20}$$

and $B_c$ the intervention of the excitation noise as an acceleration term, identified by vector $U$, through :

$$B_c = \begin{pmatrix} 0 \\ 1 \end{pmatrix} \tag{3.21}$$

The formal solution is :

$$X(t) = \Phi(t, t_0).X(t_0) + \int_{t_0}^{t} \Phi(t, \tau).B_c.U(\tau)d\tau \qquad \text{for } t > t_0 \tag{3.22}$$

with $\Phi(t,t_0) = \int_{t_0}^{t} e^{A_c \tau} d\tau$.
As only the resonant case is of interest, where $\frac{{\omega_0}^2}{Q^2} - 4{\omega_0}^2 < 0$, the integrated process, between $t_0$ and $t = t_0 + T$, is :

$$\Phi(t,t_0) = \Phi(T) = e^{-\frac{\alpha T}{2}} \begin{pmatrix} (\cos\omega T + \frac{\alpha}{2\omega}\sin\omega T) & \frac{1}{\omega}\sin\omega T \\ -\frac{\beta}{\omega}\sin\omega T & (\cos\omega T - \frac{\alpha}{2\omega}\sin\omega T) \end{pmatrix} \tag{3.23}$$

with

$$\begin{cases} \alpha = \frac{\omega_0}{Q} \\ \beta = {\omega_0}^2 \\ 2\omega = \sqrt{|\frac{{\omega_0}^2}{Q^2} - 4{\omega_0}^2|} \end{cases}$$

Finally, discrete-time formulation can be derived by considering only values at $t = jT$, $j \in \mathcal{N}$, $T$ the time step. Assume $U$ to be constant between sampling moments in order to extract it from the integral :

$$X((j+1)T) = \Phi((j+1)T, jT).X(jT) + B((j+1)T, jT).U(jT) \tag{3.24}$$

where

$$\begin{aligned} B((j+1)T, jT) &= \int_{jT}^{(j+1)T} \Phi((j+1)T, \tau).B_c d\tau \\ &= {A_c}^{-1}.(\Phi - I_m).B_c \\ B &= e^{-\frac{\alpha T}{2}} \begin{pmatrix} \frac{1}{\beta} - \frac{1}{\beta}(\alpha\sin\omega T + \cos\omega T) \\ \frac{1}{\omega}\sin\omega T \end{pmatrix} \end{aligned} \tag{3.25}$$

with $I_m$ the identity matrix.
The excitation of the physical model relies on a random (thermal) acceleration, hence $U \in \mathcal{R}$.
This discrete time model of a viscously damped violin mode agrees well with predictions, especially in the frequency band of interest around the resonance, see figure 3.2 for an illustration.

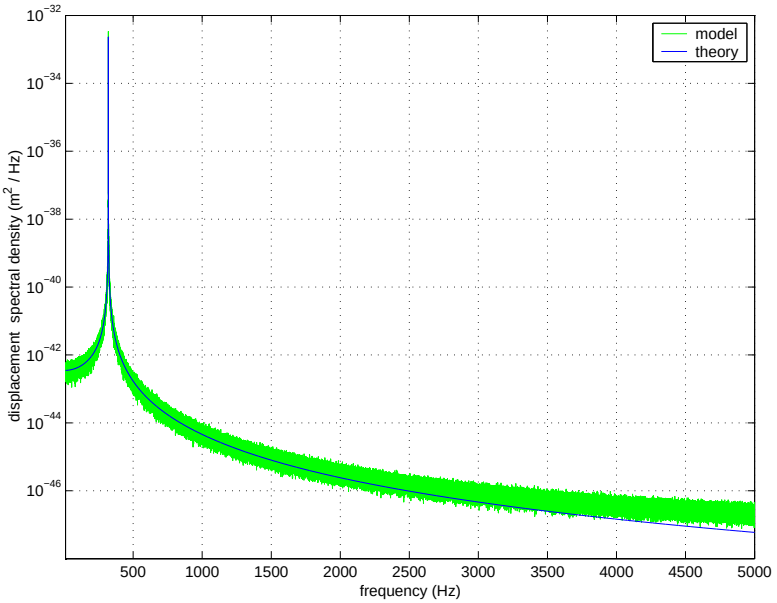


**Figure 3.2:** Spectral comparison of the discrete time domain model with prediction for viscous damping. At the peak frequency, agreement is limited by the PSD resolution, here 0.076 Hz. The remaining discrepancy, generated by PSD estimation bias, is well away from the resonance and below broadband noise level for the instrument. The line parameters correspond to the fundamental violin mode of table 3.1.

## 3.3 Model-based filtering

### 3.3.1 Introduction

Kalman filtering is a model-based time-domain recursive method, developed from the least-square estimation problem (see [11] for an historical perspective on the topic) that describes how to mix the input data and the internal model. The model described above allows the filter to work in the state space, with all the variables required to define the physical system, here position and velocity.
Basically, at each time step, the filter uses the model to guess what the state could be, then compares its prediction to the actual measured variable. This gives an error, also called innovation, used by the filter to correct its guess into an estimation of the current state. Since the considered processes are noisy, another part of each time step is devoted to updating the noise descriptors, though in a measure-independent fashion. This implies that the model provided to the filter must include noise characterization.
The original algorithm [3] was proved to be optimal, in the mean square error sense, for a class of noises including Gaussian white noise. The derivation of its equations is recalled in Annex E. Applying it directly with a colored-type noise would in principle not be correct.
Still, the spectral signature of the model oscillator defined above is very narrow-band, hinting that only the very local noise spectral profile would have any influence. Hopefully the Virgo noise spectral density will be smooth enough to be approximated by a flat distribution around the thermal modes frequencies. Note that this approach is far simpler than in [2], where down-sampling and bandpass filtering are applied prior to the Kalman filter, implying additional calibration and a final up-sampling, with the related numerical issues.

### 3.3.2 Generic equations of the Kalman filter

At the moment only stationary processes are considered. Time dependence is therefore dropped where not required, even though it would be tractable by a Kalman method. The retained form is the *predictor-corrector*, introduced in [3], used to separate the modeled signal (the resonance mode) from noise in the data.

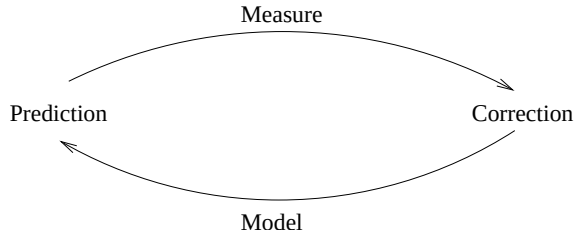


**Figure 3.3:** Schematic Kalman filter loop.

This method deals successfully with any physical process signal $x(t)$, mixed with additive noise in the measured data $y(t)$, provided $t$ is a discrete time index and the physical process producing $x$ (called the plant in control theory) follows a linear recursive update rule :
*Model (the plant)*

$$\begin{pmatrix} x(t) \\ \dot{x}(t) \end{pmatrix} = \Phi \begin{pmatrix} x(t-1) \\ \dot{x}(t-1) \end{pmatrix} + \chi d(t-1) + B n_p(t-1) \qquad \textit{state evolution} \tag{3.26}$$

$$y(t) = Hx(t) + n_m(t) \qquad \textit{observation evolution} \tag{3.27}$$

where the notations of equation 3.24 are kept. $\chi$ is a matrix that projects the deterministic excitation $d$ onto the process state, $n_p$ is the (white) process noise. Most often, only part of the information describing the process is available: $y$ is the observable quantity, the matrix $H$ indicating the projection from $x$ onto $y$. Finally $y$ can be affected by an additional, so called measurement, noise $n_m$.
These noises are represented in the filter by their covariance matrices :

$$R_p = E[n_p.{n_p}^t] \qquad \text{for the process noise term.} \tag{3.28}$$

$$R_m = E[n_m.{n_m}^t] \qquad \text{for the measurement noise.} \tag{3.29}$$

*Kalman processing*

By convention, in this section $\tilde{.}$ indicates prediction of the next time step, $\hat{.}$ estimation of the current state.

The following equations implement the orthogonal projection solution exposed in Annex E. The filter uses its internal model to compute what the next state of the system could be and the uncertainty due to the process and measurement noises.

$$\text{Prediction} \begin{cases} \tilde{x}(t) = \Phi\hat{x}(t-1) + \chi d(t-1) & \textit{state prediction} \\ \tilde{P}(t) = \Phi\hat{P}(t-1)\Phi^t + BR_p(t-1)B^t & \textit{prediction covariance} \end{cases}$$

Then, comparing this prediction to the actual measurement, the filter applies a correction on the state estimation and adjusts the uncertainty related to the measurement noise.

$$\text{Correction} \begin{cases} K(t) = \tilde{P}(t)H^t(t){R_i}^{-1}(t) & \textit{filter gain} \\ \hat{x}(t) = \tilde{x}(t) + K(t)(\overbrace{y(t) - H(t)\tilde{x}(t)}^{innovation}) & \textit{state estimation} \\ \hat{P}(t) = [I_m - K(t).H(t)].\tilde{P}(t) & \textit{correction covariance} \end{cases}$$

with $R_i(t) = H(t)\tilde{P}(t)H^t(t) + R_m(t)$ the innovation covariance matrix.

From these updated values, the filter can compute the next state $\tilde{x}(t+1)$, and so on. At the time first step ($t = 0$), values for $\hat{x}(0)$, the state estimation, and $\hat{P}(0)$, the correction covariance are provided.

The Kalman gain $K$ quantifies the influence of the input measure $y$ on the filter output, but it does not depend at all on the actual measurement. For one-dimensional variables $x$ and $y$, ${R_p} = {\sigma_p}^2$ and ${R_m} = {\sigma_m}^2$. The behaviour of $K$ with respect to the noise parameters can thus be derived :

$$K \propto \frac{{\sigma_p}^2}{{\sigma_m}^2} \tag{3.30}$$

Another form of the same relation goes as follows :

$$\lim_{\|R_m\| \to 0} K = H^{-1} \tag{3.31}$$

$$\lim_{\|\tilde{P}\| \to 0} K = 0 \tag{3.32}$$

There are two separate causes that affect the gain: the relative covariance of the additional noises and the independent characterization of these terms. When $\|R_m\| \to 0$, the noise term disappears, leaving only the process and its own excitation noise, factored by the measurement matrix, while $\|\tilde{P}\| \to 0$ indicates that the state does not vary anymore, thus should not be updated at all. For a low $K$ ($\sigma_p \ll \sigma_m$ or $\|\tilde{P}\| \to 0$), $\hat{x}$ will be close to $\tilde{x}$ as the filter 'trusts' the model. Conversely, high values of $K$ ($\sigma_p \gg \sigma_m$ or $\|\tilde{R_m}\| \to 0$) prompt the filter to follow the input values and disregard its own predictions.

In the original Kalman scheme, $n_p$ and $n_m$ are zero-mean and Gaussian white random sequences.

### 3.3.3 Application to Virgo thermal lines

Given that the Virgo noise is strongly colored, noise parametrization must be refined in order to apply a Kalman filter. Measurement noise is defined by the variance ${\sigma_m}^2$, related to the continuous time Fourier transform of $n_m$ by :

$${\sigma_m}^2 = \langle \widehat{n_m}(\omega)^2 \rangle_\omega \tag{3.33}$$

and to the estimated PSD of data sampled with frequency $\nu_0 = \frac{1}{T}$ by :

$${\sigma_m}^2 = {PSD_m}^2(\omega)\frac{\nu_0}{2} \qquad \text{for a one-sided PSD.} \tag{3.34}$$

The measurement noise parameter must be accurate for the frequency band around the concerned resonance mode, or the filter will not behave properly.

From equation 3.2 and following, the final set of equations is :

$$\Phi = e^{-\frac{\alpha T}{2}} \begin{pmatrix} (\cos\frac{\gamma T}{2} + \frac{\alpha}{\gamma}\sin\frac{\gamma T}{2}) & \frac{2}{\gamma}\sin\frac{\gamma T}{2} \\ -\frac{2\beta}{\gamma}\sin\frac{\gamma T}{2} & (\cos\frac{\gamma T}{2} - \frac{\alpha}{\gamma}\sin\frac{\gamma T}{2}) \end{pmatrix} \tag{3.35}$$

$$B = e^{-\frac{\alpha T}{2}} \begin{pmatrix} \frac{1}{\beta} - \frac{1}{\beta}(\alpha\sin\frac{\gamma T}{2} + \cos\frac{\gamma T}{2}) \\ \frac{2}{\gamma}\sin\frac{\gamma T}{2} \end{pmatrix} \tag{3.36}$$

$$H = \begin{pmatrix} 1 & 0 \end{pmatrix} \tag{3.37}$$

$$\chi = 0 \tag{3.38}$$

$${\sigma_p}^2 = \frac{1}{m^2}\frac{4kT_K m\omega_0}{Q} \tag{3.39}$$

$$R_p = {\sigma_p}^2 \tag{3.40}$$

$$\sigma_m \quad \textit{given by the data} \tag{3.41}$$

$$R_m = {\sigma_m}^2 \tag{3.42}$$

$$G = {\sigma_p}^2\frac{e^{-\alpha T}}{\gamma^2} \begin{pmatrix} \frac{(-\gamma e^{-\frac{\alpha T}{2}} + \gamma\cos\frac{\gamma T}{2} + \alpha\sin\frac{\gamma T}{2})^2}{\beta^2} & \frac{-\alpha+\alpha\cos\gamma T-\gamma\sin\gamma T+2\gamma e^{-\frac{\alpha T}{2}}\sin\frac{\gamma T}{2}}{\beta} \\ \frac{-\alpha+\alpha\cos\gamma T-\gamma\sin\gamma T+2\gamma e^{-\frac{\alpha T}{2}}\sin\frac{\gamma T}{2}}{\beta} & 2(1-\cos\gamma T) \end{pmatrix} \tag{3.43}$$

with $G = B.R_p.B^t$.
For a stationary model, several elements can be computed once for all when setting the filter parameters.
The physical parameters to be initialized before running the algorithm are :

- Pendulum characteristics: Q, $\omega_0$, $m_{eq}$
- Environment description: $T_K$ (*defining* $\sigma_p$), $\sigma_m$
- Initial conditions: $x_0$ (*defining the initial energy*), $\dot{x}_0$

The impact of filter parameters accuracy on filtering efficiency is discussed below.

## 3.4 Performances of static Kalman filter for violin mode removal

The above algorithm can be adapted and used as an estimator, but only for parameters with linear effects; the violin mode characteristics, embedded in matrix $\Phi$, are not accessible in this way. It is therefore necessary to suppose that these parameters remain fixed, and accurate. Discussions on other situations are to be found in the following sections. In order to remain in conditions close to Virgo data, the parameter values of table 3.2 are used in the simulations.

| $\nu_s\ (Hz)$ | $\omega_0\ (Hz)$ | $m_{eq}\ (kg)$ | $Q$ | $T\ (K)$ | $\sigma_p\ (m/\sqrt{Hz})$ | $\sigma_m\ (m/\sqrt{Hz})$ | $x_0\ (m)$ | $\dot{x}_0\ (ms^{-1})$ |
|---|---|---|---|---|---|---|---|---|
| 20000 | 320.44 | $1.17 \times 10^7$ | $5.0 \times 10^5$ | 303.5 | $2.4 \times 10^{-15}$ | $2.2 \times 10^{-23}$ | 0 | 0 |

**Table 3.2:** Reference parameter values used for simulated data. $\nu_s$ is the sampling frequency. Values are for the fundamental mode, as described in [10].

### 3.4.1 Filter response

To demonstrate best case efficiency (referred to below as optimal filtering) in colored noise, the filter was run on data generated using a smooth Virgo PSD, with extra spectral lines, as illustrated in figure 3.4. The filter takes the selected thermal mode out without damaging other features. As the broadband line component is underestimated, this narrow-band filtering behaviour is also seen for mirror modes, even though they affect the PSD over a larger frequency band.

Having verified the initial assumption of tolerance to colored measurement noise, the remaining of the simulations was done in white noise, $\sigma_m = 10^{-20}$, for simplicity reasons.

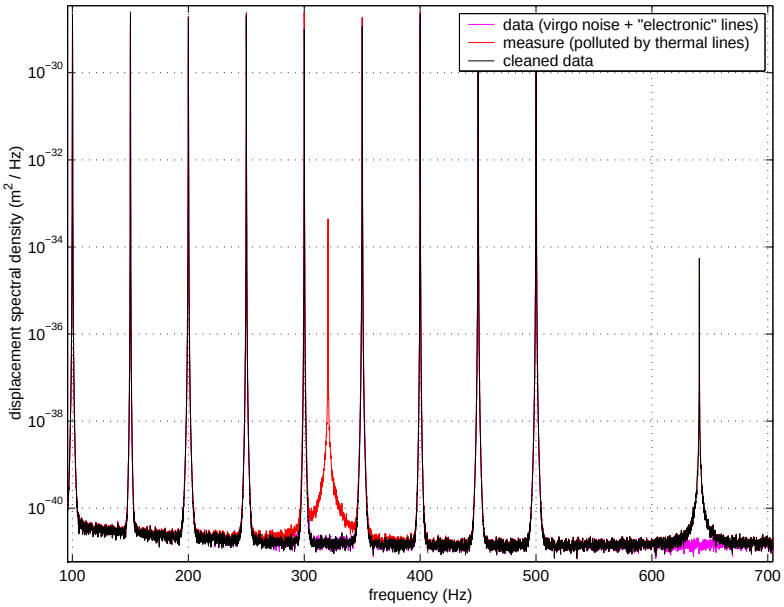


**Figure 3.4:** Violin mode suppression spectra. The input data is Virgo type noise, two thermal lines (320 Hz and 640 Hz) and nine sinusoids (at $k \times 50Hz$), representing electronic lines. The targeted mode (320 Hz) is effectively suppressed while no other spectral feature is altered.

To understand the filter performance, its response to standard input was tested. An impulse signal, see figure 3.5, is eliminated in less than 0.5 s, a desexcitation time depending on the received energy and value of $K$. The behaviour is the same when a Gaussian white noise or Virgo-type measurement noise is added. Note that the pendulum model had a characteristic attenuation time ($\frac{2Q}{\omega_0}$) of roughly 52 s. The large initial value difference between the filter output and the excited pendulum is another effect of the response time of the filter: it doesn't have the time to adjust to the impulse value.

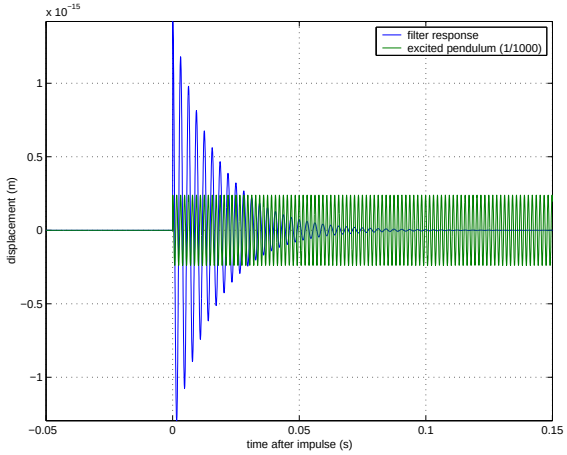


**Figure 3.5:** A single non-zero input displacement value of $2.4 \times 10^{-13}m$ (equal to $100 \times \sigma_m$) was sent at time 0. The filter estimation goes from $1.42 \times 10^{-15}m$ to a numerically zero value after half a second.

### Safe and sound removal

Fed with pure white noise (no component to be extracted) the filter still sees a thermal mode. The PSD is wrongly affected, see figure 3.6. This highlights the effect of a mismatch between the model and the data: the filter 'drills' into the PSD smooth background. However, the energy attributed to the line still comes from the data. Thus the peak power spectral density of the estimated line is at the level of the broadband noise.

It is therefore possible to introduce a safety threshold on the relative energy density in the estimated line $\hat{x}(t)$ and noise. While the noise level is a filter input with $\sigma_m$, the energy of the line can be obtained in the time domain using $Safe = \sigma(\hat{x})$, on short intervals. When the line energy is close to the the background level, the conservative decision is not to remove the estimated line. This time domain computation protects against the suppression of absent lines as illustrated in figure 3.6. It is ineffective when some energy is present above the background level, as it will be integrated in the estimate.

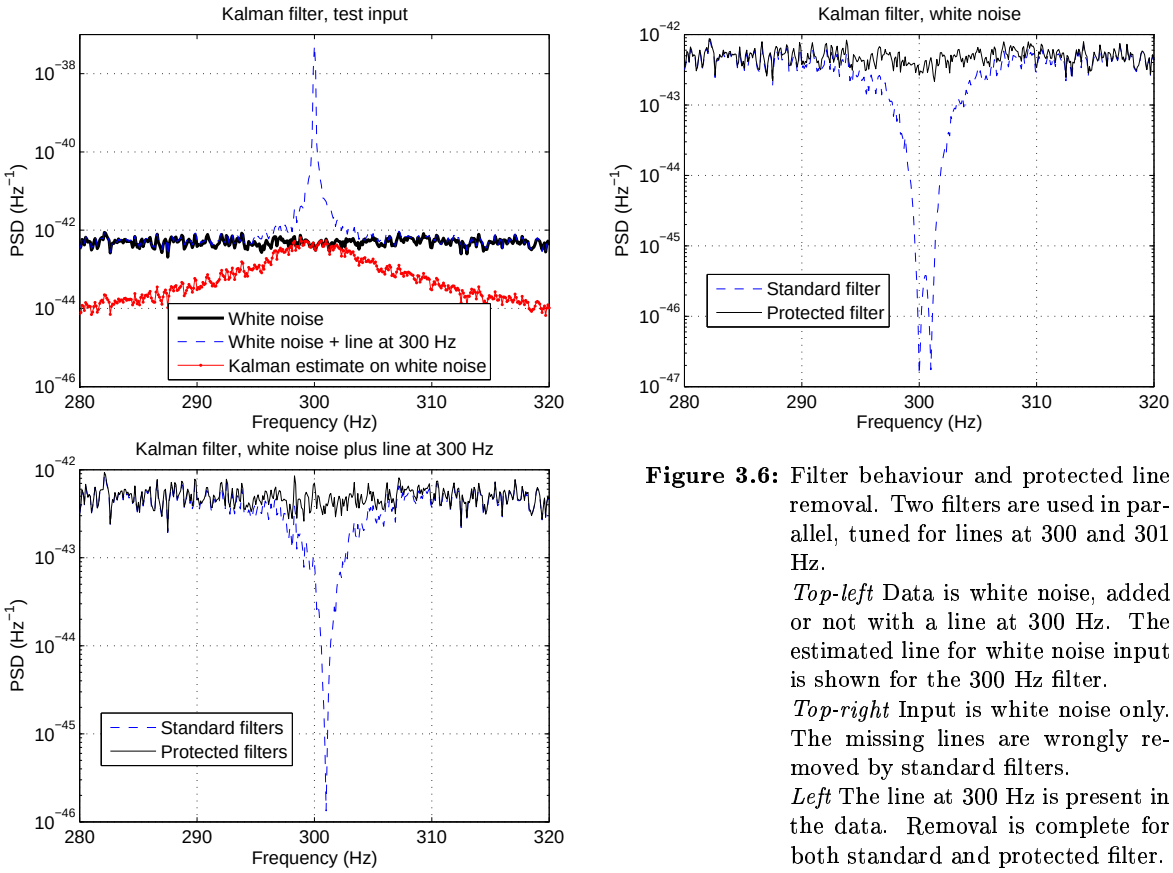


**Figure 3.6:** Filter behaviour and protected line removal. Two filters are used in parallel, tuned for lines at 300 and 301 Hz.
*Top-left* Data is white noise, added or not with a line at 300 Hz. The estimated line for white noise input is shown for the 300 Hz filter.
*Top-right* Input is white noise only. The missing lines are wrongly removed by standard filters.
*Left* The line at 300 Hz is present in the data. Removal is complete for both standard and protected filter.

To complement this 'safe removal' criterion, the same quantity can be computed after the removal step. If a properly modeled line was present and suppressed, the new quantity $Sound = \sigma(x + n - \hat{x})$ should give values compatible both with the absence of line and a background noise at the same level as before. In case of incorrect removal, low $Sound$ values would suggest a hole in the PSD while high values would hint of large residuals. For better performances, a model with a high quality factor and a low mass seems adapted, as it will only sample a narrow frequency region.
This test requires the application of a second filter, hence an additional cost, but it could replace frequency domain checks of the 'drilling effect'.

### 3.4.2 Waveform alteration

Data whitening is most important for some of the burst search algorithms, that suffer from colored noise. The distortion left on typical burst waveforms, after applying the line-removal filter, was checked. As seen in figure 3.7, a residual line, due to the incomplete removal, is added to the signal waveform.
The filter residual (a mostly sinusoidal wave) does not hide the main burst features but blurs its overall shape. Comparison to non-filtered case requires an estimation of the SNR loss, via Monte-Carlo simulations.

Using match filtering on three different waveforms, the SNR loss due to the line residual was estimated. Results are detailed in table 3.3. Reconstructed SNR are easily compatible given the standard deviation. Timing accuracy is limited by sampling and not affected by the processing. As expected, match filter is very robust to colored noise, as long as the given PSD is accurate.

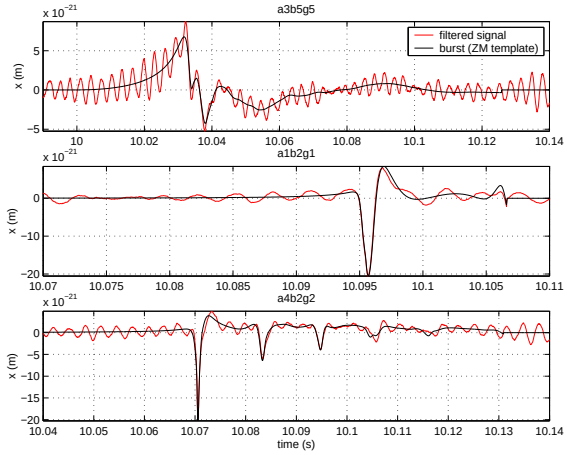


**Figure 3.7:** Time domain residual after line removal : input signal minus Kalman mode estimate, minus the input broadband noise. All filter parameters were optimal. The input was white noise plus a thermal line at 320 Hz, plus a burst waveform ( from the Zwerger & Müller catalog ) injected with a SNR of 10.

| DFM a2b4g1 | | |
|---|---|---|
| Noise type | SNR (std) | Delay (std) $10^{-4}s$ |
| Virgo-type | 9.74 (1.01) | 0.03 (1.1) |
| Plus violin modes | 9.73 (1.01) | -0.02 (1.1) |
| With Kalman filter | 9.72 (1.00) | 0.03 (1.1) |
| CG 235Hz 5 | | |
| Noise type | SNR (std) | Delay (std) $10^{-4}s$ |
| Virgo-type | 9.74 (1.00) | 0.22 (4.4) |
| Plus violin modes | 9.73 (0.99) | 0.24 (4.5) |
| With Kalman filter | 9.71 (1.00) | 0.37 (4.6) |
| G 1ms | | |
| Noise type | SNR (std) | Delay (std) $10^{-4}s$ |
| Virgo-type | 9.77 (1.01) | 0.2 (1.1) |
| Plus violin modes | 9.75 (1.00) | 0.2 (1.0) |
| With Kalman filter | 9.75 (1.01) | 0.2 (1.1) |

**Table 3.3:** The table illustrates the small variation in match filtering output. The waveforms were injected with SNR 10 in colored noise. Each value is averaged over 10000 realizations.

The reconstructed SNR decreases slightly where Kalman filtering was applied : the injected signal itself is affected, if marginally, by the process.

The SNR loss differs with the waveform, it is greater for shorter signals. However, the loss is always a fraction only of the SNR variance. This variance remained constant for increasing numbers of injections, so its meaning is not purely statistical.

### 3.4.3 Pre-processing pipeline

In order to quantify the interest of a line removal step for burst detection, data is simulated with the broadband Virgo spectrum and lines added using the parameters indicated in table 3.1. ROC curves are then computed for waveform DFM a1b2g1, using the MF filter, that requires a whitening pre-processing step. The objective is the comparison of ROCs when a well-tuned line-removal step is applied before whitening, for the same number of coefficients in the AR model. As spectral line AR models require many parameters, the overall quality of the whitened data is affected. And so are MF performances, as shown in [1]. The whitening algorithm is outlined in Annex C.

Results are grouped in table 3.4. Overall, spectral lines have a clear negative effect on the detection performances of MF, whereas applying a well-tuned line removal step does not alter detection performances, which is consistent with the small effect obtained with match filtering. Besides,

for a smooth spectral density, there does not seem to be any interest in increasing the number of whitening parameters. The irregular behaviour at false alarm rate $10^{-4}$ Hz can reasonably be affected to statistical error due to the small event population. Similarly, best results at false alarm rate $10^{-4}$ Hz require less parameters when lines are present due to the higher tolerance to noise events.
Real spectral densities are not expected to be as clean as here, so reducing further the number of AR parameters does not present a strong interest.
The potential gain, under these favorable conditions, is a reduction of a factor 10 in the complexity of the whitening step, without loss of detection performances. This is a computing time gain of the same order, compounded by the cost of the line removal process.

Table 3.5 shows that the part of computing time devoted to line removal is of the order of whitening with 100 parameters. Since the computing load for line removal is constant, this share decreases when the whitening step becomes heavier. As a rule of thumb, for 1000 parameters, the time devoted to pre-process the data is of the order of half the duration of the data segment, and reaches this value for 2000 parameters. These values are obviously to some extent machine-dependent, and likely to improve with computer performances. For instrumental data the requirements may exceed 3000 parameters for some detection filters.

## 3.5 Robustness to parameter error

As the proposed implementation supposes static parameters, it does not allow for model parameters to be tuned on-fly by the Kalman filter. The effect of parameter mismatch on efficiency is all the more critical. This is investigated here.
Estimating the efficiency of a Kalman filter cannot be done independently of its details. Standard tests [12] take advantage of the expected whiteness of the filter internal variables, in a white noise case. These are very useful to verify model design, but were not found to be meaningful for performance studies in this specific case.

A Kalman filter having the same parameter values, hence the same process matrix, as the thermal violin mode generator is considered as an optimal filter. Introducing parameter mismatch then allows performance analysis of suboptimal filters.

All data components are additive and separately generated, using noise routines for the data $s(t)$ and equation 3.24 for violin mode $v(t)$. The cleaned data $s_{Kalman}(t)$ is directly obtained from the estimated line $v_{Kalman}(t)$ *via* $s_{Kalman}(t) = s(t)+v(t)-v_{Kalman}(t)$. Thus reconstruction quality can be quantified using, in the frequency domain, the difference between the PSD of the original signal and that of the reconstructed sequence $s_{\hat{Kalman}}(\omega)$, after subtraction of the estimated violin mode $v_{\hat{Kalman}}(\omega)$, and in the time domain the normalized maximal line reconstruction error :

$$\epsilon = \langle | \frac{(\widehat{s} - \widehat{s}_{Kalman})^2}{\widehat{s}^2} | \rangle_{\omega} \qquad \text{this is a frequency-wise average.} \tag{3.44}$$

$$err_{max} = \langle \frac{max_t(|v_{Kalman} - v|)}{max_t(|v|)} \rangle \qquad \text{this is a time-wise average.} \tag{3.45}$$

From equation 3.44, choosing the frequency range when averaging, two quantities can be obtained alternatively: mode suppression $\epsilon_{mode}$, for $\nu \in [\nu_0 - \Delta\nu, \nu_0 + \Delta\nu]$, or broadband alteration $\epsilon_{bb}$ ($\nu \notin [\nu_0 - \Delta\nu, \nu_0 + \Delta\nu]$). An arbitrary conservative half-width $\Delta\nu = 40$ Hz for the mode band was used.

The first caveat, from the values of $\epsilon_{mode}$, is that mode removal is not complete. Even the optimal filter does not completely suppress the thermal line, as already seen in figure 3.3. The improvement is still very interesting, with a reduction factor of the order of $2 \times 10^5$ on $\epsilon_{mode}$ between filtered and input data. The effect of this residual on the detectability of low SNR short signals was discussed in Section 3.4.2.
Summary results are grouped in table 3.6, while the full study is shown in the figures indicated below.

| Detection efficiency | | according to noise type | | |
|---|---|---|---|---|
| FA rate (Hz) | Burg parameter number | With violin modes | Lines removed | No line |
| $10^{-1}$ | 100 | 0.69 | **0.94** | **0.95** |
| | 200 | 0.80 | 0.93 | 0.94 |
| | 300 | 0.86 | 0.94 | 0.94 |
| | 400 | 0.89 | 0.93 | 0.94 |
| | 500 | 0.89 | 0.94 | 0.94 |
| | 1000 | 0.92 | 0.93 | 0.94 |
| | 1500 | **0.93** | 0.94 | 0.94 |
| | 2000 | 0.93 | 0.94 | 0.94 |
| | 2500 | 0.93 | 0.94 | 0.94 |
| | 3000 | 0.93 | 0.94 | 0.94 |
| $10^{-2}$ | 100 | 0.46 | **0.85** | **0.86** |
| | 200 | 0.62 | 0.83 | 0.83 |
| | 300 | 0.69 | 0.84 | 0.85 |
| | 400 | 0.74 | 0.84 | 0.84 |
| | 500 | 0.75 | 0.84 | 0.85 |
| | 1000 | 0.80 | 0.83 | 0.85 |
| | 1500 | 0.82 | 0.84 | 0.84 |
| | 2000 | 0.82 | 0.83 | 0.84 |
| | 2500 | 0.82 | 0.83 | 0.84 |
| | 3000 | **0.83** | 0.83 | 0.85 |
| $10^{-3}$ | 100 | 0.28 | **0.71** | **0.73** |
| | 200 | 0.42 | 0.67 | 0.69 |
| | 300 | 0.51 | 0.68 | 0.70 |
| | 400 | 0.55 | 0.69 | 0.70 |
| | 500 | 0.58 | 0.69 | 0.70 |
| | 1000 | 0.63 | 0.67 | 0.70 |
| | 1500 | 0.65 | 0.68 | 0.70 |
| | 2000 | 0.65 | 0.69 | 0.69 |
| | 2500 | 0.66 | 0.67 | 0.69 |
| | 3000 | **0.68** | 0.66 | 0.69 |
| $10^{-4}$ | 100 | 0.16 | **0.57** | 0.56 |
| | 200 | 0.28 | 0.54 | 0.56 |
| | 300 | 0.32 | 0.53 | 0.56 |
| | 400 | 0.40 | 0.46 | **0.58** |
| | 500 | 0.45 | 0.54 | 0.54 |
| | 1000 | 0.35 | 0.48 | 0.53 |
| | 1500 | 0.45 | 0.53 | 0.50 |
| | 2000 | 0.50 | 0.46 | 0.46 |
| | 2500 | 0.50 | 0.51 | 0.48 |
| | 3000 | **0.51** | 0.51 | 0.48 |

**Table 3.4:** Mean Filter efficiency fraction. Effect of data pre-processing on the performances. For the chosen waveform (DFM a1b2g1 at SNR 10), the detection efficiency of the filter is given for several false alarm rates, according to the number of parameters allowed to the whitening algorithm. The noise contained violin modes removed or not using optimal Kalman filters. The performance reference is given by results for a noise without lines. Results obtained from 10 hours of data, containing the 10 violin modes of table 3.1, and more than 68000 injections.

| Burg parameter number | 100 | 200 | 300 | 400 | 500 | 1000 | 1500 | 2000 | 2500 | 3000 |
|---|---|---|---|---|---|---|---|---|---|---|
| Kalman to whitening duration ratio | 1.27 | 0.67 | 0.45 | 0.20 | 0.17 | 0.08 | 0.05 | 0.05 | 0.04 | 0.04 |

**Table 3.5:** Pre-processing time sharing. For each configuration is indicated the ratio of processing time spent in the line removal step with respect to the whitening one. Results are from 1 hour of data and 10 violin modes treated.

| Tested parameter | Deviation | $\epsilon_{mode}$ | $\epsilon_{bb}$ | $err_{max}$ |
|---|---|---|---|---|
| $T_K$ (K) | -10% | +10% | -2% | -0.5% |
| | -7% | +5% | -1.5% | -0.5% |
| | 20% | +4% | +5% | +1% |
| | 27% | +10% | +6.5% | +1.5% |
| $\sigma_m$ $(m/\sqrt{Hz})$ | -11% | +11% | +6% | 1.4% |
| | -9% | +5.5% | +5% | +1% |
| | +5% | 7% | -2% | -0.5% |
| | +7% | 13% | -2.7% | -0.5% |
| $Q$ | -20% | 14% | -0.05% | 4.4% |
| | -11% | 2% | -0.03% | 2% |
| | 12% | 10% | 0.03% | -1.6% |
| | 26% | 30% | 0.05% | -3.6% |

**Table 3.6:** Optimal and suboptimal filters comparison, for white broadband noise. Other parameters remain fixed at their optimal value. Each value is a an average of 10 results obtained from PSD estimated on 13 seconds of data and smoothed over 20 runs. One way or another, around 40 minutes of data were used for each case.

### 3.5.1 Environment parameters

Environment descriptors, temperature $T_K$ and measurement noise variance $\sigma_m$, are first considered, as the filter parameters most likely to drift in time.

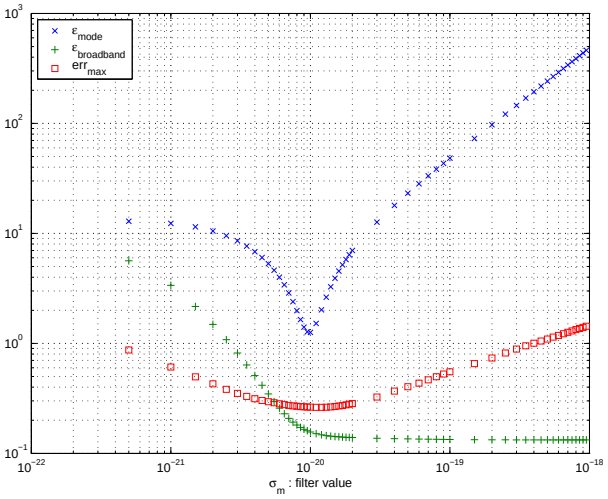


**Figure 3.8:** Filtering error estimators for a mismatch on $\sigma_m$. All other filter parameters are optimal. Note that broadband alteration is limited when $\sigma^{filter}{}_m \geq \sigma^{data}{}_m$, making it a preferred case. Values obtained from 40 minutes of data (white noise background).

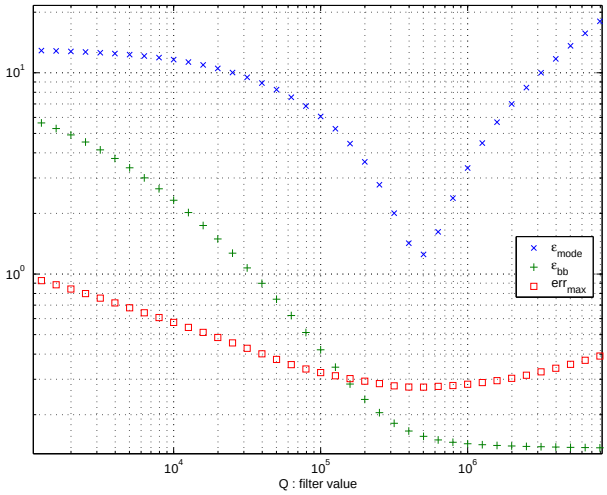


**Figure 3.9:** Filtering error estimators for a mismatch on Q. All other filter parameters are optimal. There is a range around the optimal value where mode suppression is stable, but effects on broadband alteration worsen faster. Values obtained from 40 minutes of data (white noise background).

In the explored range $\delta T_{K\,filter}$ affects (at 5%) both the mode suppression and the broadband component, for mismatches over +30% (the lower limit was not in the explored range). This still leaves a range of more than 50 K around the actual temperature where little mismatch effect is expected, much larger than experienced by the instrument.
The error on $\sigma_m$ (see also figure 3.8) has a stronger effect. There is a [-10% +5%] preferred band around optimal value for peak resorbtion, while broadband alteration is less sensitive to overestimation, and overall error does not vary much. Overestimation is to be preferred, in relation to the evolution of $K$: the filter doesn't take into account measurement noise with a large variance, thus does not alter its broadband part.

### 3.5.2 Line parameters

Quality factor mismatch seems (figure 3.9) to affect filter performances in the same way as $\delta\sigma_m$. The acceptable range value is also similar: $\pm 20\%$ seems a reasonable maximum drift, for the tested configuration.
No measurable effect in the steady state performance was found due to initial energy mismatch ($x_0{}^{filter} \neq x_0{}^{data}$) in a range $[10^{-22}, 10^{-18}]$. This could be explained by the adequacy of all other parameters in the test, that gives sufficient weight to the *innovation* term.
The effect of an equivalent mass ($m_{eq}$) error is similar to that of $\frac{1}{T_K}$, see equations 3.11 and 3.39, with $m_{eq} \gg T_K$, implying a greater impact for the same relative error. Yet it seems reasonable to consider $m_{eq}$ as a static parameter, to be adjusted once for all to experimental values. Therefore it was not specifically explored here.

The most tuning-sensitive parameter is by far the resonant frequency $\omega_0$ (see figure 3.10). For an absolute mismatch of $-0.05$ Hz, $\epsilon_{mode}$ grows by 60%, and 200% for +0.05 Hz. This is in agreement with the narrowness of the violin modes, that allowed us to use a simple filter, but with a price in robustness.

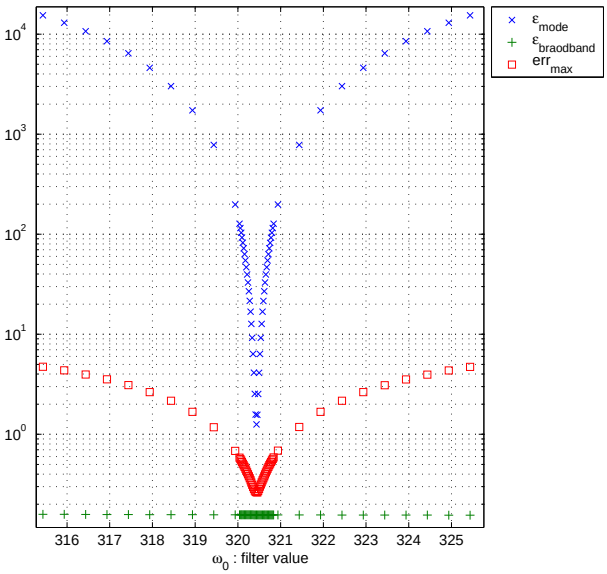


**Figure 3.10:** Filtering error estimators for a mismatch on the resonant frequency. All other filter parameters are optimal. This parameter is very sensitive to mismatch, but the broadband part is not affected. Values obtained from 40 minutes of data (white noise background).

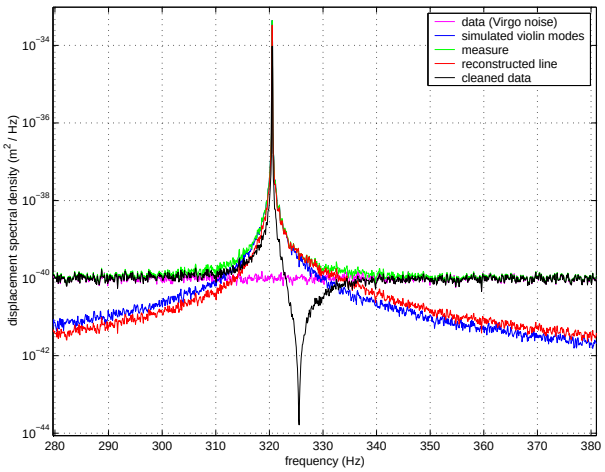


**Figure 3.11:** Resonance frequency mismatch : spectrum with a double peak structure. The model frequency is 5Hz above that of the simulated data. All other filter parameters are optimal. This double peak might be used as a frequency mismatch test.

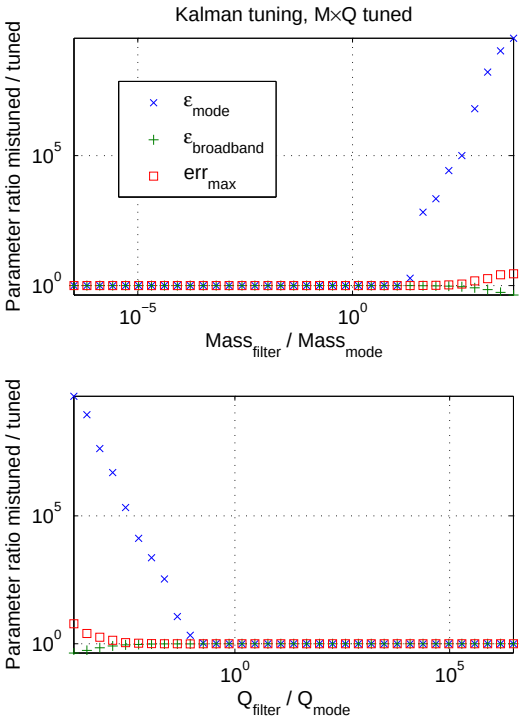


**Figure 3.12:** Filtering error estimators for a mismatch on either mass or quality factor, while keeping the product $M \times Q$ constant. All other filter parameters were are optimal. Values obtained from 40 minutes of data (colored noise background).

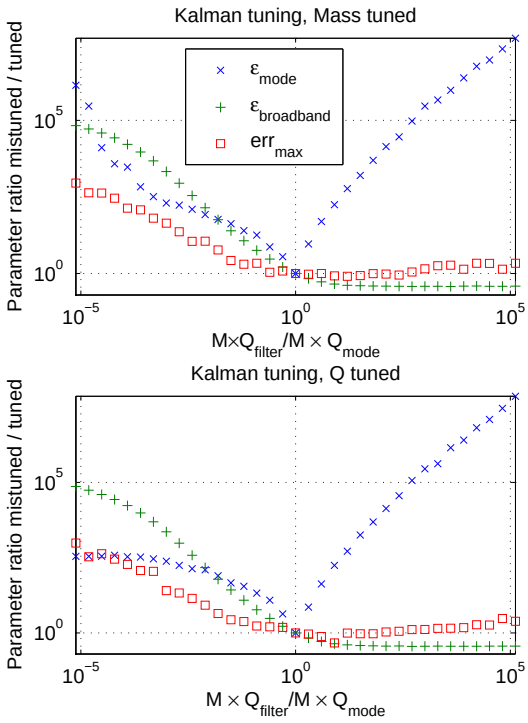


**Figure 3.13:** Filtering error estimators for a mismatch on the product $M \times Q$, while keeping either mass or quality factor constant. All other filter parameters were are optimal. Values obtained from 40 minutes of data (colored noise background).

### 3.5.3 Coupling between line parameters

From equation 3.11, it is clear that the product $\Pi = m_{eq} \times Q$ and $Q$ are effective profile descriptors, indicating for the former the line height, for the second its frequency width. The importance of the accuracy of $\Pi$ is apparent from tests. First, keeping $m_{eq} \times Q$ at the correct value while mis-tuning either $m_{eq}$ or $Q$, as done to produce figure 3.12, does not produce the same error as seen above when $m_{eq}$ or $Q$ was changed while the other remained fixed. Conversely, a correct value for either $m_{eq}$ or $Q$ is not satisfying when $\Pi$ is not correct, as shown in figure 3.13 for the fundamental violin mode. As expected, the same effect was found for lines at higher frequency.

These are indications of what coefficients should be tuned in priority.

## 3.6 Tuning

Since the filter is not very robust to parameter mismatch, its interest depends on the possibility to efficiently find the correct values for the parameters when dealing with real Virgo data.
In real conditions, where no reference signal is available, the performance estimators used in Section 3.5 cannot be calculated.
The filter equations of Section 3.3.3 show that some parameters are coupled in their effect on the filter setup. Hence is it not necessary to tune all the parameters. It should be sufficient to adjust the line frequency, using a corrected parabolic interpolation, described in Annex A, and the covariance of the measurement noise. The value of $\Pi$ would give the quality factor if the mass is considered correct and static. Yet the mass affects the line height like the squared inverse of the measurement coefficient. Data calibration suggests that this coefficient may vary. Unless the line removal adjusts using calibration information, is seems realistic to accept variations of the mass.
Some investigations on time-domain parameters were carried out without much success. They are covered in Annex E.2.

### 3.6.1 Spectral steady state indicators

The idea is to recover parameter values from PSD computed from the data or the filter output. Environment parameters could be recovered from the PSD of the input signal averaged on spectral narrow bands framing the mode peak, $T_K$ using equation 3.10 for peak value measured with a high spectral resolution, or maybe more accurately through environmental monitoring of the instrument. These would be only approximate values. The constraint on $T_K$ could be comfortably set at 10% accuracy, so it does not seem necessary to track it.
For $\sigma_m$, averaged PSD give reliable values. A robust method proceeds by smoothing the PSD, then interpolating a flat background from values at frequencies away from the line peak. The issue could be the characteristic time of the noise evolution.
As observed on real data, spectral lines may move in frequency with time. The physics of violin modes does not easily allow for such wandering, except for the effect of temperature variations on the properties of the material. In any case, filter resonant frequency mismatch is graphically easy to spot in the spectral domain, as shown in figure 3.11.
Automatic detection of the double peak feature could trigger a frequency re-estimation step. This *ad hoc* solution would be favorably replaced by an accurate line tracking algorithm. This is a separate issue, not explored here.
The problems of line estimation, tracking and removal have generated much work in the Virgo collaboration, see for instance [13] and the on-line tool [14].

This spectral method is less reliable when applied on shorter duration data segments, as the variance of the PSD increases. However strong line features are easily separable even in noisy spectra, probably allowing coarse estimations.

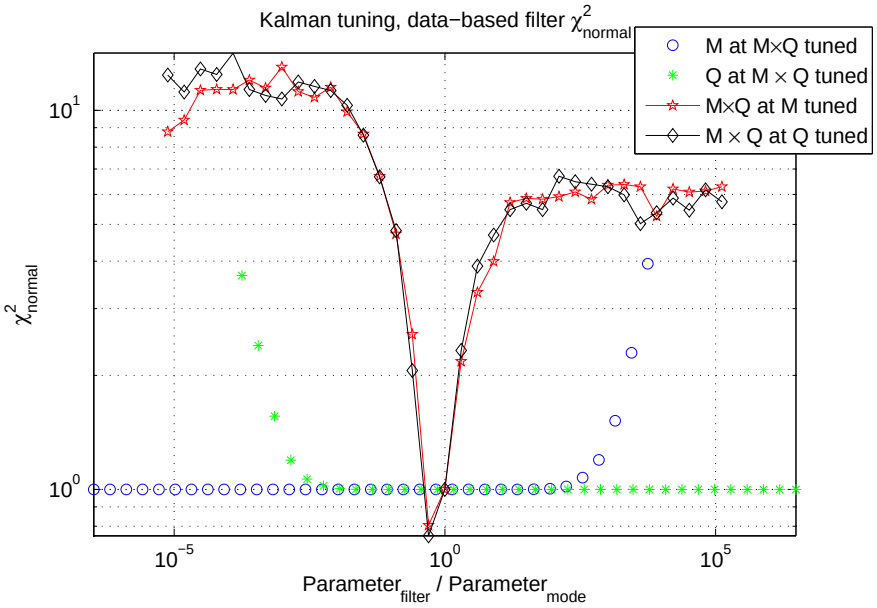


**Figure 3.14:** Filtering data-based estimator. The four cases presented in Section 3.5.3 are presented. Values obtained from 40 minutes of data (colored noise background).

#### Filter mismatch estimator

Since the power spectral density of a line can be computed directly from its parameters, using for instance equation 3.11, it is possible to compare the observed line profile in $PSD_{data}$ with the current filter model $PSD_{model}$, in the frequency range around the resonance frequency.
This comparison is based on the $\chi^2$ quantity, with a bin-specific variance that gives an equal weight to all bins, independently of the line height. It is defined using the quantities :

$$\chi^2{}_{normal} = \frac{1}{N_{line}} \sum_{line} \left(\frac{PSD_{data}(\omega) - PSD_{model}(\omega)}{PSD_{data}(\omega) + PSD_{model}(\omega)}\right)^2 \tag{3.46}$$

$$neg = \sum_{line} \frac{PSD_{data}(\omega) - PSD_{model}(\omega)}{PSD_{data}(\omega) + PSD_{model}(\omega)} \tag{3.47}$$

The returned value is ${\chi^2}_{normal}$, except when $neg < 0$ : then ${\chi^2}_{normal}$ is multiplied by 2. This penalty corresponds to the preference given to insufficient line removal, where $PSD_{model}$ is overall inferior to $PSD_{data}$, over alteration of the background noise by excessive line removal.

As shown is figure 3.14, the behaviour obtained for ${\chi^2}_{normal}$ reproduces the mismatch quantification obtained in Section 3.5 where all the information (background noise and injected line time series) was available for the same parameter sets. The same extremal value of ${\chi^2}_{normal}$ is reached close to the tuning point both for the fundamental violin mode and the first harmonic, although the second is less visible above the noise background. The error on the minimum is at most the width of the sample grid, here a factor 0.5 below the correct value. This validates the estimator for tuning purposes.

### Tuning strategy

More robust indicators of accurate filter tuning could be derived by comparing the output of several filters. The objective is to track some quantity that would reach an extreme when the filter is correctly tuned. Note that this approach cannot correct for data description errors, that command the behaviour of the filter. Measurement noise covariance is obtained as described above, and the temperature is fixed to a reasonable value.

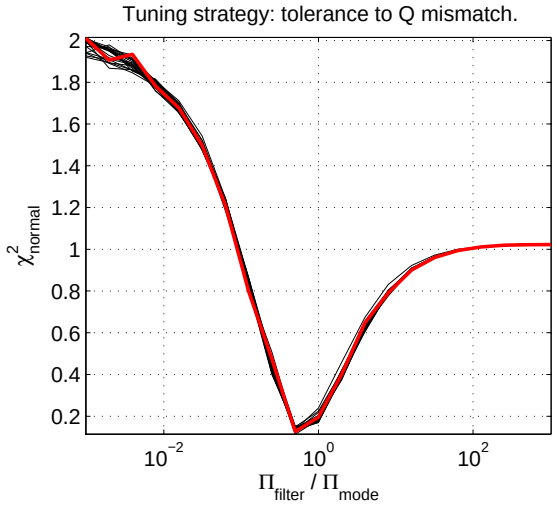


**Figure 3.15:** Robustness of the tuning strategy. The quality factor ranges from $Q_{mode}/2^{10}$ to $Q_{mode} \times 2^{10}$ by factors of 2. The red curve is for $Q_{filter} = Q_{mode}$. Results obtained for the fundamental mode, on 40 minutes of data (colored noise background).

From the results presented here, given a violin mode, or any line that could be modeled similarly, clearly visible in the PSD, with precise conditions yet to be quantified, it is possible to extract separately all the required parameters, using different methods :

- Measurement noise covariance by linear interpolation.
- Line frequency by parabolic interpolation.
- $\Pi$ by minimization of ${\chi^2}_{normal}$, using the golden ratio [15] bisection algorithm [1], at set Q value.
- Quality factor inequality check on ${\chi^2}_{normal}$, at set $\Pi$ value.

It is not critical to have a correct estimation of Q to properly recover $M \times Q$. Figure 3.15 shows that within a range $Q_{mode} \times [10^{-3}, 10^{3}]$, the minimum of ${\chi^2}_{normal}$ when varying $\Pi$ is the same. The quality factor adjustment will not be very accurate, as seen from the small variation of ${\chi^2}_{normal}$ for $Q_{filter} > 10^{-2} Q_{mode}$. This should not be damaging, given the similarly small increment on $\epsilon_{mode}$, $\epsilon_{broadband}$ and $err_{max}$.

[1] Since the explored feature is very narrow, it seemed prudent to prefer a robust, if slow, search algorithm.

### 3.6.2 Tuning accuracy limitation

As the proposed tuning algorithm relies on the spectral shape of the lines, estimated in the PSD, the accuracy of the parameter estimation depends on the resolution of the PSD.

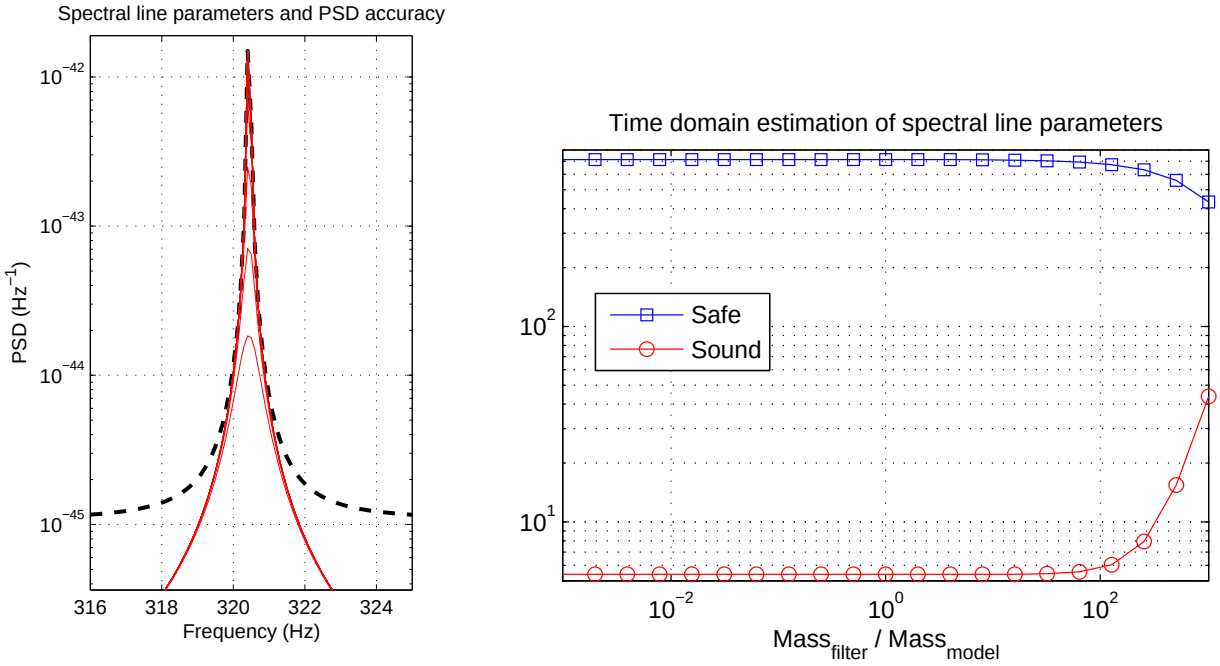


**Figure 3.16:** Resolution and permitted parameter mismatch for a mismatch on mass, while keeping the product $M \times Q$ constant and optimal. All other filter parameters are optimal.
*Left* PSD confusion for line models for M below 100 × $M_{model}$.
*Right* Safe and sound filtering. Time domain filtering error estimators.
Values obtained from 100 seconds of data and a resolution of 0.1 Hz (colored noise background).

For instance, if the quality factor was obtained using $Q = \frac{f_0}{\delta f_{FWMH}}$, the limit $\delta f \geq \delta f_{PSD}$ would make it impossible to measure quality factor above $Q_{lim} = \frac{f_0}{\delta f_{PSD}}$, a very low value for the PSD resolution evoked so far of 0.1 or 0.01 Hz. This may explain the flat allure in figure 3.14 of the $\chi^2{}_{normal}$ when Π is correct but Q is far too high, or M too low, which makes for a very high (in part from the $\frac{1}{M}$ factor) and narrow line profile.
This effect is illustrated in figure 3.16, where it is not possible to make out profiles for a large range of parameter values.

The $Safe$ and *Sound* quantities introduced earlier and applied to the same set of parameters as the $\chi^2{}_{normal}$ demonstrate (figure 3.16) a comparable level of accuracy and indifference to parameter errors. This equivalent behaviour in the frequency and time domains suggest that it is an intrinsic limitation, to be solved by increasing the duration of data and frequency resolution.

## 3.7 Conclusions

The main specificity of Kalman filtering is the time domain model, so its performances are directly limited by the accuracy of that model. When the model is valid, this filter is efficient even when applied directly on Virgo type data (strongly colored noise instead of the normally required white noise).

The loss of performance when a model mismatch occurs was chartered. Automatic model tuning is in theory possible, but has not yet been tackled in this context. Performance estimators are therefore critical to inform an external retuning process. The efficiency coefficients discussed here rely on knowledge of the original noise altered by the violin mode. Alternative indicators are required before trusting this filter with data conditioning.

In the spectral domain it was possible to derive satisfying filtering quality indicators, that can be applied for parameter tuning. Equivalent time domain indicators were obtained, that notably allow a fast update on both the actual presence of the modeled line in the data and the preservation of the broadband background noise.

Multiple-modes filtering is possible by applying either several one-mode filters in parallel, or one multiple-modes filter, whose model matrix would be block-diagonal. Any fast practical implementation would do away with matrices, essentially limiting the difference between the two solutions to the number of running processes.
The single-mode algorithm used so far already has a low computation cost. A rough estimate gives a computation time of less than 1% of data duration, per removed line. Since processing is done one bin at a time, the filter does not require data to be buffered.

For very large values of $Q$ and low masses, this oscillator model might also be used to represent, hence estimate and remove, electronic lines, caused by contamination by the electric supply, as well as calibration lines, forced mirror motions used as a reference for the calibration of the optical response. Compared to actual mono-frequency models, variations in amplitude and phase would be readily allowed. Frequency would be the only tunable parameter, with $Q$ and $M$ fixed to constraint line width. Tracking should not be necessary: an external reference would be available, from the monitoring of the electric power supply, or the chosen parameters of calibration lines.

Dealing wit real data will imply uncertainties on all the parameters, plus possible drifts. The conflicting needs of higher resolution and short update time have to be balanced from the observed behaviour of the physical system. Another concern will be confusion of lines with very close frequencies. Such practical difficulties are likely to reduce the usefulness of the method.

# Bibliography


[1] N. Arnaud *et al*, *Comparison of filters for detecting gravitational wave bursts in interferometric detectors*, *Phys. Rev.* D **67**, 062004 (2003).

[2] L.E. Finn and S. Mukherjee, *Data conditioning for gravitational wave detectors: A Kalman filter for regressing suspension violin modes*, *Phys. Rev.* D **63**, 062004 (2001).

[3] R.E. Kalman, *A new approach to linear filtering and prediction problems*, ASME-Journal of basic engineering **82**, 35-45 (1960).

[4] H.B. Callen and T.A. Welton, *Irreversibility and generalized noise*, Phys. Rev. **83**, 34 (1951).

[5] P.R. Saulson, *Thermal noise in mechanical experiments*, *Phys. Rev.* D **42**, 101990 (1990).

[6] P.M. Morse and K.U. Ingard, Theoretical acoustics (Princeton University Press, 1986).

[7] G.I. Gonzalez & P.R. Saulson, *Brownian motion of a mass suspended by an anelastic wire*, Journal of Acoustical Society of America **96**, 207 (1994).

[8] A. Gillespie & F. Raab, *Thermally excited vibrations of the mirrors of laser interferometer gravitational-wave detectors*, *Phys. Rev.* D **52**, 577 (1995).

[9] F. Bondu & J.Y. Vinet, *Mirror thermal noise in interferometric gravitational-wave detectors*, Phys. Lett. A **198**, 74 (1995).

[10] M. Punturo, *The Virgo sensitivity curve*, Virgo NOTE VIR-NOT-PER-1390-51.

[11] H.W. Sorenson, *Least-squares estimation: from Gauss to Kalman*, IEEE Spectrum **7**, 63 (1970).

[12] J.V. Candy, Signal processing, the model-based approach (McGraw-Hill, 1986).

[13] T. Cokelaer *et al*, *Spectral lines identification and removal in Virgo CITF engineering runs*, *Virgo Note* VIR-NOT-FIR-1390-286 (2004).

[14] <http://pub0.virgo.infn.it/virgo_lines>

[15] W.H. Press *et al*, Numerical Recipes (Cambridge University Press, 1988).

# Chapter 4

# Analysis of Virgo commissioning run data

## Contents



## 4.1 Introduction

Taking advantage of the availability of real non-Gaussian noise produced by an *a priori* stable instrument, the Virgo gravitational wave burst analysis group investigates data from the Commissioning Runs, aiming at detector characterization and preparing for the analysis of data of astrophysical relevance.

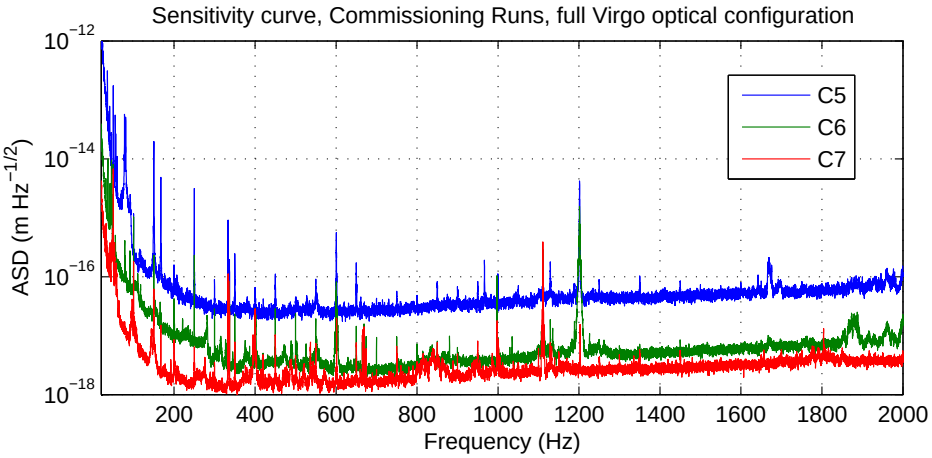


**Figure 4.1:** Calibrated sensitivity of Virgo, estimated from the dark fringe data, subtraction of several noises and renormalization.

Between December 2 and 7 2004, the Virgo collaboration worked on the C5 commissioning run, to keep the interferometer at its working point, successively without and with power recycling. This was the first long data taking with the full optical configuration, though still a mostly manual adjustment of the optical alignment. See [1] and [2] for details on the instrument condition during

the run.
From these efforts, continuous stretches of data were obtained, where the instrument remained in a stable state. The longest is a 5 hours segment, with the instrument working without power recycling. Sensitivity gains were obtained during the Run, but the evolving state of the instrument limits the interest of an in-depth analysis.
Rapid improvements in the control strategy, notably the optical alignment scheme, prompted the C6 Summer Run, two weeks long in August 2005, before the planned shut-down for hardware upgrade. It was again used to improve the tuning of the instrument, and so was immediately followed by the generalization of the automatic alignment to the whole interferometer. The expected gain in sensitivity prompted another shorter Run, C7, right before the upgrade. Figure 4.1 shows the large improvement at low frequency, where control noise is dominant.
Run C7 lasted from September 14th to 19th with few modifications of the instrument configuration and provided the best sensitivity so far. For this reason, although the instrument was less stable than during C6, with a longest continuous lock period of 14 hours against 39 hours during C6, it is the main focus of the following work, after briefly recalling C5 studies.

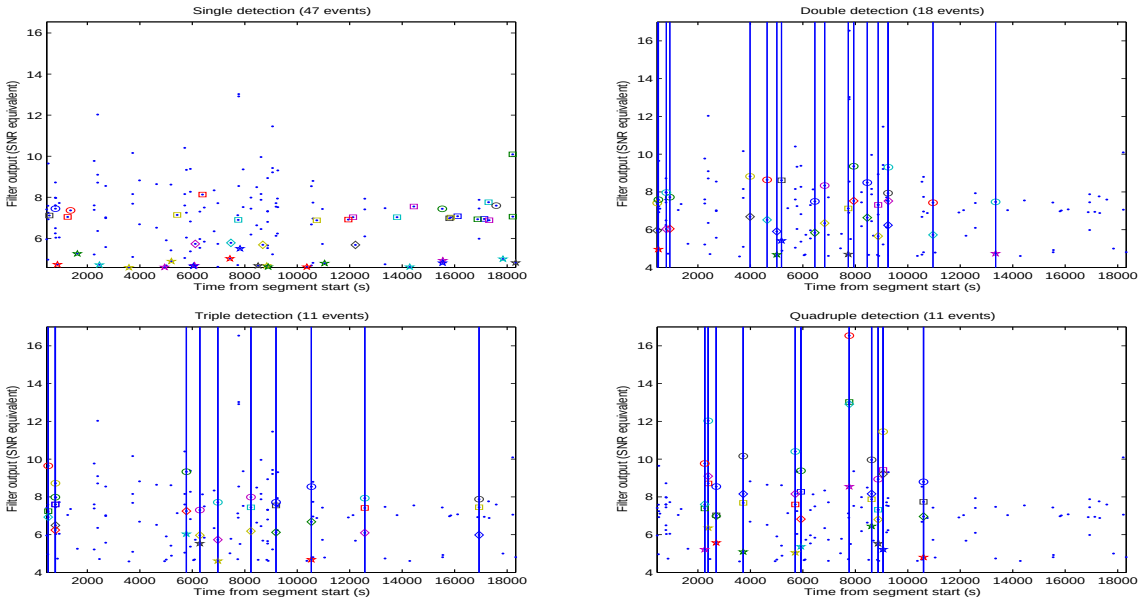


**Figure 4.2:** Burst event candidates over the C5 'stable' period (40 highest 'SNR' events from each method only). All events are plotted four times, using ($\cdot$), with additional vertical lines marking coincidences between methods. Triggers are from MF ($\square$), PC ($\circ$), EGC ($\diamond$) and PF ($\star$).

## 4.2 Investigations on Run C5

Results for C5 were obtained on the 5 h stable period, using raw data, that is before strain reconstruction, on the demodulated in-phase channel. The photo-diode DC signal and the quadrature demodulated channel were also surveyed, with compatible conclusions.

Table 4.1 recalls basic features from burst detection methods in the Virgo collaboration for a quick comparison. All methods include a procedure to adapt to the noise non-stationarity. Timescales of adaptation were of the order of 8 seconds for PF, 13 seconds for PC and EGC, corresponding to the data size used to compute Fourier Transforms, and 300 seconds for MF, for output normalization. Note that the data whitening, for PF and MF, was static.

These four burst detection methods were jointly applied on the C5 'stable' segment and provided lists of transient noise events.
Figure 4.2 summarizes the results, obtained using standard parameters for the algorithms.
The main outcome is that even among the 160 most outstanding (40 per method) events, there is only partial overlap between the methods. Besides, the coincidence with periods identified as not or less stable by statistical methods (introduced in [3] and [4]) is not very good either.

| Method | Algorithm type | Pre-processing | Adaptability | Bandwidth (§)(*) |
|---|---|---|---|---|
| MF | Time domain | Whitening, normalization (a) | Normalization update | 100 - 2000 Hz |
| PC | Correlator | None | PSD update | $< 5kHz$ |
| EGC | Correlator | None | PSD update | 10 - 500 Hz |
| PF | Time-frequency | Whitening, normalization (a) | Normalization update | 40 - 1000 Hz |

**Table 4.1:** Burst detection methods at a glance. (a) Toward zero mean and unit variance. (§) Filter bandwidth must be compounded by the noise PSD: at low-frequency ($\lesssim 40$ Hz) noise levels are too high for meaningful detection.

These differences probably originate in the specific coupling of each burst filter with noise, the explored frequency regions, and the time-scales of the adaptivity.

More studies were conducted with MF and PF, as discussed in [5], with no strong result, owing in particular to the repetitive modifications of the control parameters that complicates the analysis over long durations. Exploiting the hardware waveform injections was difficult due to uncertainties on the calibration of the injected amplitudes.

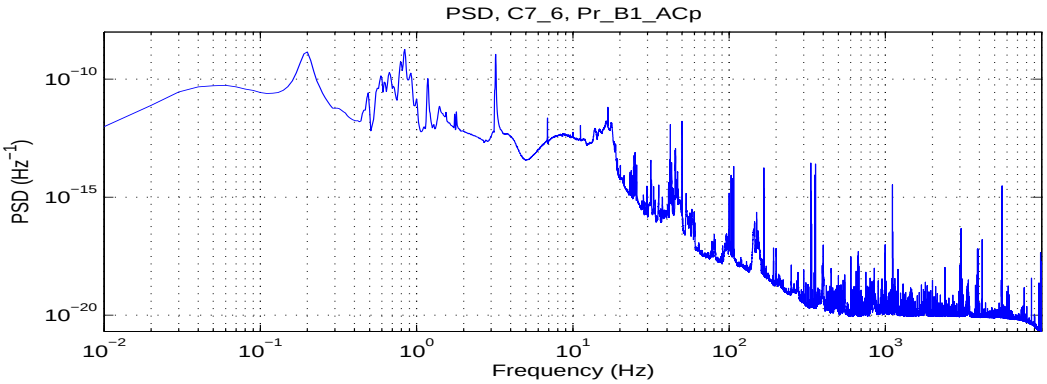


**Figure 4.3:** Averaged PSD for the C7_6 segment, with a resolution of 0.01 Hz.

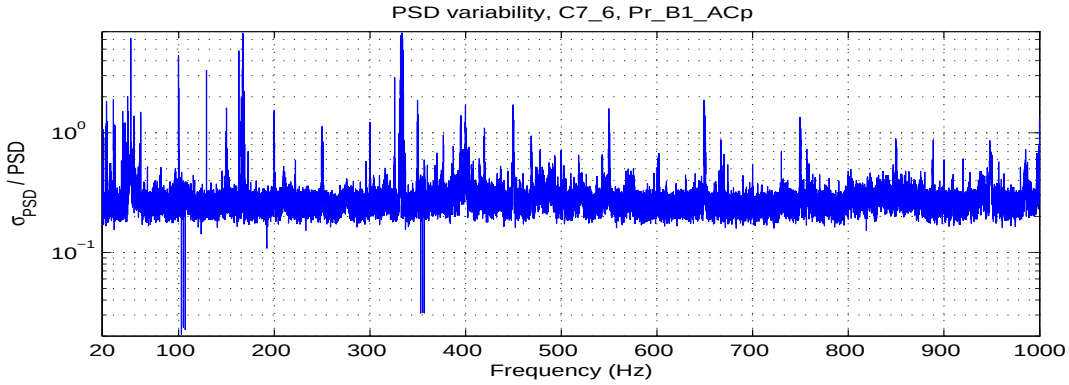


**Figure 4.4:** Indication of local spectral variability for the C7_6 segment. It is given by the ratio $\sigma_{PSD}(f)/PSD(f)$. Each PSD estimate was computed over 1000 seconds of data, with a frequency resolution is 0.01 Hz, hence the average and standard deviation were extracted from about 50 values.

## 4.3 Investigations on Run C7

The following results concern the longest (14 hours) continuous segment, called C7_6 hereafter. The main examined channel was the dark fringe, a direct output of the instrument, with no reconstruction or noise reduction applied. This allowed for a longer stretch of data while limiting couplings to instrumental origins.

Hardware injections took place, in small quantities and with high effective SNR values (15 or more). Signals stood out in the results of burst detection filters, but no further analysis was possible.

The dark fringe canal exhibits a complex accumulation of noise sources, of varying spectral extent, as illustrated in figure 4.3. The noise sources that limit the overall sensitivity are the following (see [6] for a detailed review and quantification) :

- control loops : below 100 Hz, noise is dominated by the controls, both angular (the alignment part) and longitudinal (the locking part).
- acoustic and seismic noise : structures above 400 Hz are related to vacuum pump activity.
- shot noise and electronic noise : sensitivity is limited above 500 Hz by the output power and photo-diode performances.
- laser frequency noise : control of the laser optical frequency, that uses the 3 km arms as a reference length, is polluted by noise from the photo-diodes, thus contributing to the sensitivity limit above 500 Hz.

Using PSD variability as shown in figure 4.4 allows to identify spectral lines and their behaviour. Variability below average is obtained for injected lines, forced motion of the mirrors used for calibration purposes. There are two groups of such lines clearly visible around 103 and 350 Hz. Conversely thermal lines express higher than average variability. At 167 Hz are resonances of the input mode cleaner (IMC) system, while around 668 Hz are the first harmonics of the violin modes from the suspensions of the main interferometer. The fundamental violin modes are around 334 Hz, frequencies also compatible with harmonics of the IMC resonances.

### 4.3.1 EGC analysis of dark fringe data

The full implementation of the EGC event detection chain, as described and evaluated in Chapter 2, was applied on dark fringe data over the full segment.

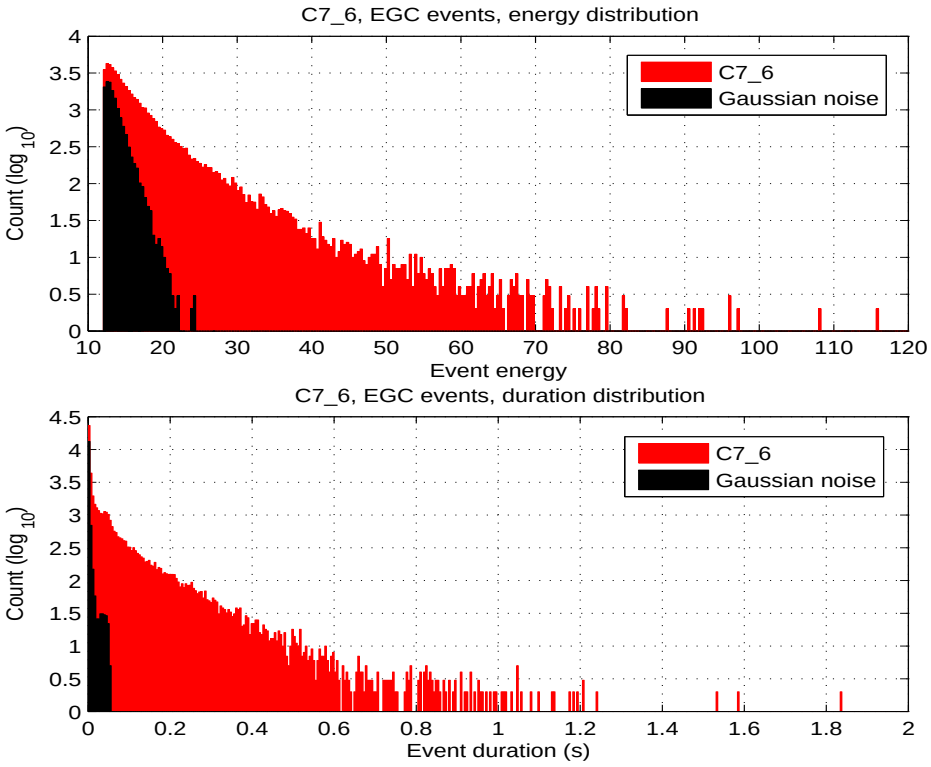


**Figure 4.5:** Histograms of EGC events energy (top) and duration (bottom) over the C7_6 segment.

As could be expected from instrumental data, the output is much more structured than for Gaussian noise. From the algorithm of the filter, it is expected that background fluctuations on

time scales shorter than the filter update, kept to 262 second as used on simulation data, will introduce events that are do not correspond to impulse-like structures. However, the additional normalization of the time-frequency map should cancel out any noise level that is static over the duration of a map, here 13 seconds.
The non-Gaussian behaviour observed for the dark fringe channel are summarized in the histograms of figure 4.5, compared to results from the data set described in Chapter 3 (Virgo-like simulated Gaussian noise, with thermal lines) for the same duration. There is a large excess of events with a high energy or duration over 0.1 seconds.

### Overview of EGC output

The background variability mentioned above was found in the event list, in relation with the very low frequency modes of the mirror suspensions.
From a list of event time $l_t$ it is interesting to produce an auto-correlation histogram, or correlogram from [13], as the plot of the following quantities :

$$c_a(l_t) = \{\delta t = t_2 - t_1 / (t_1, t_2) \in {l_t}^2, t_2 > t_1\} \tag{4.1}$$

From classical statistical treatment, time delays between independent (uncorrelated) events should follow a Poisson's distribution and give a flat correlogram, with no preferred delay. If a periodicity is present, events will occur preferentially every period, so the period and its multiples will have large $c_a$ values, while, for a constant-size list, in-between delays will have lower $c_a$.

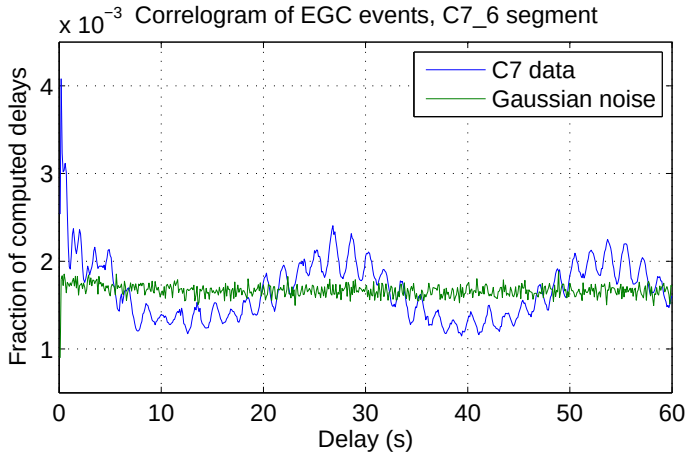


**Figure 4.6:** Correlogram of EGC events for C7_6 compared to a Gaussian simulation reference. Two modulations are visible. Values are normalized by the total number of entries in the plot.

The correlogram of EGC events shows (figure 4.6) two such modulations, of periods 0.6 Hz and 37 mHz. The 0.6 Hz mode was mentioned in Section 1.2.5 as a pendulum motion. The other one comes from the rotation of the last stage of the suspension. See [7] for a full description of the mechanical behaviour of the super-attenuator.

The distribution of energy versus frequency in figure 4.7 shows two narrow peaks, around 25 Hz and 560 Hz, plus a broader shape centered at 480 Hz.

The objective then is to identify the physical causes of events, in order to remove them safely from the list. Localized excesses are very useful for this purpose, as they hint of a recurrent cause, whose identification would allow to remove many events.

### Event populations

Three groups of events were isolated from the EGC list (51360 events), using the above distributions :

- Population 1 (1520 events) : Long duration events. This group is absent from Gaussian simulation results, while most burst-type models translate in shorter EGC events. A cut $\delta t \geq 0.3$ s was used.

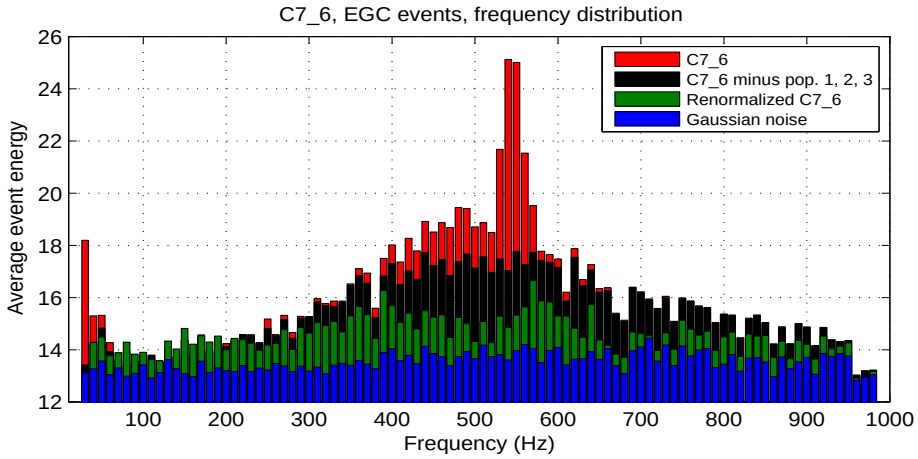


**Figure 4.7:** Distribution of the energy of EGC events against composite frequency. The full EGC list of events is compared to the cleaned list -populations 1, 2 and 3 removed- and a Gaussian data reference.

- Population 2 (2450 events) : Main frequency-localized group. Almost all the highest energy events share a peak frequency close to 560 Hz -templates at (f, Q) = (548.4 , 13.7), (572.6, 9.6) and (572.5, 16.3)-. All events with these peak templates were set aside.
- Population 3 (240 events) : Secondary frequency-localized group. The main energy excess at low frequency can be attributed to peak templates below 25 Hz -(f, Q) = (21.8, 1.3)-.

A first indication of the interest of these populations is provided by the distribution of deposited energy with respect to event (composite) frequency, in figure 4.7. Part of the excess of events compared to simulation can be removed when these events are discarded.

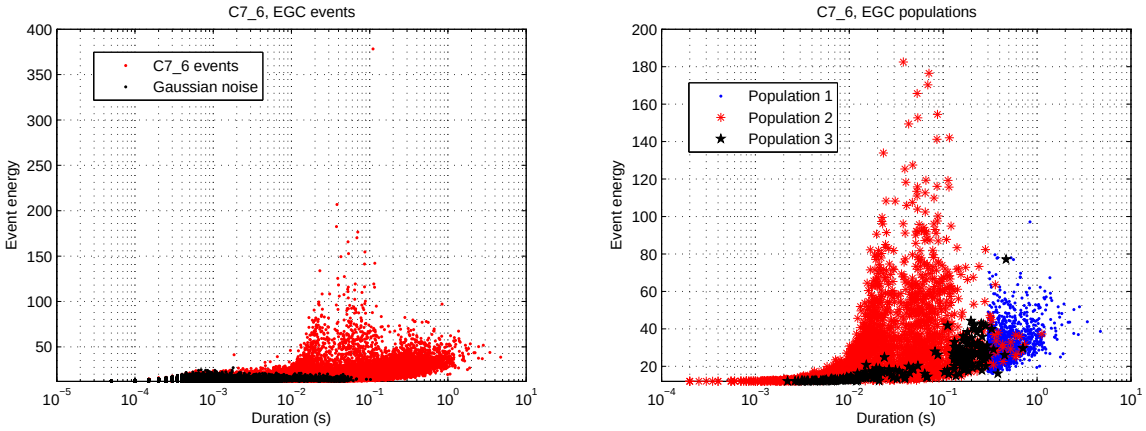


**Figure 4.8:** Event energy versus duration. *Left* Events from C7_6 are compared to Gaussian noise. *Right* The three populations defined in the C7 list are shown together. Some overlap is visible for the duration criterion.

These populations contain events with low energy, that would be difficult to identify otherwise, as illustrated in figure 4.8. Population 1 is not completely separated from the other two, while the duration of population 3 events is bimodal, with a plausible separation around $\delta t = 0.1$ s.
There are also strong event energy variations over the segment, notably for population 2, as visible in figure 4.9. The possible overlap of populations and this variability make it important to associate a physical origin. This should remove unidentified bias of the detection method and solve the population boundary issue.

### 4.3.2 Population identification from auxiliary data

The data set collected during the operation of the instrument contains, beside the dark fringe, many auxiliary data channels, either optical read-out at different positions, as shown in figure 1.3,

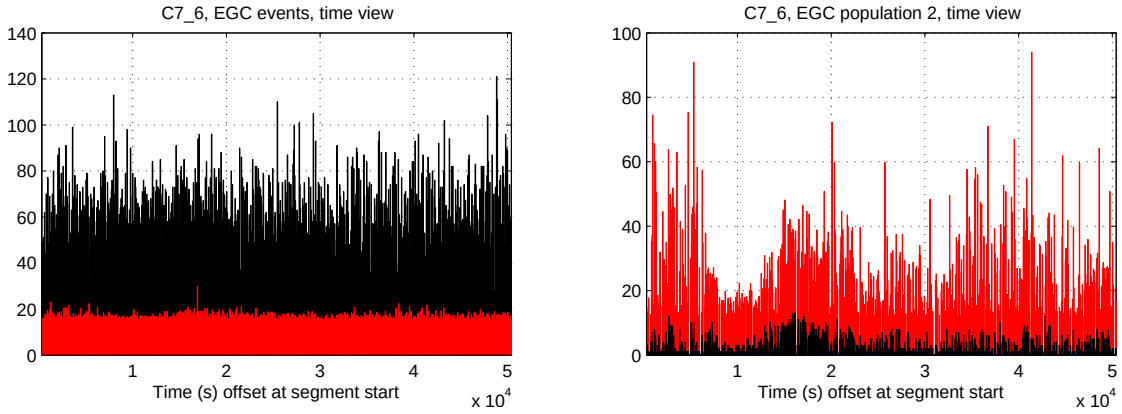


**Figure 4.9:** Variability of all EGC events (*Left*) and in particular population 2 (*Right*). The black histogram shows the event rate per minute, while the red one gives the average event energy over the same period. The scale is valid for both results, with adequate units.

control actuation channels or environment monitoring.
Using the event lists obtained on the dark fringe, physical sources must be traced among auxiliary data. As sampling rates and noise fluctuations vary between channels, it is not always possible to run the EGC filter or any match filter. Methods that use whitened data, like MF, may sometime prove more robust and produce event lists for comparison. However, visual inspection around event times is mandatory to find the shape of the event in time. This is particularly rewarding for high energy events.

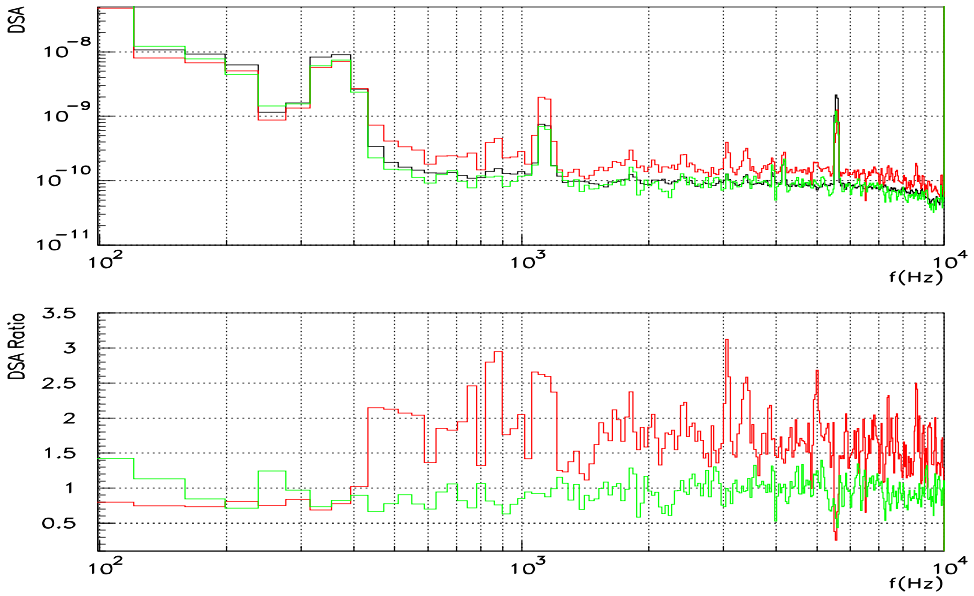


**Figure 4.10:** ASD fluctuation around a population 1 event. *Top* The short duration spectral amplitude density was estimated right before (green curve) during (red curve) and after (black) a population 1 event. *Bottom* The ratio of these densities, between after and before the event (green) and during and after (red), highlights the broadband nature of the fluctuation.

### Physical origin of population 1 events

Visual inspection showed that long duration events corresponded to temporary increases of the noise level over all frequencies above about 100 Hz, as illustrated in figure 4.10. The additional noise may come from laser frequency noise, already dominant at high frequency.

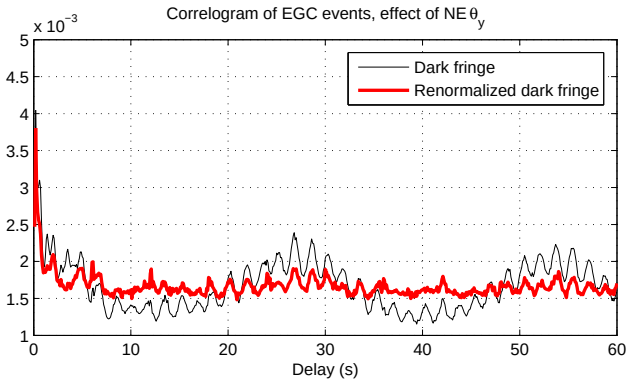


**Figure 4.11:** Correlogram of EGC events for the renormalized dark fringe channel, compared to the initial data set. The 0.6 Hz modulation is still present, though reduced.

This frequency noise should be suppressed by the symmetry of the Michelson arms. When a mirror is misaligned, the instrument moves away from this symmetry and frequency noise is stronger. The introduction of noise by mis-alignment was discussed in [8], and the requirements on the RMS to reach the nominal sensitivity, see also [9], are for the Fabry-Perot mirrors $\delta\omega 210^{-8}$ rad for the entry and $\delta\omega \approx 3 \times 10^{-9}$ for the end mirrors. Current values are of the order of $10^{-7}$ rad for all the mirrors.
It finally appeared that noise injection through control loops emphasized the effect of the tilt of the NE mirror around its vertical axis, as measured by the angle $\theta_y$ in the Virgo nomenclature, on the noise RMS of the dark fringe channel, with a quadratic dependence.
This generalized coupling prompted an *ad hoc* renormalization of the dark fringe signal to suppress this variability.

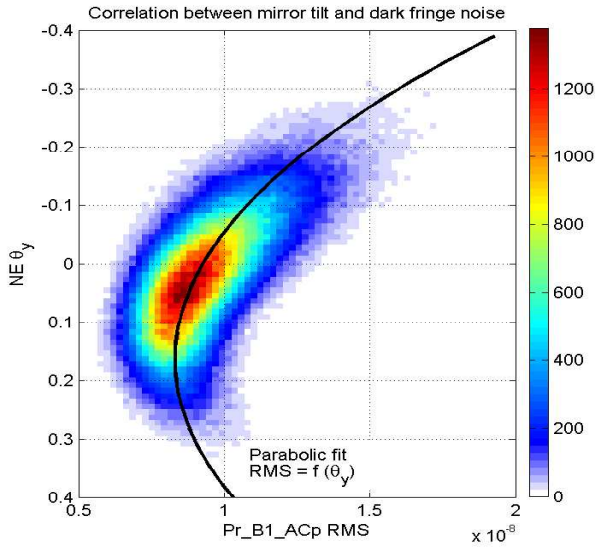


**Figure 4.12:** Distribution of the RMS, over 2 ms, on the dark fringe with respect to the NE mirror $\theta_y$ angle (in $\mu$ rad). The plot shows some 1000 seconds of data, but the coupling was confirmed over the whole segment.

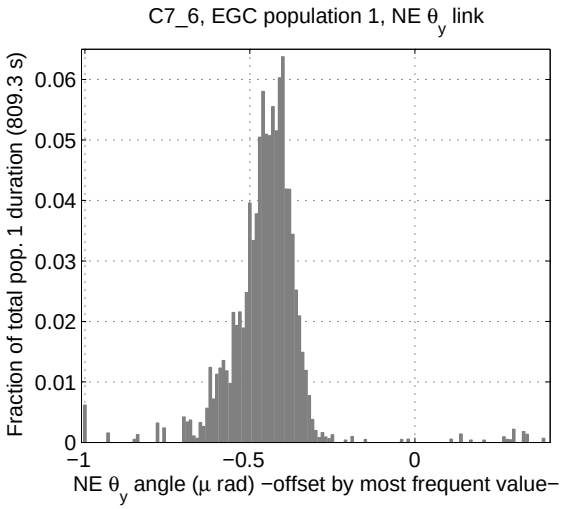


**Figure 4.13:** Physical origin of population 2 events. Integrated event duration with a given averaged NE mirror angles $\theta_y$, over population 1.

Figure 4.11 shows the correlogram of the EGC events found on the renormalized dark fringe, while the coupling is illustrated for a short stretch of data in figure 4.12.
The lowest frequency modulation, at 37 mHz, has mostly disappeared, expect for the visibility enhancement from the 0.6 Hz modulation. This encouraging result may still be improved, with a

proposed reconstruction that include the effect of all the angular motions of all the mirrors.
The affected EGC events were from the long duration group, as clearly shown is figure 4.13. An external event suppression criterion (a veto) based on the value of $\theta_y$ provides a stronger protection against the 37 mHz modulation than the reconstruction, but at the cost of losing about a third of the available data.
While these temporary solutions are useful to isolate the population and look for other lower energy behaviours, the long-term cure requires improved controls to lower the angular motion to the level of the specifications.

### Physical origin of population 2 events

Population 2 events were related to activity on the detection optical bench, as found in an auxiliary channel measuring seismic activity on the -suspended- bench, see figure 4.14.

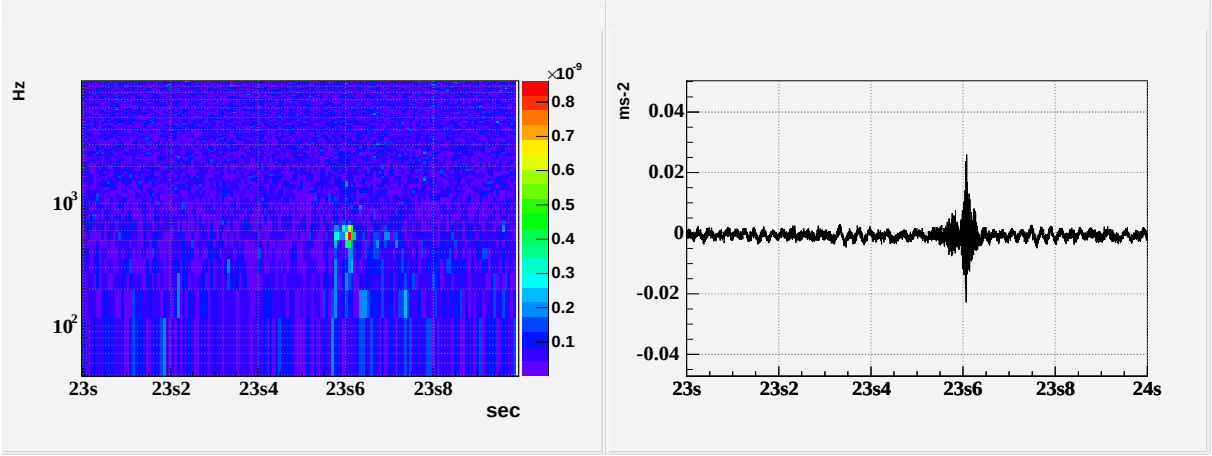


**Figure 4.14:** Coincident extracts of the dark fringe and detection bench seismometer data around a population 2 event. *Left* Short duration spectrogram of dark fringe data. *Right* Time view of seismic bench activity.

A strong hint on their cause came from the regularity (every 6 seconds) of the events, visible as narrows peaks in figure 4.11, the same periodicity used for the re-centering test of the quadrant photo-diodes on this optical bench. The mechanical excitation is only registered as a low accuracy (1 s sampling) indicator of motion of the B5 quadrant photo-diode re-centering motors. High timing resolution confirmation was found by running EGC on the seismometer channel as shown in figure 4.15.

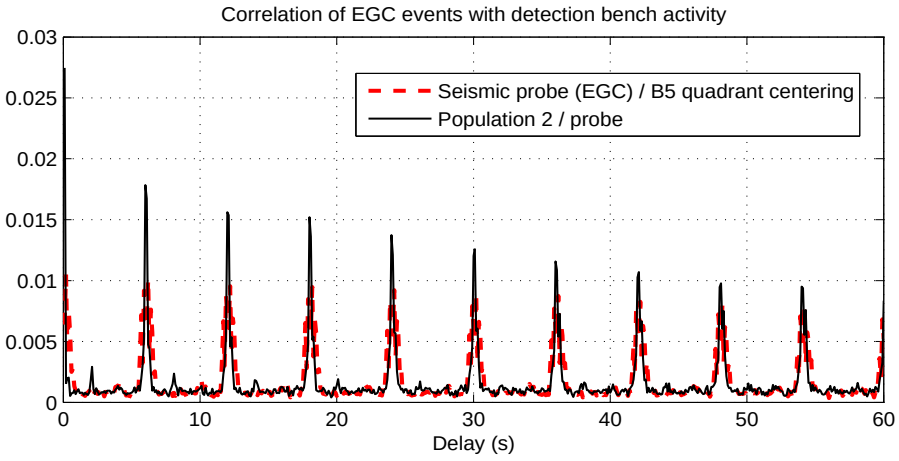


**Figure 4.15:** Time of EGC events from Pr_B1_ACp and a seismometer on the output detection bench are correlated.

With a delay window of 0.5 seconds, is was possible to associate 90% of population 2 events with both events in the EGC output for the seismometer and quadrant re-centering actions. There is

more activity on the detection bench that is coincident with events from the dark fringe. However, the lack of an external confirmation does not permit to rule out accidental coincidences. A clear veto would therefore rely on both motor and seismometer channels.

**Physical origin of population 3 events**

Partial investigations show a correlation between these events and the seismic noise measured in the input mode cleaner building. The seismometer data have large fluctuations at low frequency, that complicates the use of the match filter scheme. Applying a whitening step may reduce the dynamics and allow the extraction of similar events for coincidence with the dark fringe results. The regularity of these events is compatible with the cycles of the air-conditioning system in that building. The large delay between the seismic event and the dark fringe counterpart leaves room for a complex coupling relation, that would be difficult to clarify. Better isolation of the mechanical parts of the air-conditioning may improve the situation.

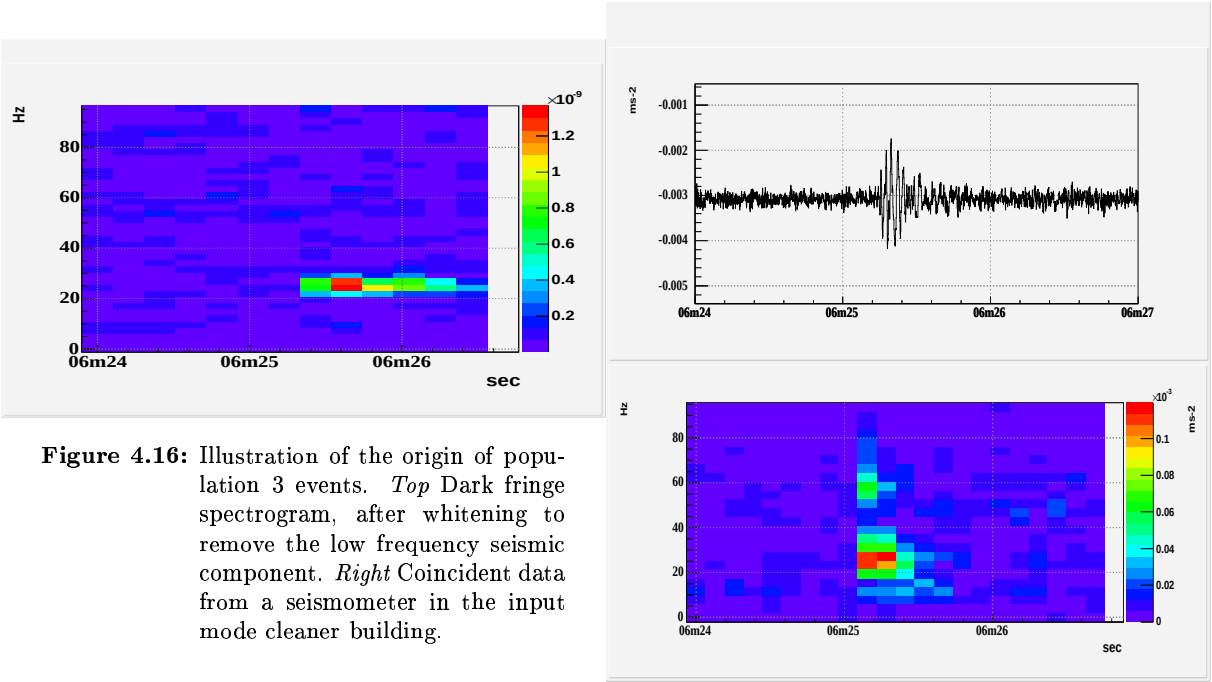


**Figure 4.16:** Illustration of the origin of population 3 events. *Top* Dark fringe spectrogram, after whitening to remove the low frequency seismic component. *Right* Coincident data from a seismometer in the input mode cleaner building.

### 4.3.3 C7 EGC studies summary

The time-frequency information provided by EGC permitted to characterize three types of events. High energy events were also seen with other filters, but frequency selection can be applied with some success independently of event energy.
Physical processes explaining the three populations were identified. Combining data reprocessing and time coincidence vetoes permitted to reduce the discrepancy with the expected Gaussian behaviour, as illustrated in figure 4.17. These histograms are not yet satisfying, notably because the renormalization did not remove all long events, and effects of the suspension motions can still be found in the event list.
There are still many events with excessive energy, that will hopefully be associated to physical phenomena. Until then, an upper limit on gravitational wave signal observation rate would be very high, even compared to what could be expected from the sensitivity curve. It is indeed the nature of burst-like events to have limited impact of the averaged spectral density, as illustrated in Annex A.2.

## 4.4 Thermal lines

The application of a Kalman filter, as presented in Chapter 3, to remove violin and mirror resonances in the data relies on the correct estimation of the parameters. The PSD should provide most of the necessary information. However C7 violin modes are very close, as all wires behave

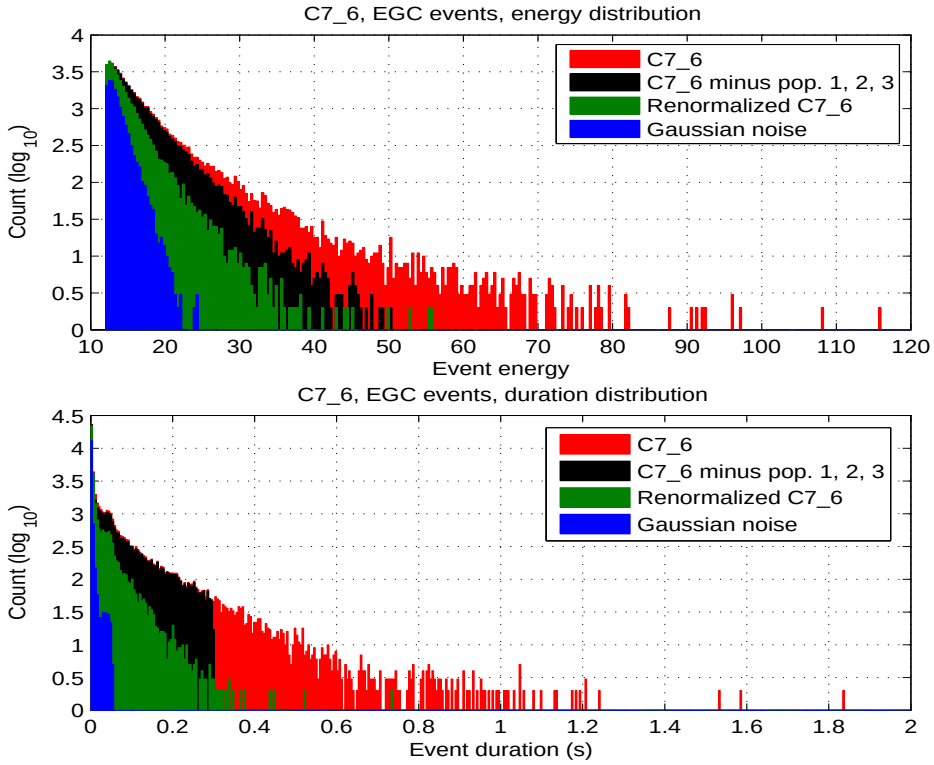


**Figure 4.17:** Histograms of EGC events energy (top) and duration (bottom) over the C7_6 segment. Progressive cleaning of the distribution is achieved by removing events from the three identified populations, then using the renormalized data and removing events belonging to population 2 and 3.

slightly differently. This gives a grouping of narrow lines, see figure 4.18, where the adjustment of a spectral profile to each line is not possible everywhere. The situation seems to be much cleaner for the main mirror modes, at high frequency. The parameter estimation algorithm was first tested on these lines.

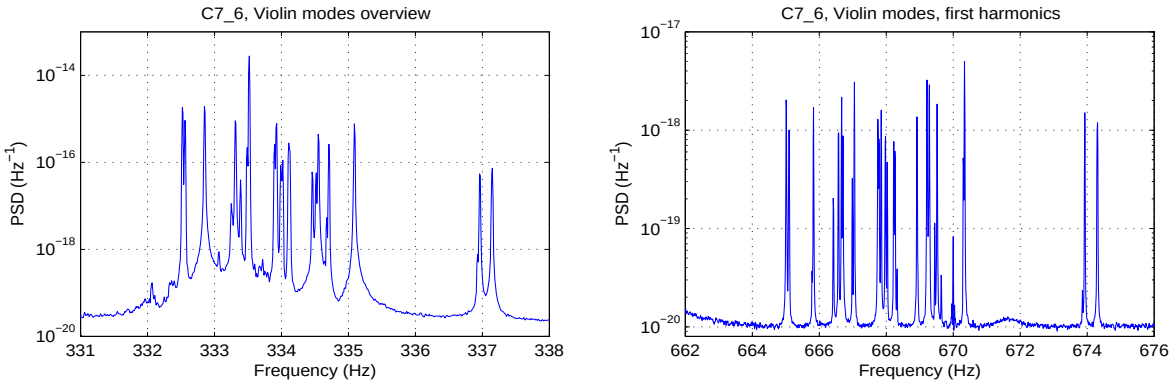


**Figure 4.18:** Spectral view of the violin mode fundamentals (*left*) and first harmonics (*right*). Not all frequencies have been associated with violin modes from the main suspensions. First harmonics from the suspension of the input mode cleaner fall in the same frequency range as the fundamentals.

Figure 4.19 shows the progress so far. The first bump, below 5530 Hz, does not belong to the group of mirror resonances, or with significantly different parameter values. The large peak at 5545 Hz was fitted with success. The remaining narrow feature actually comes from a second resonance very close to the removed one. It may be possible to remove it with an additional filter. This was tested on the following doublet, around 5585 Hz. It is clear that the parameters for the narrower (and lower frequency) mode were not estimated as well. The quality of the PSD estimate

is illustrated by the improvement obtained when tuning with a low noise PSD [1].

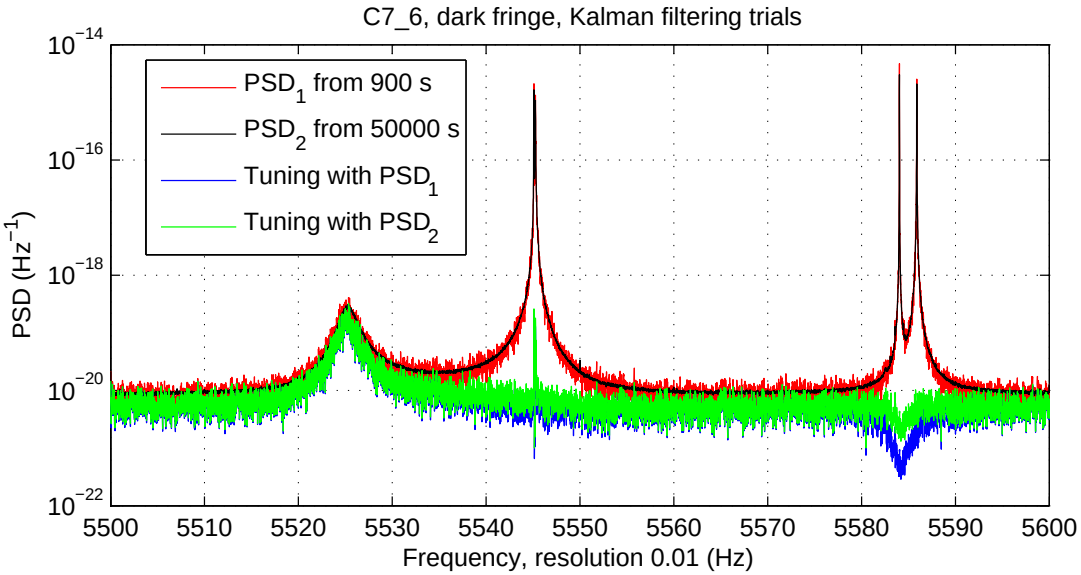


**Figure 4.19:** Spectral view of the main mirror resonances, and first trials to remove them using Kalman filters.

These are partial results, to be confirmed over longer stretches of data, and possibly improved by using variants of the tuning algorithm. The sharpness of the resonances, essentially for the mirror modes, suggests that line parameters are very stable on the scale of a dozen of hours. This is an encouraging point concerning the requirements for parameter tracking.

[1] The increased data duration permitted to lower the variance of the spectral estimate, at fixed resolution.

# Bibliography


[1] S. Braccini for the Virgo collaboration, *Virgo status, to appear in CQGS* (2006).

[2] L. Barsotti for the Virgo collaboration, *Status of Virgo*, *Class. Quant. Grav.* **22S**, 869 (2005)..

[3] G. L. Guidi for the Virgo collaboration, *Data analysis methods for non-Gaussian, nonstationary and nonlinear features and their application to VIRGO*, *Class. Quant. Grav.* **20S**, 915 (2003).

[4] E. Cuoco *et al*, *On-line power spectra identification and whitening for the noise in interferometric gravitational wave detectors*, *Class. Quant. Grav.* **18S**, 1727 (2001).

[5] M.A. Bizouard *et al*, *Burst search results in C5 Run data*, *Virgo Note* VIR-NOT-1390-LAL-298 (2005).

[6] R. Flaminio, R. Gouaty and E. Tournefier, *Analysis of the sensitivity of the recycled interferometer during C5, C6 and C7 runs*, *Virgo Note* VIR-NOT-LAP-1390-313 (2006).

[7] L. Fiori *et al*, *Tune of the NE tower SIESTA simulation*, *Virgo Note* VIR-NOT-PIS-1390-285

[8] F. Barone *et al*, *Effects of misalignements and beam jitters in interferometric gravitational wave detectors*, Phys. Let. A **217**, 90 (1996).

[9] F. Cavalier, *Le Contrôle Global de Virgo*, Thèse d'habilitation à diriger des recherches, LAL 01-69 (2001).

# Conclusion

Interferometric detectors of gravitational waves are now in operation, but the extraction of the rare and low visibility signals from these non-Gaussian time series remains a challenge.
Virgo has not achieved yet its nominal sensitivity and instrumental noises have to be identified and reduced progressively.
This work dealt with two aspects of the analysis, the reduction of the noise *a posteriori* and the detection of short duration signals.
Because their dynamics are well understood, it is possible to remove mechanical resonances in the data, provided the critical parameters, frequency, quality factor and equivalent pendulum mass are correctly estimated. This is validated on simulation data. The accuracy requirements are difficult to meet and dedicated algorithms are proposed and tested in simulation. Application to real data introduces further difficulties, owing to frequency promiscuity. Besides, many narrow band noise features escape the resonant oscillator model, thus limiting the effective improvements on the complexity of the power spectral density.
The short signal detection problem has no obvious solution, given the lack of information of the waveforms and the expectedly small amplitudes. Time-frequency methods are explored here, under several approaches. The dominant issue remains the negative effect of the spectral density of Virgo on detection performances. A robust method is introduced, that offer broadly satisfying performances. Oscillatory signals are recovered with the best energy, time and frequency precision. Other tested waveforms, Gaussian and numerical Relativity models, are more difficult to recover, depending on the detailed signal shape. This observation comforts the principle of multi-method analysis.
Available Virgo data still contain many spurious noise events, notably a large population of short duration oscillations, accessible by time-frequency methods. Progressive identification of physical origins for noise events provides hints for the instrument commissioning work. Further analysis will eventually lead to the definition of environmental and instrumental vetoes.

# Appendix A

# Estimation of spectral quantities

## A.1 Power spectral density

The standard spectral-density estimator used for this work is the Welch-modified periodogram, based on the Fast Fourier Transform algorithm. A detailed discussion on spectral estimators can be found for instance in [1].
The periodogram value for time series $x$ of length N, Fourier transform $\hat{x}$, at angular frequency $\omega$ is defined as :

$$\hat{P}_x(e^{j\omega}) = \frac{1}{N}|\hat{x}(e^{j\omega})|^2 \tag{A.1}$$

It is an estimate of the power density derived from the correlogram :

$$\hat{S}_x(e^{j\omega}) = \sum_{l=-L}^{L} \hat{R}_x[l]e^{-j\omega} \qquad L < N \tag{A.2}$$

with $L = N-1$ for the periodogram. $\hat{R}$ is a biased, but positive, sample autocorrelation function :

$$\hat{R}_x[l] = \frac{1}{N}\sum_{n=0}^{N-l-1} x[n+l]x^*[n] \qquad 0 \leq l \leq N \tag{A.3}$$

and, for $l < 0$, $\hat{R}_x[l] = \hat{R}_x^*[-l]$.

The statistical estimators built from the simple periodogram do not behave very well. Introducing windowing and averaging, as in the Welch procedure, is a palliative. The initial time series is divided in K overlapping segments. Each segment is windowed, with $v$, and the obtained modified periodograms $\hat{P'}_x^{(k)}$ $(1 \leq k \leq K)$ are averaged into a better spectral estimate $\hat{S}_W$ :

$$\hat{P'}_x^{(k)}(e^{j\omega}) = \frac{1}{N}\left|\sum_{n=0}^{N-1} v[n]x^{(k)}[n]e^{-j\omega n}\right|^2 \tag{A.4}$$

$$\hat{S}_W(e^{j\omega}) = \frac{1}{K}\sum_{k=1}^{K} \hat{P'}_x^{(k)}(e^{j\omega}) \tag{A.5}$$

with a condition on $v$ : $\frac{1}{N}\sum_{n=0}^{N-1} v^2[n] = 1$. Among the large variety of possibilities, see [2] for a review, the chosen windowing function is the Hann shape :

$$H(i) = \frac{\alpha}{2}(1 - \cos(\frac{2\pi i}{N-1})) \qquad i \in [0, N-1] \tag{A.6}$$

with $\alpha$ fixed to satisfy the normalization condition.

## A.2 PSD alteration by signal injection

Detection methods relying on the correlation formula compute the spectral normalization on the same data they are filtering to extract signal. The modification of the PSD introduced by the

presence of the injected waveform could alter the estimation of the noise background and modify the effective SNR.
It appears however, as illustrated in figure A.1, that at low signal to noise ratio and low injection occurrence this effect is negligible.

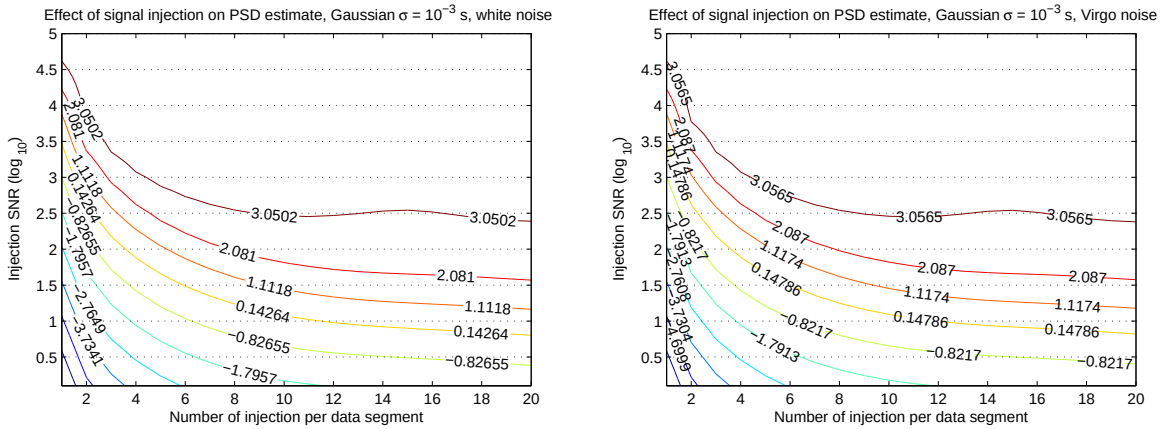


**Figure A.1:** Average contrast (logarithmic scale) between the PSD obtained for pure noise and in the presence of injected waveforms. *Left* for white noise. *Right* for Virgo-type spectral density. Simulation for a 0.05 Hz resolution PSD computed from 200 seconds. The average is done over all frequencies, for 20 realizations.

## A.3 Frequency estimation

An improved frequency estimator for a spectral line can be obtained from a PSD using parabolic fit around the PSD peak of interest. For a peak located at discrete frequency index p, with $f_p = p \times f_{resolution}$, and PSD value L(p), the interpolated parabola maximum is defined by :

$$f_{peak} = f_p + f_{parabola} \quad (A.7)$$
$$L_{peak} = c + b \times f_{parabola} + a \times f_{parabola}^2 \quad (A.8)$$

with

$$f_{parabola} = -f_{resolution} \times \frac{b}{2a}$$

and the following components:

$$a = (L(p+1) - 2L(p) + L(p-1))/2$$
$$b = (L(p+1) - L(p-1))/2$$
$$c = L(p)$$

This interpolation is biased depending on the position of the peak frequency with respect to the sampled values, as measured by $\delta = f_{sample} - f_{peak}$. Bias is null when the frequency coincides with a sample or is at mid-distance between two. An error is also introduced on the amplitude estimation, that gets worse when the peak frequency moves away from a sample. This is illustrated in figure A.2. As shown, a gain of a factor 30 on the frequency resolution of the PSD is possible when the parabolic fit error is reduced, using :

$$f'_{peak} = f_{peak} + \alpha \times \Delta(\Delta - 0.5)(\Delta + 0.5) \quad (A.9)$$
$$L'_{peak} = L_{peak} \times (1 + \beta\Delta^2) \quad (A.10)$$

where $\Delta$ is the distance to the closest sample frequency, normalized by the resolution. Numerical factors $\alpha$ and $\beta$ depend on the windowing scheme, as shown in [3], and were extracted for the retained configuration.

The resolution improvement on bin unit translates to the frequency resolution, apparently without loss. The same gain was obtained on 0.1 Hz and 0.01 Hz resolution spectra, for static frequency features and at different frequencies.

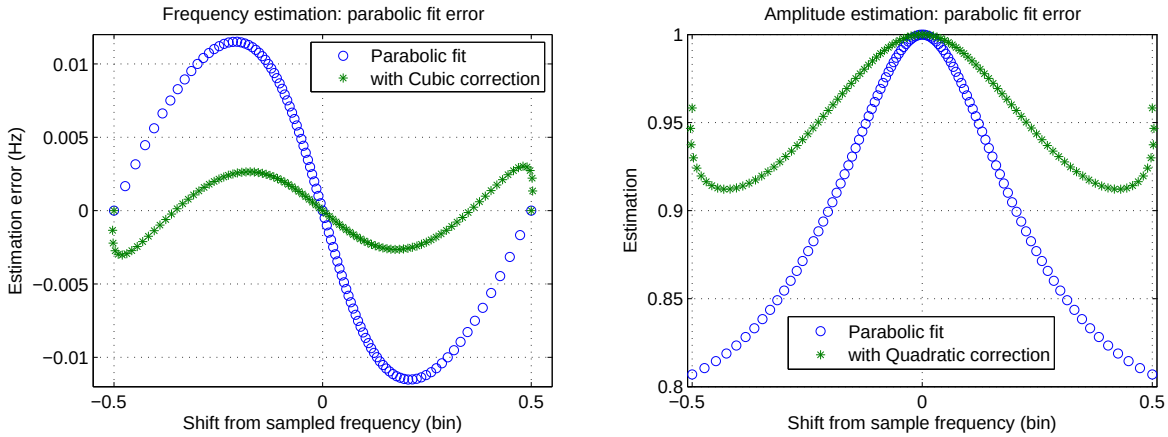


**Figure A.2:** The parabolic fit error and its correction for line frequency *Left* and amplitude *Right*. Simulation for a PSD resolution 0.1 Hz computed from 200 seconds of sinusoidal signal. The same curves were obtained for $f_{peak} = 100$, 1000 and 5000 Hz.

From 100 seconds of data, a resolution of 3 mHz can thus be expected, or 0.3 mHz from 1000 s of data. The practical limitation will come from the time scale of line frequency fluctuations.

# Bibliography

[1] C.W. Therrien, "Discrete random signals and statistical signal processing" (Prentice Hall, 1992).

[2] F.J. Harris, *On the use of windows for harmonic analysis with the Discrete Fourier Transform*, Proc. IEEE **66**, 51 (1978).

[3] M. Abe & J.O. Smith III, *CQIFFT: Correcting bias in a sinusoidal parameter estimator based on quadratic interpolation of FFT magnitude peaks*, Technical report STAN-M-117 (Dept. of Music, Stanford University, 2004).

# Appendix B

# Filter output correlation

Here is considered an alternative view on template selection for a linear detection filter, based on the correlation of output values.

## B.1 Filter output correlation

Given data with Gaussian statistics and a flat power spectral density, it is straightforward to compute the correlation of a linear filter output between two given time indexes, or for the same time between two templates. These can be used to establish a tiling rule along the same line as in Section 2.1.2.

The output of a linear filter of length N can be developed as :

$$\Phi_i = \sum_{j=i}^{j=i+N} a_j x_j \tag{B.1}$$

with $\{ x_j \}$ the data samples that satisfy $E[x_j] = 0$, $E[x_j x_j] = 1$ and $E[x_j x_k] = 0 \ \forall (j,k)\ j \neq k$, and $\{ a_j \}$ the filter coefficients.

The correlation between filter outputs at time index i and i+k is therefore :

$$C_\Phi(i, i+k) = E[\Phi_i \times \Phi_i + k] = E[\sum_{j=i}^{j=i+N} a_j x_j \times \sum_{j=i+k}^{j=i+k+N} a_j x_j] \tag{B.2}$$

Applying the distributivity of the expectation over the sum and available information on data, this equation simplifies into :

$$C_\Phi(i, i+k) = 0 \qquad \text{for } k \geq N \tag{B.3}$$

$$C_\Phi(i, i+k) = 1 \qquad \text{for } k = 0 \tag{B.4}$$

$$C_\Phi(i, i+k) = 1 - E[\sum_{j=i}^{j=i+k-1} (a_j x_j)^2] = 1 - \sum_{j=i}^{j=i+k-1} a_j^2 \qquad \text{for } 0 < k < N \tag{B.5}$$

The principle is the same for the correlation between the output of different templates, of lengths N and M and coefficients $\{ a_j \}$ and $\{ b_j \}$ :

$$C_i(\Phi_a, \Phi_b) = \sum_{j=i}^{j=i+m} a_j \times b_j \qquad \text{for m = min (N, M)} \tag{B.6}$$

### B.1.1 Application to Mean Filter

The Mean Filter [8] is a linear detection method built over a length N, with coefficients $a_j = \frac{1}{\sqrt{N}}\ \forall j \in [1, N]$. The above results apply easily in this case :

$$C_{MF_N}(i, i+k) = 1 - \frac{k}{N} \tag{B.7}$$

$$C_i(MF_N, MF_{N+dN}) = \frac{N}{\sqrt{N(N+dN)}} = \sqrt{\frac{N}{N+dN}} \tag{B.8}$$

To define a template selection rule, it is necessary to introduce a reference signal or bank of signals. Otherwise the choice of a maximum level of correlation between templates may lead us to filter parameters, among which the duration or length, that are not characteristic of the target waveforms.
Another limitation is that these computations are not valid for colored noise, where correlation between samples will depend on the noise profile. It is therefore solely adapted to detection methods where a pre-processing whitening step is applied.

# Appendix C

# Data whitening: an introduction

The principles of the static whitening algorithm [1] used for Virgo data analysis are briefly recalled. Only the Auto-Regressive model is considered. For a white noise input, the power spectral density of the output of an AR filter is given by :

$$S_{AR}(f) = \frac{\sigma^2}{|1 + \sum_{k=1}^{P} a_k e^{-j2\pi kf}|^2} \tag{C.1}$$

where $\sigma$ is the standard deviation of input noise and $a_{k\ 1\leq k\leq P}$ are the AR coefficients.
Conversely, a colored power spectral density can be modeled with an AR filter. The model coefficients can be obtained solving the Yule-Walker equations (see reference [1] in Annex A). It is then possible to whiten a discrete time series $x$ with the same PSD, applying the recursive formula :

$$w[n] = x[n] - \sum_{k=1}^{P} a_k x[n-k] \tag{C.2}$$

The output time series $w$ should have a flat PSD, provided the AR model is accurate enough.

Narrow-band features require many coefficients for a satisfying removal, which explains the high cost (of the order of 3000 parameters) of the whitening step for the full Virgo spectrum, as illustrated in figure C.1.

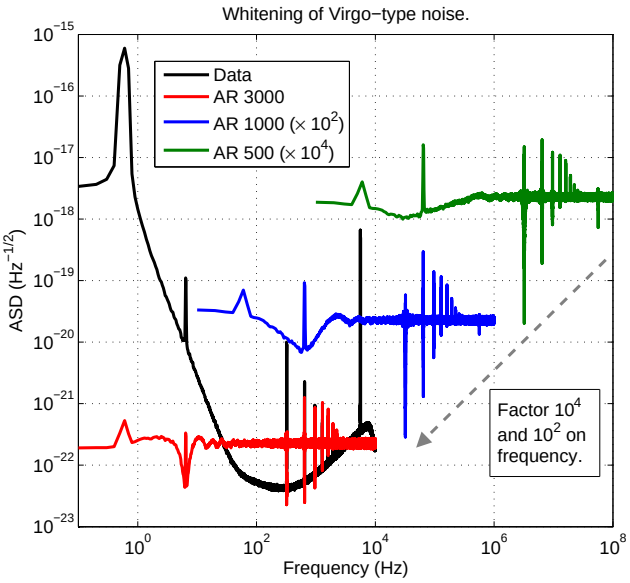


**Figure C.1:** The difficulty of suppressing narrow band features is illustrated by the features related to spectral lines that persist, or even spread over a band of frequencies, even for a large number of whitening coefficients.

# Bibliography

[1] E. Cuoco *Virgo Note* VIR-NOT-PIS-1390-145 (2000)

# Appendix D

# Exploratory work on TF methods

## D.1 Event selection rule

To illustrate the performance margin between an optimal filter and EGC, figure D.1 shows both ROC curves for EGC on tests waveforms and analytic predictions using the formulas of Section 2.1.3.

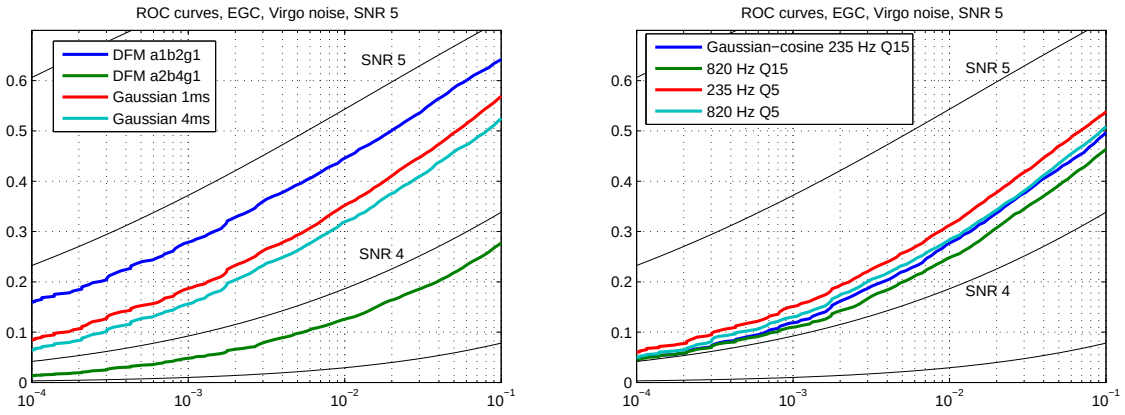


**Figure D.1:** Comparison of standard EGC performances with predictions for an optimal linear filter, for the test waveforms used in Chapter 2. These results come from some 50000 injections spread over 24 hours of simulated data, with a SNR of 5.

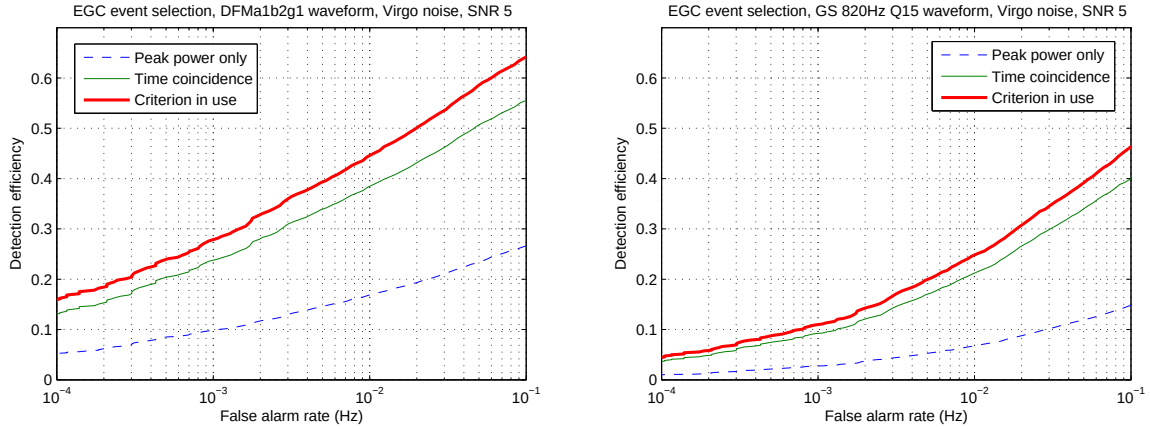


**Figure D.2:** Comparison of EGC performances for a threshold on peak energy, according to the event selection rule, for two waveforms, DFMa1b2g1 to the left, Gaussian-cosine 820 Hz Q 15 to the right. These results come from some 6500 injections spread over 24 hours of simulated data, with a SNR of 5.

The event-selection algorithm presented in Section 2.3.5 is not straightforward. Using the 24 hours of data produced for the LIGO-Virgo exercise, with a Virgo-like spectral density, and two waveforms, DFM a1b2g1 and Gaussian-cosine 820 Hz Q 15, several selection rules were compared. Starting from a raw threshold on pixel energy and neighbour clustering, the first gain comes from the introduction of time coincidence, that combines events from multiple detection of the same structure, thus reducing the false alarm rate without affecting detection efficiency. Further improvement is obtained when the pixel energy threshold is raised, thus reducing the number of events clearing the total energy threshold. This evolution is shown in figure D.2. Intermediate steps, like decreasing the initial pixel energy threshold, did not alter the ROC. This can probably be explained by the correction brought by the time coincidence, with a delay allowance of 0.05 seconds.
The difference in efficiency between the two waveforms come from the minimum template mismatch. As shown in Section 2.4.4, the main structure of DFM a1b2g1 happens to be very well matched. The Gaussian-cosine waveform illustrates the effect of a lower match.

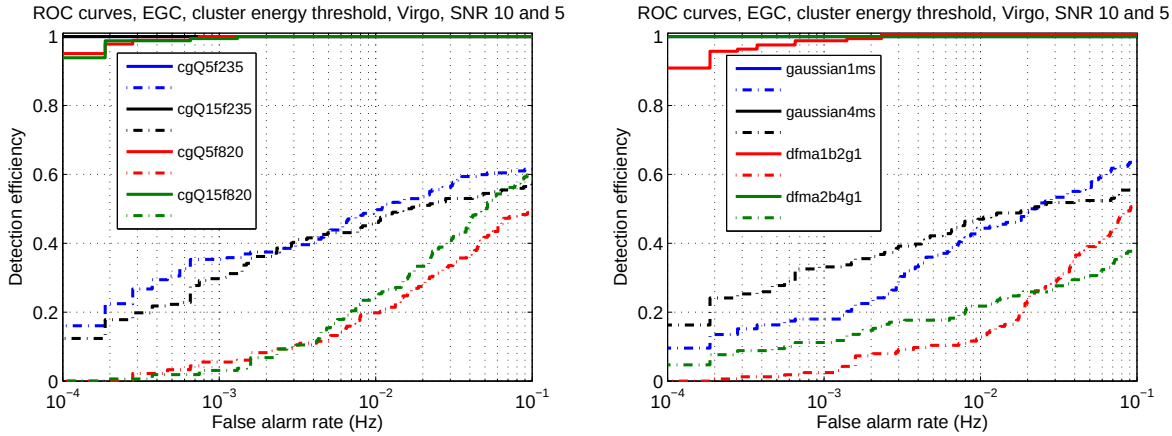


**Figure D.3:** EGC event thresholding using total event energy instead of peak value.

### D.1.1 ROC curves construction

Event selection is done by thresholding a single parameter, the peak energy so far. Comparing results when thresholding with total energy, as done for figure D.3, it appears that performances change differently according to the waveform. For Gaussian-cosine, the short duration signals (f = 820 Hz) are penalized while longer events (f = 235 Hz) are better separated from noise, with an efficiency increase always above 0.05, reaching 0.1 for some false alarm rate values (remember that the statistics from 3 hours of data are not large enough for a precise quantification). The change is marginally positive for Gaussian waveforms as well. And a large improvement, roughly a factor 2 everywhere, is achieved for DFM a2b4g1, as was expected from event characterization.

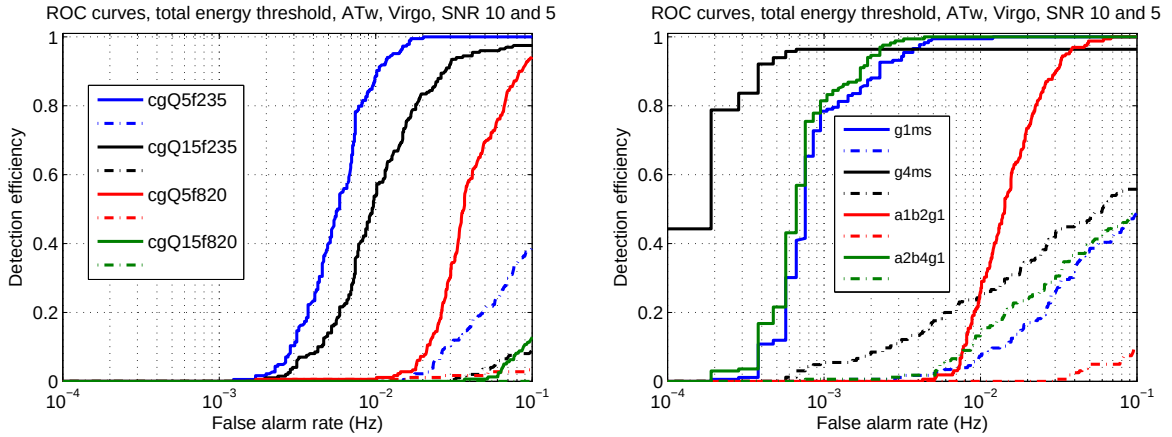


**Figure D.4:** ATw event thresholding using total event energy instead of peak value.

| Waveform | Peak energy | Total energy |
|---|---|---|
| DFM a1b2g1 | 5.25 | 6.23 |
| DFM a2b4g1 | 6.43 | 5.92 |
| Gaussian 1 ms | 5.46 | 5.13 |
| Gaussian 4 ms | 5.70 | 5.08 |
| Gaussian-sine (235,5) | 5.48 | 5.08 |
| Gaussian-sine (235,15) | 5.70 | 5.10 |
| Gaussian-sine (820,5) | 5.73 | 5.93 |
| Gaussian-sine (820,15) | 5.63 | 5.71 |

**Table D.1:** Required signal SNR for a detection efficiency of 50 % with a false alarm rate of $10^{-2}$ Hz. Results are provided for both peak and total energy selection criteria, from simulations of Virgo-type noise.

However, the shift to this alternative threshold may not be a good idea, as efficiency decreases sharply for the other DFM waveform, a1b2g1. The probable reason comes from the near-match between two templates and the waveform, which otherwise produces events of small size.
The question remains of how accidental, compared to the variety of plausible waveforms, this match with DFM a1b2g1 is. Ideally, a segregation strategy would isolate correctly signals behaving either like DFM a1b2g1 or a2b4g1. The same effect was already visible for ATw, see figures 2.15 and D.4.

The sigmoid fit procedure, presented in Section 2.1.3, was used on EGC results, see table D.1. Gains are not systematic, but where achieved they bring EGC close to the best values from other methods, given in table 2.1. Some kind of 'targeted search', privileging some waveform-type by choosing the thresholding method, might be considered. Further explorations would be required to profile what features are targeted.

Unfortunately ROCs built from a larger population of noise events and injections show that any gain at high false alarm rate obtained by using the total energy as a selection threshold is lost below $3 \times 10^{-3}$ Hz, as illustrated in figure D.5. The highest performances are obtained with a set of event-selection parameters slightly different than fixed as the standard for this work.

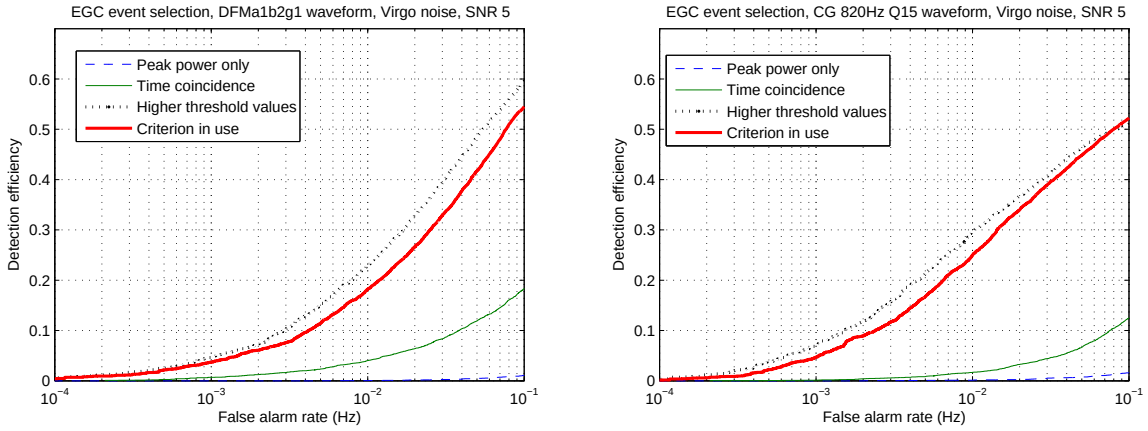


**Figure D.5:** Comparison of EGC performances with a threshold on total event energy, according to the event selection rule, for two waveforms, DFM a1b2g1 to the left, Gaussian-cosine 820 Hz Q 15 to the right. The data set is the same as in figure D.2.

From these simulations, it does not seem advantageous to replace the peak energy with total energy in the final threshold for a generic-purpose analysis. It may still prove interesting to do so as a mean to emphasize events with a large cluster size but relatively low SNR values, in a reasonable noise background (false alarm rate $\approx 10^{-2}$ Hz).

### D.1.2 Exclusion rule from filter behaviour

As described in Section 2.3.5, events are rich objects with many numerical descriptors. So far thresholding has been limited here to the total energy of an event, and it proved satisfying. However, some discriminating power could be expected from other event parameters, like the size or

maximum pixel energy, with the aim of false alarm rate reduction. No conclusive result were obtained so far.

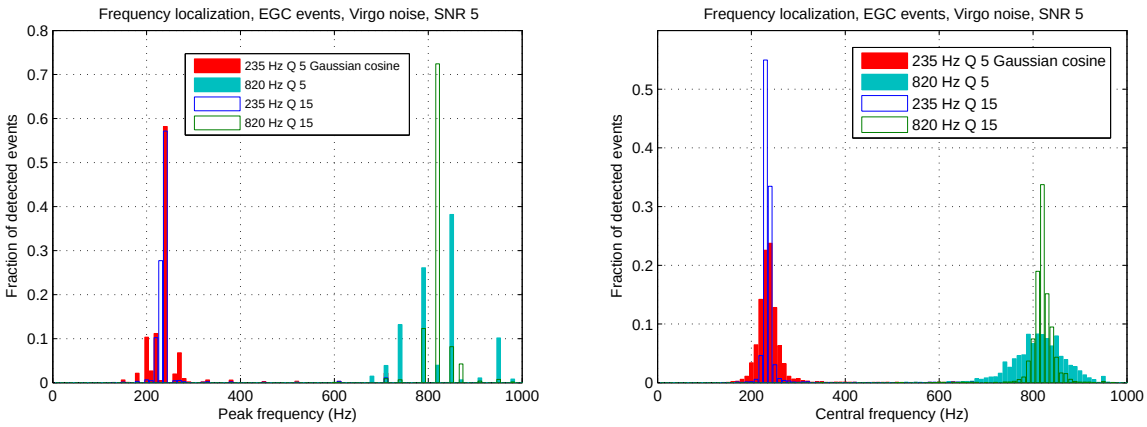


**Figure D.6:** Histogram of the fraction of detected events distributed by peak frequency, to the left and central frequency to the right. Signals are Gaussian-cosine, injected with SNR 5. Some 50000 events were injected over 24 hours of Virgo-type data.

Notably, discriminating events according to their estimated frequency is not always possible. As shown in figure D.6, the indication is valid for the Gaussian-cosine waveforms, well-localized in frequency. The slight difference between the two frequency scales is due to the varying quality factors, not taken into account in the figure but discriminating for signal detection.

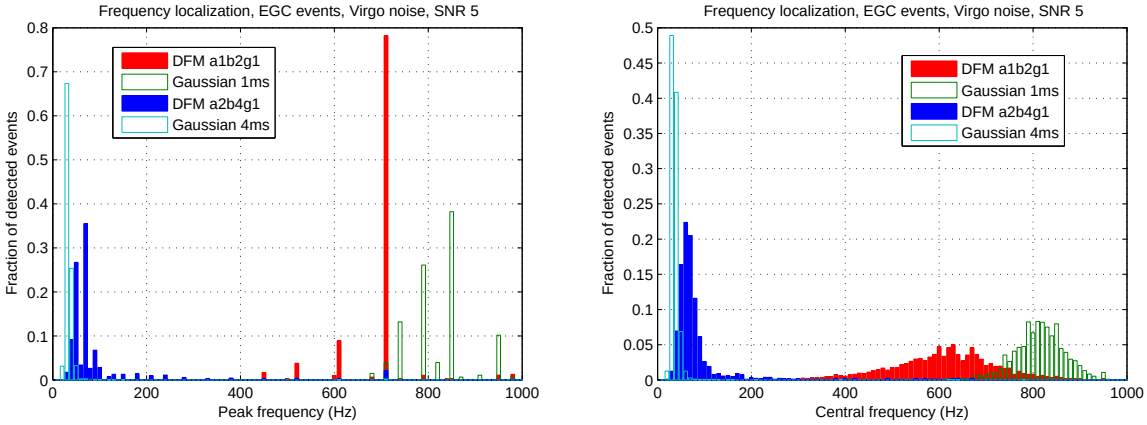


**Figure D.7:** Histogram of the fraction of detected events distributed by peak frequency, to the left and central frequency to the right. Signals are Gaussian and DFM waveforms, injected with SNR 5. Some 50000 events were injected over 24 hours of Virgo-type data.

The Gaussian and DFM waveforms do not give such clear distributions. Figure D.7 illustrates the time-width interpretation of frequency for Gaussian signals and the difficulty of attributing a precise frequency to the more complex DFM waveforms.
As a reminder of the filter behaviour, the same distributions for false alarms (noise-only events) are reproduced in figure D.8.

These elements suggest that the current implementation of the EGC filter is not adequate for a selection of low SNR events by frequency, unless they are supposed to have a dominantly oscillating behaviour, like Gaussian-cosine waveforms. The frequency selection criterion of Chapter 4 was done under this hypothesis and concerned essentially high SNR events, compared to the Gaussian noise simulations. This restriction may affect coincidence strategies where frequency information would be added to timing.

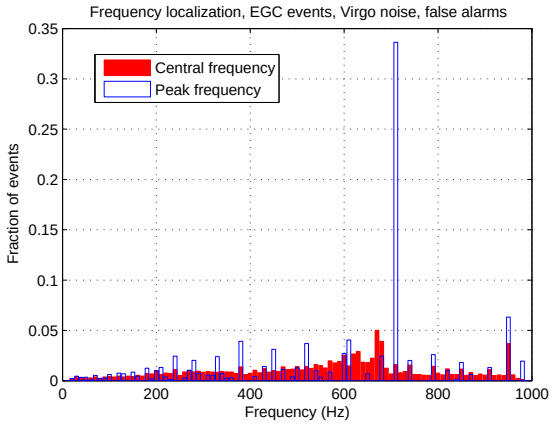


**Figure D.8:** Histogram of the fraction of false alarm events distributed by peak frequency, to the left and central frequency to the right. Results obtained from 24 hours of Virgo-type data.

## D.2 S transform modifications

The chain described in Chapter 2 is very simple and only aimed at including the main aspects of a time-frequency analysis. Straightforward modifications are explored, that seemed promising.

### D.2.1 Non-linear frequency spacing

The original ST scheme is quite resource consuming. As already suggested, a reduction of the number of frequencies computed in a map would be a simple resource saver.
In the spirit of TF tools, a resolution reduction was implemented that takes into account the variable frequency spread of the ST kernel according to the central frequency. Each frequency defines a template, described by equation 2.25. Instead of constant frequency spacing, or template spacing in the frequency dimension, constant frequency overlap is applied, for the Gaussian frequency profile of the kernel:

$$f_{n+1} = f_n * \sigma_f \qquad with \qquad \sigma_f = \sqrt{\frac{-ln(\rho)}{2\pi^2}} \tag{D.1}$$

for $\rho$ the accepted value of the Gaussian at template crossing, normalized between 1 (peak value) and 0. Templates are placed so that no frequency is weighted by less than $\rho$ in the representation. This 'minimal weight' scheme gives a power-law distribution for the central frequencies of templates. It gives similar results for the EGC tiling scheme, when Q is fixed. See figure 2.4 for a graphical illustration of the two procedures.

However, as templates cover a varying bandwidth according to their centre frequency, at high frequency each one represents a very large spectral band, with coefficient mean values accordingly large. To restore correct proportions after the whitening, that suppresses this trend, a rescaling factor is applied, proportional to the centre frequency, between the map-whitening step and the first thresholding. Thus frequency resolution is lost, as expected, while to some extent biased representations are avoided.
Preliminary results indicate varying loss from the original implementation, depending on the tested waveform. This is in agreement with the resolution loss: very localized signals can be badly matched by the templates.
Further work on the spacing parameter and thresholding algorithm might improve these elements.

### D.2.2 Miscellaneous

The so-called map-whitening step, defined in equation 2.30 as a self-normalization method, would tend to suppress excess values (see for instance reference [16] in Chapter 2 for a discussion on this effect). To reduce the risk of degrading a clear signal, normalization quantities obtained from the

previous map could be used. Provided noise statistics is stable enough, emerging features of a map would not be suppressed.

# Appendix E

# Complements on Kalman filtering

## E.1 Derivation of Kalman filter equations

The following proof for the Kalman equations of Chapter 3 is an abridged version of the original by E. Kalman [3].

### E.1.1 Optimal estimation

Given a time series $\mathbf{y}(t)$, either a scalar or vector, defined as the sum of two random variables, a signal $\mathbf{x}(t)$ and noise $\mathbf{n}(t)$, for $t < t_1$, the goal is to estimate $\mathbf{x}(t_1)$, as accurately as possible. In this discussion signal refers to the modeled part of the data (here the oscillator mode) while noise covers everything else in the data. Since $\mathbf{y}(t)$ are the only available elements, the only option is to build $\hat{\mathbf{x}}(t_1)$, a statistical estimate of $\mathbf{x}(t_1)$, as a function of $\mathbf{y}(t)$. The estimation error is then $\epsilon = \mathbf{x}(t_1) - \hat{\mathbf{x}}(t_1)$. It is natural to define the best estimate $\mathbf{x}^*(t_1)$ as the one that minimizes the average norm of $\epsilon$.
Now restricting $\hat{\mathbf{x}}(t_1)$ to be a linear combination of the $\mathbf{y}(t)$, it is interesting to consider the linear manifold $Y(t)$, that contains all linear combinations of the random variables $y$ up to time $t$. Defining orthogonality of random variables $u$ and $v$ as $E[uv] = 0$, an orthogonal base can be found for $Y$. Any random variable $\mathbf{x}$ can then be projected as an element $\bar{\mathbf{x}}$ of $Y$ plus a residue $\tilde{\mathbf{x}}$ orthogonal to $Y$.
Considering the 2-norm, $L(\epsilon) = \epsilon^2$, the best estimate for $\mathbf{x}(t_1)$ from information (measurements $\mathbf{y}$) till time $t$, compactly noted $\mathbf{x}^*(t_1|t)$, is the orthogonal projection of $\mathbf{x}(t_1)$ on $Y$. For Gaussian variables, this projection is equal to the conditional expectation of $\mathbf{x}(t_1)$ knowing $Y$, noted $E[\mathbf{x}(t_1)|\, Y(t)]$. The hybrid notation $\hat{E}$ acknowledges this equality.
A linear process excited by a Gaussian noise will be described by another Gaussian random variable, for which the above results apply.

### E.1.2 Kalman equations

Consider a discrete-time dynamical system of internal state $\mathbf{x}$ and observable $\mathbf{y}$, modeled as :

$$\mathbf{x}(t+1) = \mathbf{\Phi}(t+1;t)\mathbf{x}(t) + \mathbf{u}(t) \tag{E.1}$$
$$\mathbf{y}(t+1) = \mathbf{M}(t)\mathbf{x}(t) \tag{E.2}$$

with $\mathbf{x}$, $\mathbf{y}$ and $\mathbf{u}$ vectors, $\mathbf{\Phi}$ and $\mathbf{M}$ matrices, from the state-space formalism of Chapter 3. Transposed vector or matrix $a$ will be written $\mathbf{a}'$. The excitation term $\mathbf{u}$ is taken to be an Gaussian random variable.
The problem at hand is to compute an estimate $\mathbf{x}^*(t+1|t)$ of $\mathbf{x}$ knowing all the observations at previous discrete times $Y(t) = \{\mathbf{y}(t_i)\,,\, t_i \leq t\}$, under the condition that it minimizes the average error to $\mathbf{x}(t+1)$.

Assuming that $\mathbf{x}^*(t|t-1)$ is known, the following step is given by :

$$\begin{aligned}\mathbf{x}^*(t+1|t) &= \hat{E}[\mathbf{x}(t+1)|\, Y(t)] \\ &= \mathbf{\Phi}(t+1;t)\mathbf{x}^*(t|t-1) + \hat{E}[\mathbf{u}(t)|\, Y(t-1)] + \hat{E}[\mathbf{x}(t+1)|Z(t)]\end{aligned} \tag{E.3}$$

where $Z$ is the linear manifold generated by $\tilde{\mathbf{y}}(t|t-1)$, from the projection of measurement $\mathbf{y}(t)$ on $Y(t-1)$. The other part of the orthogonal decomposition belongs to $Y(t-1)$ and can be expressed from previous results as $\bar{\mathbf{y}}(t|t-1) = \mathbf{M}(t)\mathbf{x}^*(t|t-1)$.
From the independence of the realizations of $\mathbf{u}$, $\hat{E}[\mathbf{u}(t)|\,Y(t-1)] = 0$. By definition of a manifold

$$\hat{E}[\mathbf{x}(t+1)|\,Z(t)] = \mathbf{\Delta}^*(t)\tilde{\mathbf{y}}(t|t-1) \tag{E.4}$$

with $\mathbf{\Delta}^*$ a matrix. Hence the expression :

$$\mathbf{x}^*(t+1|t) = \mathbf{\Phi}^*(t+1;t)\mathbf{x}^*(t|t-1) + \mathbf{\Delta}^*(t)\mathbf{y}(t) \tag{E.5}$$

where

$$\mathbf{\Phi}^*(t+1;t) = \mathbf{\Phi}(t+1;t) - \mathbf{\Delta}^*(t)\mathbf{M}(t) \tag{E.6}$$

The estimation error is now given by :

$$\begin{aligned} \tilde{\mathbf{x}}(t+1|t) &= \mathbf{x}(t+1) - \mathbf{x}^*(t+1|t) && \text{(E.7)} \\ &= \mathbf{\Phi}(t+1;t)\mathbf{x}(t) + \mathbf{u}(t) - \mathbf{\Phi}^*(t+1;t)\mathbf{x}^*(t|t-1) - \mathbf{\Delta}^*(t)\mathbf{M}(t)\mathbf{x}(t) \\ &= \mathbf{\Phi}^*(t+1;t)\tilde{\mathbf{x}}(t|t-1) + \mathbf{u}(t) && \text{(E.8)} \end{aligned}$$

with a covariance matrix :

$$\begin{aligned} \mathbf{P}^*(t+1) &= E[\tilde{\mathbf{x}}(t+1|t)\tilde{\mathbf{x}}'(t+1|t)] \\ &= \mathbf{\Phi}^*(t+1;t)\mathbf{P}^*(t)\mathbf{\Phi}'(t+1;t) + \mathbf{Q}(t) \end{aligned} \tag{E.9}$$

where $\mathbf{Q}(t) = E[\mathbf{u}(t)\mathbf{u}'(t)]$.

Finally, to explicit the transition matrix $\mathbf{\Delta}^*(t)$, orthogonality relations are used. Equation E.4 gives

$$\begin{aligned} E[\mathbf{x}(t+1) - \mathbf{\Delta}^*(t)\tilde{\mathbf{y}}(t|t-1)]\tilde{\mathbf{y}}'(t|t-1) = 0 \\ E[\mathbf{x}(t+1)]\tilde{\mathbf{y}}'(t|t-1) = E[\mathbf{\Delta}^*(t)\tilde{\mathbf{y}}(t|t-1)]\tilde{\mathbf{y}}'(t|t-1) \end{aligned} \tag{E.10}$$

From equations E.2 and E.7, substitutions are possible, that simplify from orthogonality or definition :

$$\begin{aligned} E[\tilde{\mathbf{x}}(t+1|t) + \mathbf{x}^*(t+1|t)]\tilde{\mathbf{y}}'(t|t-1) = E[\mathbf{\Delta}^*(t)\mathbf{M}(t)\tilde{\mathbf{x}}(t|t-1)]\tilde{\mathbf{x}}'(t|t-1)\mathbf{M}'(t) \\ E[\tilde{\mathbf{x}}(t+1|t)]\tilde{\mathbf{x}}'(t|t-1)\mathbf{M}'(t) = \mathbf{\Delta}^*(t)\mathbf{M}(t)\mathbf{P}^*(t)\mathbf{M}'(t) \end{aligned} \tag{E.11}$$

Equation E.8 and the independence of $\mathbf{u}$ and $\mathbf{x}$ then give :

$$\begin{aligned} E[(\mathbf{\Phi}^*(t+1;t)\tilde{\mathbf{x}}(t|t-1) + \mathbf{u}(t))]\tilde{\mathbf{x}}'(t|t-1)\mathbf{M}'(t) = \mathbf{\Delta}^*(t)\mathbf{M}(t)\mathbf{P}^*(t+1)\mathbf{M}'(t) \\ \mathbf{\Phi}^*(t+1;t)\mathbf{P}^*(t)\mathbf{M}'(t) = \mathbf{\Delta}^*(t)\mathbf{M}(t)\mathbf{P}^*(t+1)\mathbf{M}'(t) \end{aligned} \tag{E.12}$$

Provided $\mathbf{\Phi}^*$ is positive definite, no row of $\mathbf{M}$ is ever a linear combination of others, it is possible to extract

$$\mathbf{\Delta}^*(t) = \mathbf{\Phi}^*(t+1;t)\mathbf{P}^*(t)\mathbf{M}'(t)[\mathbf{M}(t)\mathbf{P}^*(t)\mathbf{M}'(t)]^{-1} \tag{E.13}$$

These are all recursive formulas, that need only initial values to deliver the required estimate. A standard starting point is :

$$\begin{cases} \tilde{\mathbf{x}}(t_0|t_0-1) = \mathbf{x}(t_0) \\ \mathbf{P}^*(t_0) = E[\mathbf{x}(t_0)\mathbf{x}'(t_0)] \\ \mathbf{Q}(t_0) = E[\mathbf{u}(t_0)\mathbf{u}'(t_0)] \end{cases} \tag{E.14}$$

## E.2 Additional explorations

### E.2.1 Time-domain local frequency estimation

In the simplified case of pure sinusoidal data $x(t) = a \times \cos(\omega t)$, it is possible to recover the frequency from the time derivative $x'(t) = \omega \times a \times \sin(\omega t)$ once removed the oscillation. This can be conveniently done using the second moment of the time series :

$$\omega_{local} = \frac{\sigma(x')}{\sigma(x)} \tag{E.15}$$

$$= \frac{\omega \times a \times \frac{1}{T}\sigma_{t=t_0}^{t_0+T}\sin(\omega t)}{a \times \frac{1}{T}\sigma_{t=t_0}^{t_0+T}\cos(\omega t)} \tag{E.16}$$

$$\omega_{local} \approx \omega \tag{E.17}$$

computed for a duration $T$, either long compared to a period $1/\omega$, or, for a short-time estimations, a multiple of the period.
Applied to the Kalman filter estimate series $\hat{x}(t)$, this 'local frequency' estimator gives consistent results as long as the oscillatory part is dominant, in agreement with the resonator model. When the filter is mistuned, part of the uncorrelated noise is integrated in $\hat{x}$. This is the origin of the 'PSD holes' mentioned in Section 3.4.1. This contamination in turns falsifies the above relations, allowing for a mismatch indication. When all other parameters are correctly tuned, the frequency error can be recovered very clearly, see figure E.1, with a resolution, as constrained by the standard deviation, competitive with the spectral estimate.

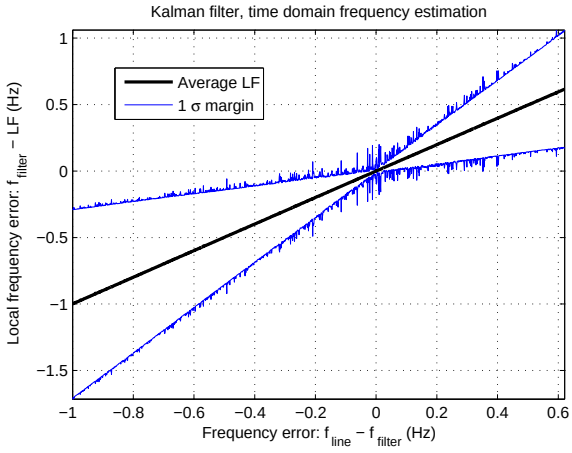


**Figure E.1:** Local frequency estimates according to the frequency mismatch between the actual line and the filter parameter. Values obtained from about 2500 local frequency estimates, corresponding to 100 seconds of data, with a line at 300 Hz, $Q = 5 \times 10^5$ and $M = 10^6$ kg. White Gaussian noise background.

Two observed limitations suggest this parameter is not suitable for tuning purposes. Firstly, when the filter frequency is changed, the optimal sample size to cover an integer number of periods may also change, along with the remaining binning error. This complicates comparison for a sweep in frequency. Secondly, mismatch on other parameters alter the estimation, but the minimum discrepancy between filter frequency and local estimation may be found at any tuning value.
It is therefore not possible to constrain parameters other than frequency, and little robustness can be expected.

### E.2.2 Time domain response to parameter evolution

Acknowledging the presence of glitches and the evolution of parameter values, it seems important to look more closely to short delay filter response, in the time domain.
Going through the filter's available outputs, two coefficients were identified that react strongly to large instantaneous parameter mismatch, the *innovation* and the 2-norm of the estimate. Monitoring their mean value and variance, a clear reaction to mismatch on the resonant frequency and variance for both process and measurement noises is seen.

The innovation is an intermediate step in the updating loop. It compares the prediction to the measure, which includes all other contributions to the data. Therefore it cannot be very sensitive, but it is this coefficient, rescaled by K, that will be used to correct the prediction so it still could be a relevant mismatch indicator. Preliminary tests, see figure E.2, show an interesting behaviour for its variance. These are large mismatch, and the effect of smaller discrepancies remains to be seen.

The other output retained is the adapted 2-norm of the estimate, $es = \sqrt{\hat{x}^2 + (\hat{\dot{x}}\delta t)^2}$, physically equivalent to a distance. It does not respond to all introduced mismatches, as visible in figure E.3, but could complement the innovation.

To reduce the cost of filter quality estimation, it would be interesting to use estimators in

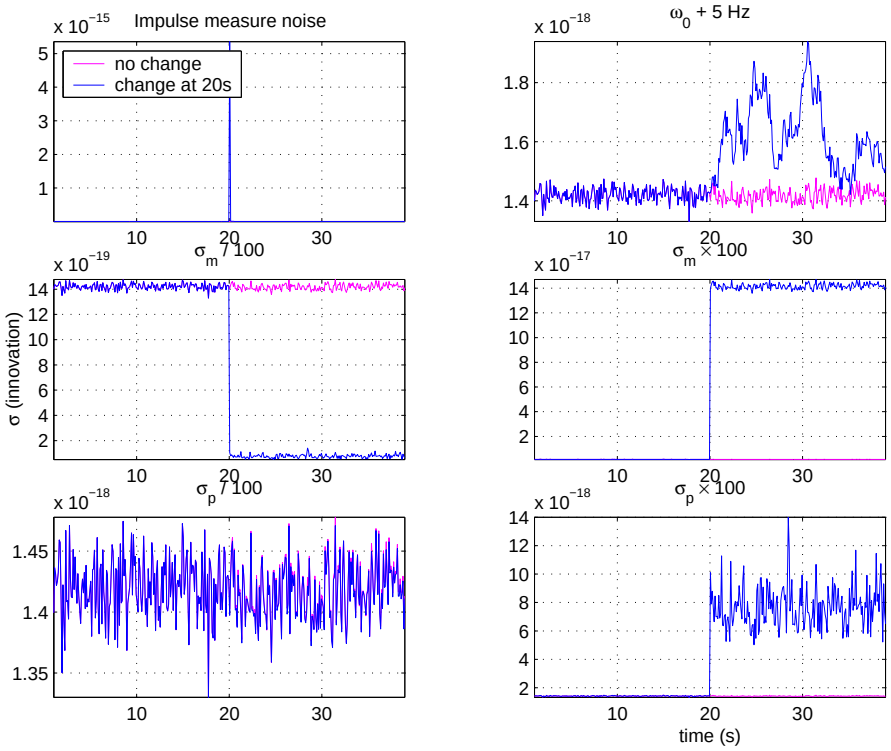


**Figure E.2:** Time domain parameter mismatch estimator: the standard deviation of the Kalman innovation. The signals represented show the variation of the standard deviation of the innovation when, having allowed the filter to settle with the optimal parameters, a parameter mismatch is introduced, at time 20s, on Gaussian white noise. Clockwise from top left, impulse on the measured signal, mismatch of 5Hz on $\omega_0$, $\sigma_m$ divided by 100, multiplied by 100, and the same for $\sigma_p$. For each plot, two signals are shown, with and without mismatch. Note the absence of marked effect for $\sigma_p \times 100$.

the time domain, computed from the filter variables. Unfortunately, no variation on these two parameters was found when changing the quality factor, even by large values. Besides, it is not clear whether or not these short time effects could serve as tuning indicators.
With a white measurement noise model, the filter innovation averaged norm was minimized when the filter was tuned. Unfortunately, this behaviour was not reproduced with Virgo noise.

### E.2.3 Modifications of the Kalman filter

#### Augmented Kalman filter

As a way to maintain a consistent filter behaviour when going from white to colored measurement noise, an extension of the simple Kalman filter used so far was tested. Instead of modeling only the resonant mode, the measurement noise is included, represented by a constant affected by a random walk component. An illustration of this approach is available for instance in [1]. The coloration of the noise series $n$ is introduced by a correlation coefficient relating successive times: $n_{k+1} = \psi_{corr} \times n_k + \nu$, where the excitation $\nu$ is large enough to describe the actual noise behaviour.
This scheme proved satisfying for static and correctly tuned parameters, with a reduction on broadband error compared to the standard implementation, but did not provide any improvement concerning the parameter tuning issue: the filter was not able to adjust to a parameter mismatch.

#### Unscented Kalman filter

Another recent development on model-based filtering, presented in [2], proposed to reproduce the behaviour of non-linear systems using several filters with slightly different parameters, to be adjusted according to the estimated error. This scheme should allow a dynamic tuning of the filter. While results for the favorable static case were interesting, with a reduction of broadband noise,

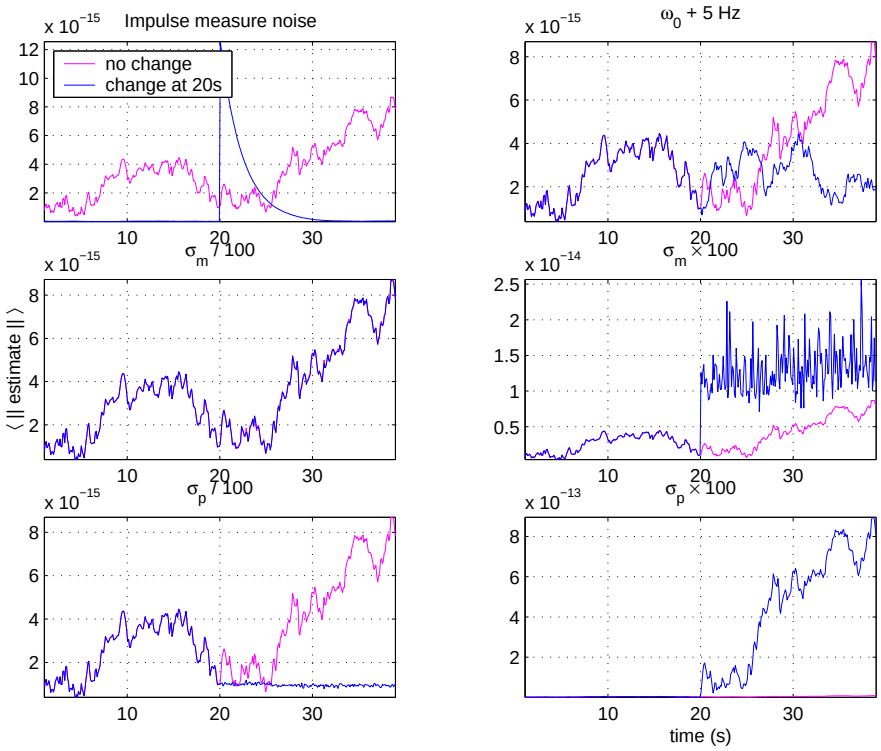


**Figure E.3:** Time domain parameter mismatch estimator: the norm of the Kalman estimate. The plots are for the same situations as fig. E.2.

the studied implementation proved unable to estimate the variation of the resonance frequency. Overall, these alterations still rely on step-by-step computations, while the physical process under consideration does not react immediately to an alteration in its parameters. It seems that too much emphasis is given to rapid noise fluctuations. Improvements could come from the introduction of a second characteristic time for the parameter tuning, orders of magnitude longer than the system-state update time.

# Bibliography

[1] G. Bishop and G. Welch, *An Introduction to the Kalman Filter* (ACM SIGGRAPH Course, 2001).

[2] S.J. Julier, J.K. Uhlmann, *A new extension of the Kalman filter to nonlinear systems*, Proc. of AeroSense: The 11th Symp. A.D.S.S.C. (1997).

# Remerciements

La soutenance de mon travail de thèse au printemps, cinq mois avant la fin prévue de mon séjour au Laboratoire de l'Accélérateur Linéaire, ne doit pas être interprété comme volonté de départ anticipé. J'ai eu beaucoup de satisfaction à travailler dans cette unité de recherche du CNRS. Pour cela, je dois remercier deux Directeurs du Laboratoire de l'Accélérateur Linéaire, Bernard d'Almagne, qui m'a accueilli au LAL, et Guy Wormser, qui a accepté de participer à mon jury.

Un jury que je remercie de son intérêt pour mes recherches, avec une mention particulière pour ses membres séjournant loin de Paris.
Eric Aubourg, venu de Princeton et de recherches en cosmologie. Eric Gourgoulhon, intéressé aux progrès des détecteurs d'ondes gravitationnelles au fil de rendez-vous expérimentateurs-théoriciens organisés de temps à autre entre les groupes du LAL et de l'Observatoire de Paris. Erik Katsavounidis, membre de la collaboration LIGO au MIT et directement impliqué dans l'analyse, que j'ai eu l'occasion de rencontrer dans le groupe de travail LIGO-Virgo. Fulvio Ricci, de Rome, responsable de l'analyse pour la collaboration Virgo pendant ma thèse, qui a pu suivre mon cheminement étape par étape.

Toute ma gratitude à mon Directeur de Thèse, Patrice Hello, adepte invétéré du calembour, voire des calembredaines. Il est surtout enseignant et chercheur : son sens physique et ses qualités de pédagogue m'ont également beaucoup aidé.

Les autres membres du groupe d'analyse Virgo à Orsay, Fabien Cavalier, Marie Anne Bizouard et Nicolas Leroy, ainsi que Stéphane Kreckelbergh, jusqu'à la fin de sa thèse en octobre dernier, m'ont aussi apporté soutien et compétences. Merci à eux pour l'environnement de travail au quotidien, très détendu, les discussions et éclaircissements sur les nombreux aspects de Virgo et de la recherche publique, comme pour les à-côtés des déplacements professionnels, en Toscane, sur le site de Virgo, et ailleurs : passages obligés des visites touristiques, restaurants du pays et fins de soirées autour d'un verre.
Je suis reconnaissant à Michel Davier, responsable du groupe Virgo au LAL, qui m'a permis de participer à des conférences, Annecy, Val d'Aoste, Okinawa, avec le support du groupe puis de la collaboration.

Le support, ce sont aussi les fonctions non-scientifiques du laboratoire, indispensables à l'activité de recherche. Un grand merci à Sylvie Prant au Service du Personnel, au Service Informatique, en particulier Roland Boda et Françoise Macek, au service Missions, avec Annie Huguet et Anne-Marie Caudan, et à la bibliothécaire du laboratoire, Françoise Maréchal.

Dans le cadre du projet LIGO-Virgo, et de mon utilisation des données afférentes, je remercie Andrea Viceré, en charge de leur production. Ce projet fut l'opportunité de rencontrer des membres de la collaboration LIGO, en particulier Shourov Chatterji, dont le travail de thèse fut sur certains points parallèle au mien, et Steve Fairhurst.

Parmi les nombreuses personnes que j'ai rencontré dans la collaboration Virgo, je salue amicalement Gianluca Guidi, Leone Bosi, Maddalena Mantovani et Magali Loupias.

Si Virgo, la recherche, puis la rédaction, ont occupé la majeure partie de cette période de doctorat, j'ai heureusement pu maintenir des contacts et activités autres.

Toujours sur le campus d'Orsay, mes fonctions de moniteur m'ont amené à travailler avec

Delphine Monnier Ragaigne, Véronique Vèque et Anthony Busson. Je les remercie pour cet apprentissage de l'enseignement universitaire.

Comme amateur de théâtre, je remercie l'Aria, pour deux mois de pratique théâtrale en Corse, coupures estivales très appréciées dans le parcours et sources de rencontres très enrichissantes. Merci à mes amis, que j'ai pu voir, ou pas, selon les aléas de mes progrès et des rendez-vous avec Virgo. J'espère avoir entretenu, plutôt qu'éteint, leur curiosité pour l'astrophysique.

Pour terminer au plus personnel, ce travail n'aurait pu être mené sans le soutien de mes parents, René et Colette, sans faille tout au long de mes (longues) études. Salutations fraternelles à Patrick, Jean-Christophe, mes frères.

**Summary**

The gravitational wave interferometric-detector Virgo should soon reach its target sensitivity. The main astrophysical sources expected are the inspiral of compact binary systems and gravitational supernovae. Signal amplitudes are only slightly above the instrument sensitivity. Event rates are very low and waveforms are ill-known, notably for gravitational collapses. The objective of data analysis is therefore the detection of low amplitude signals in colored noise. This work proposes the use of time-frequency methods for the detection of short duration signals. Performances are estimated on simulated data and compared to other detection filters used in the community. Another difficulty for data analysis is the presence in the noise spectral density of narrow-band structures. These originate in the mechanical resonances of the mirrors and seismic isolation system of the instrument. Kalman filters are introduced to suppress these well-modelled noises in the data. The critical issue being the adequacy of the model, the problem of parameter estimation is tackled with the aim of a dynamical update. Finally these tools are applied to the available Virgo data. The main conclusion from this practical study is the identification of several instrumental noise sources, that will not disappear until the isolation of the instrument and its behaviour are improved.

**Keywords** :

Virgo
Interferometer
Gravitational Waves
Supernova
Instrumental noise
Kalman filter
Time-frequency decomposition
Signal analysis
Compact object
High energy astrophysical phenomena

**Résumé**

Le détecteur d'ondes gravitationnelles par interférométrie optique Virgo atteindra bientôt sa sensibilité nominale. Les sources astrophysiques attendues sont principalement les coalescences de systèmes binaires d'objets compacts et les supernovas gravitationnelles. Les amplitudes des signaux sont à la limite de la sensibilité de l'instrument, les taux d'événements observables sont faibles et les formes d'ondes mal connues, notamment pour les effondrements gravitationnels. L'analyse des données repose sur la recherche de signaux de faible amplitude dans du bruit coloré. Dans ce contexte, ce travail propose l'utilisation de décompositions temps-fréquence des séries temporelles pour la détection de signaux courts. Les performances de cette approche sont estimées en simulation et comparées à celles d'autres méthodes de détection disponibles dans la communauté. Une autre difficulté pour l'analyse est la présence de structures spectrales étroites dans la distribution d'énergie en fréquence des données. Elles proviennent de résonances mécaniques des miroirs et du système d'isolation sismique de l'instrument. L'utilisation de filtres de Kalman pour éliminer ces bruits bien modélisés avant l'analyse est présentée. Le problème essentiel de l'estimation des paramètres du modèle est traité, avec l'objectif d'une réestimation dynamique. Enfin ces outils sont appliqués aux données Virgo disponibles, avec comme résultat principal la mise en évidence de sources de bruits instrumentaux importantes, dont la suppression demandera une amélioration du fonctionnement et une meilleure isolation de l'environnement.

**Mots Clés** :

Virgo
Interféromètre
Ondes Gravitationnelles
Supernova
Bruit instrumental
Filtre de Kalman
Décomposition temps-fréquence
Analyse du signal
Objet compact
Phénomènes astrophysiques de haute énergie